MAREES TERRESTRES

BULLETIN D'INFORMATIONS

INTERNATIONAL CENTER FOR EARTH TIDES
CENTRE INTERNATIONAL DES MAREES TERRESTRES

Federation of Astronomical and Geophysical Data Analysis Services (FAGS)

International Association of Geodesy - International Gravity Field Service (IAG – IGFS)

Publié par l'Université de la Polynésie française

BIM n°145

ISSN n° 0542-6766

15 DECEMBRE 2009

Éditeur : Pr. Jean-Pierre BARRIOT
Observatoire Géodésique de Tahiti
Université de la Polynésie française
BP6570 – 98702 Faa'a
Tahiti-Polynésie française

BLANK PAGE

The precious help of Prof. Bernard Ducarme is gracefully acknowledged for his guidance and help in completing this issue of the BIM.

BLANK PAGE

BIM n°145

15 décembre 2009

New Challenges in Earth Dynamics (ETS2008) – continued

ANNOUNCEMENT

The International Center for Earth Tides (ICET) reminds you that its web site is now online at:

http://www.upf.pf/ICET/

This web site includes a link and instructions to access the new ICET online database, as well several tools for analyzing and processing tide signals.

BLANK PAGE

Tidal and Seiche signals on Baikal Lake level.

Timofeev V.Y., Granin N.G.*, Ardyukov D.G.,
Zhdanov A.A.*, Kucher K.M.* **B. Ducarme

Trofimuk Institute of Petroleum Geology and Geophysics SB RAS, Novosibirsk, Russia
**Limnological Institute SB RAS, Irkutsk, Russia*
***Royal Observatory of Belgium, Brussels, Belgium*

Abstract

Study of Baikal Lake level variation was developed by pressure sensor with digital system. Observation point is located at Listvyanka (source of Angara river, Baikal Lake). Seasonal water level variations reach 0.8÷1.1 m. Tidal amplitudes reach 7.9 mm (M2), 5.6 mm (S2), 4.6 mm (O1), 6.8 mm (K1) and 20.9 mm (Mf). We discuss tidal and seiche models for Baikal Lake. The diurnal and semi-diurnal tides can be explained by a tidal oscillation of the southern basin of Baikal Lake along a direction 70°N..First mode of seiche has a period of 4.6 hour with an amplitude of 60 mm. We tried to observe these effects with GPS observations too. Snow-ice shield covers Baikal Lake (Eastern Siberia) during January-May period. Ice shield displacements studies have been performed during three Baikal-winter expeditions (February-March, 2006, 2007, 2008) with geodimeter and GPS receivers. Motion and breaking process of ice field was observed along long cracks between snow-ice blocks. Sizes of these objects were from 1 km to 20 km accross Baikal Lake. Fracturation and displacement process is connected with winds, currents, air pressure, temperature, earthquakes, seasonal level variations and snow-ice conditions at Baikal Lake. After these events eigen-frequencies of snow-ice fields was registered with periods from 1 minute to 5 minutes and with amplitude up to 12 mm. Model of blocks with elastico - viscous connections is well correlated with observed data for eigen-frequencies following growing crack process and allows to determine the Young modulus of the ice.
Key words: Baikal Lake level, tide and seiche, pressure sensor, GPS receiver, geodimeter, ice field motion, eigen-frequency of blocks.

1. Introduction

Baikal Lake is situated in central Asia between 51° 29’ and 55° 46’ N (Figures 1, 2). Baikal Lake covers an area of 31500 km^2. It is 636 km long and its width varies between 25 km and 80 km. The fresh water volume accumulated is 23000 km^3 and the coast line is 2000 km [Baikal Atlas, 1993]. Baikal Lake consists of south basin with maximal depth 1423 m, middle basin with maximal depth 1637 m and north part with maximal depth 890 m. Winter period at Baikal region lasts more than 180 days. Annual average temperature is -0.7 °C in southern

part, -1.6 °C in central part and -3.3 °C for northern part. Snow covers Baikal region from October-November to April-May; thickness of snow reaches 1÷40 cm; maximal thickness can exceed 1 m in Mountain area at south-west and north-east of Baikal Lake. Ice covers Baikal Lake from December-January to May-June. Usual thickness for first decade of March is of 0.6÷1.0 m (Figure 1). Temperature and wind condition, circular currents in different Baikal basins and water level variation controls the typical configuration of ice cracks along coast line and accross Baikal Lake (Figure 1). Study of snow-ice plates velocity and brittle breaking on plate boundaries was the aim of two Baikal-winter expeditions [Dobretsov et al., 2007]. Another task was the study the tidal and seiche variations of Baikal Lake. We investigated tidal and seiche models for Baikal Lake.

2. Instruments and Method

Observation of water level was carried out at permanent station with pressure sensor, reaching a precision of 0.1 ÷ 2 mm level. Measurement of displacement of ice shield was developed by geodimeter and GPS technology. Two-frequency GPS receivers TRIMBLE-4700 and two-frequency geodimeter TOPAZ-SP2 were used for measurements [Goldin et al., 2005; Timofeev et al., 2006]. Geodimeter observation on 1 km base had precision level 1 ÷ 3 mm (usual reading 6 seconds) at summer condition. Experiment with geodimeter at -5°C ÷ -6°C (usual reading 12 ÷ 18 seconds) allowed to to reach a precision of 0.1 ÷ 0.5 mm (Talaya observatory, south-west of Baikal region, March-April 2005). Our GPS observation at Talaya observatory had been performed during 2000-2007 yy.. Using calculation by Gamit-GLOBK and GPSurvey programs for this point were received 1 ÷ 2 mm/y velocity to the East and seasonal variation of Talaya - Irkutsk line (76 km) with double amplitude 5 mm. During the Altai and Baikal campaigns we used hard benchmarks for our instrument. At Baikal Lake experiment equipment's tripods were frozen to snow-ice plate.

3. Ice plates relative motion

First winter expedition on Baikal Lake took place during the third decade of February 2006. Temperature condition from 22/02 to 26/02 were -12°C ÷ -20°C at day period and -20°C ÷ -26°C at night (minimum -26°C during 25 ÷ 26/02 night). Wind's conditions were changeable during the week. East-wind was blowing from 22 to 24/02 and S-E wind from 25 to 26/02 with a speed 1 ÷ 5 m/sec. Geodimeter polygon was located on different plates separated by big cracks (Figure 1, 2, 3). Distance to the lake coast was 3 km, and 6km to Listvyanka (the source of Angara river). During the campaign geodimeter measurements were performed at day time only. Changes along crack (base – reflector 1) from 314,513 m to 314,575 m were observed during 100 hours (22 ÷ 26/02). Cross line (base – reflector 2) changed up 120 mm during the same period. The trajectory of relative plate motion is presented at Figure 3. The duration of separate measurement was limited by temperature-wind condition and by the capacity of the battery (Figure 4). Only on

25/02/2006 three observation lines were monitored (Figure 3). The measured strain reached $2 \cdot 10^{-4}$ during the 8 hours observation period. Breaking ice process happened usually at night (10^{-3} strain level) and was accompanied by sound effect. The development of breaking process at day period is presented on Figure 4. This process had three stages. First stage - extension motion during two hours, second stage – shift plate motion along crack during three hours, third stage - breaking of ice with "natural frequency oscillations" and reverse motion. Oscillation on Natural frequencies after growing crack is presented on Figure 4. We had three periods of free oscillation – 0.8, 2 and 5 minutes. Viscosity of the ice was estimated by the delay curve: $10^{11} \div 10^{12}$ Pa·s.

1D model of three blocks with elastic - viscous connections [Figure 6, Medvedev, 2006; Nur, 1977] are close to observed data (Figure 5). Motion equations for three masses system with characteristic's equations are presented below:

$$\ddot{\xi} + 2b\dot{\xi}_1 + \omega_0^2(2 - \Delta k/k)\xi_1 - \omega_0^2\xi_2 = 0$$

$$\ddot{\xi}_2 + 2b\dot{\xi} + 2\xi_2 - \omega_0^2(\xi_1 + \xi_3) = 0$$

$$\ddot{\xi}_3 + 2b\dot{\xi}_3 + \omega_0^2(2 - \Delta k/k)\xi_3 - \omega_0^2\xi_2 = 0$$

$$\Delta k = k - k_1$$

$$\omega_0^2 = k/m$$

$$\lambda_{1,2} = -b \pm i\omega_0\sqrt{(2 - \frac{\Delta k}{2k}) - \sqrt{2 + (\frac{\Delta k}{2k})^2 - \frac{b^2}{\omega^2}}} = -b \pm i\omega_1,$$

$$\lambda_{3,4} = -b \pm i\omega_0\sqrt{(2 - \frac{\Delta k}{2k}) - \frac{b^2}{\omega^2}} = -b \pm i\omega_2,$$

$$\lambda_{5,6} = -b \pm i\omega_0\sqrt{(2 - \frac{\Delta k}{2k}) + \sqrt{2 + (\frac{\Delta k}{2k})^2 - \frac{b^2}{\omega^2}}} = -b \pm i\omega_3.$$

where ξ_i – shift of i-mass from equilibrium position; m – block mass; k and k1 - elastic parameters (block 1 – block 2; block2 – coast); b – viscosity parameter, delay coefficient; ω_o – natural frequency.

When we have simple conditions (k = k1 and b – small) and use frequencies from our experiment - ω_o = 0.1 rad/sec. We made elastic modulus determination and energy estimation for ice breaking process in the frame of model for blocks with elastico - viscous connections (Figure 6).

Elastic modulus for ice: we have ice plates with dimensions l · w · h and density ρ.

Let us express the force F required to shift the ice plate on the distance Δx:

$F_\sigma = S \cdot \sigma = h \cdot w \cdot E\,(\Delta x / l)$, with E – Young module, σ - stress.

On other side the same elastic force can be written as:

$F_e = k \cdot \Delta x$, with k rigidity of harmonic oscillator with pulsation $\omega_0^2 = k / m$ (Figure 6).

From balance of power: $F_\sigma = F_e$, or

$$h \cdot w \cdot E\,(\Delta x / l) = k \cdot \Delta x,$$

As $k = m \cdot \omega_0^2$, $m = \rho \cdot h \cdot w \cdot l$,
we have for Young modulus:

$$E = \rho \cdot l^2 \cdot \omega_0^2$$

With $\rho = 0.92 \cdot 10^3$ kg/m^3, $l = 10^4 \div 4 \cdot 10^4$ m, $\omega_0 = 0.1$ rad/sec
We get $E = 10^9 \div 1.4 \cdot 10^{10}$ Pa

Energy estimation for ice plate system was developed as follows:
Let us consider a rectangular ice block with dimensions l, w and h and density $\rho = 0.92 \cdot 10^3$ kg/m^3,
volume V=h.w.l, mass $m = \rho \cdot h \cdot r \cdot l$, velocity $V_0 \approx 1$ mm/s [Kingery, 1963; Kouraev et al., 2007; Pounder, 1965] The cinetic energy $W_0 = m \cdot V_0^2 / 2$.
For $l = 10^4$ m, $w = 10^4$ m, $h = 0.7$ m we get $W_0 = .310^5$ J. It is less than an earthquake of magnitude M=1
For $l = 4 \cdot 10^4$ m, $w = 4 \cdot 10^4$ m, $h = 0.7$ m we get $W_0 = 510^5$ J. It is close to an earthquake with M=1

4. Plate displacement relative to Baikal coast

During the 2007 winter expedition we continued motion investigation. Start of this expedition was shifted to first decade of March as temperature-ice condition was different. We had a strong winter in 2006 (very cold January-February period with -30°C during the day) with ice thickness 0.7 ÷ 0.9 m during the third decade of February. In 2007 January-February period was warm with -10°C during the day. Only at first decade of March ice thickness reached 0.4 ÷ 0.6 m but we had strong condition during this decade (day temperature -15°C ÷ -25°C and wind up to 15 ÷ 25 m/sec). Weather allowed only to use the GPS method (Figure 2). Calculation of 3D displacement relative IGS IRKT station (Irkutsk) is presented on Figure 7. This period differed from last year not only by weather condition but by earthquake activity too. Earthquake process in Baikal basin was absent during 2006-expedition, but two earthquakes happened during 2007-expedition (Figure 2 and Figure 7). Our polygon situated near N-S crack at 3 km from coast and 3 km from Listvyanka. During 4 ÷ 10 March there was active ice breaking process and a more strong one during 7 ÷ 8 March night. 3D snow-ice plate trajectory reflected Baikal earthquake process (4 ÷ 5 March) and 0.5 m trust from West at 7 ÷ 8 March. These two features were present on seismograms recorded at Talaya station (TLY). Ice breaking process is the cause of increased noise for seismology in Baikal area during January-May period (see section 3).

5. Tides and seiche at Baikal Lake

Processing of GPS data obtained during 2007 campaign allows us to separate the daily variation on vertical displacement of ice shield (Figure 8). The 2008 expedition (Figure 9) seeks after different goals. Tidal process, seiche and ice

blocks displacement were investigated. Water level variation observed by pressure sensor with digital system was studied too. Displacement of ice blocks presented at Figure 10. Tidal and seiche variations are shown on Figure 11 and 12. Famous results were obtained for Lakes Baikal and Tanganyika, which have been studied accurately, in order to reveal the existence of Earth tides. Record of the levels obtained at two points on Lake Baikal have been analyzed at different times by Sterneck, Grace, Ekimov and Krawetz, Parfianovitch and Aksentieva and have provided the following numerical values [Melchior, 1983, 1992]:

Petchanaia (52° 15' N 105° 43' E)		Sterneck	$\gamma = 0.52$	$\varphi = -3°$
	Wave M2	Grace	$\gamma = 0.54$	
		Aksentieva	$\gamma = 0.72$	$\varphi = +1°$
	Wave K1	Sterneck	$\gamma = 0.73$	$\varphi = +4°$
Tankoi	Wave M2	Aksentieva	$\gamma = 0.55$	$\varphi = +27°$

The amplitudes are of about 5-6 mm.

Analog of Baikal Lake is Lake Tanganyika (Albertville). The observations were made at Albertville, where the lake is about 75 km wide. The median position of Albertville is such that the level there is insensible to the uninodal longitudinal seiches whose period is about 4 h (length of Lake 638 km, mean depth 800 m), on the other hand the binodal longitudinal seiche (period 2 h) and the uninodal transverse seiche (period 40 min) should be observable. Taking into account the short period of the free oscillations, we can treat the problem of the luni-solar tides by the static theory. The M2 amplitude is about 1.5 mm. As the width of the lake is 72km the EW tidal oscillation is

Albertville	Wave M2	Melchior	$\gamma = 0.55$	$\varphi = 9°$

For Baikal region we have normal tidal gravimetric and clinometric factors [Ducarme et.al., 2008, 2004, 2006; Timofeev et al., 2006b, 2008; Dehant et al., 1999]. Applying HICUM analysis method [Van Ruymbeke et al., 2001] on water level data at station Listvyanka (Figure 13) we estimated the amplitude of the main tidal waves: from 7.8 ÷ 7.9 mm for M2 to 20.9 mm for Mf wave (Figure 14) and from 4.3 ÷ 4.6 mm for O1 to 6.38 ÷ 6.9 for K1 (Figure 15). For the diurnal and semi-diurnal tides the total amplitude reaches a few centimeters. It is certainly not the static equilibrium tide which reaches a few decimeters. We tried first to model the signal by ETERNA tidal analysis method [Wenzel, 1996]. In Table 1 the observations seem to fit quite well a tilt in EW direction. However the phase lag for M_2 and the other main waves is still large and the fit is better when we use the azimuth "70°N" (Table 2). We can thus model the tidal effect as a tilt of Lake Baikal surface in the azimuth 70°N: There is a straightforward relation between the vertical tidal displacement Δr and the tilt of the surface ε [Melchior, 1983,ch.8]

$$\Delta r=(L/2).\sin\varepsilon$$

$$\varepsilon(\text{rad})= 2\Delta r/L$$

where L is the width of the lake in the given azimuth. For the wave M2 we observe a vertical displacement of 7.964mm. The corresponding tilt of the vertical is

$$\varepsilon= A_{th} *\gamma_{th}$$

The astronomical amplitude A_{th} (9.544mas) for a rigid Earth is modulated by the elastic response of the Earth expressed through the amplitude factor $\gamma_{th} = 1 + k - h = 0.69125$. This theoretical value is confirmed by the results obtained at the Talaya observatory ($\gamma_{NS.}= 0.704$ and $\gamma_{EW} = 0.710$; Timofeev et al., 2008). We get thus ε(mas)=6.597 and ε(rad)= 31.98 nanorad. Inserting these values in the relation

$$L=2\Delta r/\varepsilon(rad)$$

We get L=498km. Similar computations provide L=412km for S2, L=420km for O1 and L=440km for K1.These values are compatible with the total length of the southern and central basins of the lake from Slyudyanka in SW to Ust Barguzin in NE. This line is more or less oriented in the correct azimuth (Figure 16). The tidal tilt is symmetric around the ridge separating the two basins, where the tidal amplitude vanishes. The Northern basin oriented more in the NS direction should be a priori decoupled. However The above equation is written under the assumption that the tidal amplitude is equal to zero in the middle of the lake, as in the example given above for Lake Tanganyka, which has a very simple shape and NS orientation. In the case of Lake Baikal the southern basin where the observations take place is separated from the central one by a ridge and both basins could oscillate independently, provided that tides vanishes at the limit of the two basins. Then L will be the length of the southern basin and the relation becomes

$$L=\Delta r/\varepsilon(rad)$$

providing values ranging from 206km to 249km in rough agreement with the size of the southern basin. Further studies are required to get firm conclusions.
The fortnightly Mf tide has an amplitude similar to the equilibrium tide and is certainly generated by a completely different mechanism.

When we cut off tidal effect from water level records the seiche variation is clearly seen (Figure 17). Seiche have periods: 4h 33 m, 2 h 33 m, 1 h 28m, 1h 06 m at Listvyanka point. Zero lines for seiches are situated at distance 280 km, 130 km, 360 km, 540 km respectively from southern point of Lake (Kyultyuk).

Theoretical seiche periods presented in relation

$T = 2l / (n\sqrt{gh})$,

where l – length of the lake, h – average depth of the lake, g = 9.8 m/c^2 and n – number of knots (modes). For first seiche with period 4.6 h we have the depth 630 m.

Seiche amplitude has seasonal variation (Figure 18). The origin of seiches is connected with earthquakes, air pressure variation and with tides. First seiche (4h 38.4 min) is extremely well recorded at Listvyanka point as well in water level, as in ice displacement.

6. Conclusions

Study of Baikal Lake level variation was performed using pressure sensor with digital recording located at Listvyanka (source of Angara river) and GPS observations on Baikal ice. Ice shield displacements had been performed during three Baikal-winter expeditions (February-March, 2006, 2007, 2008) with geodimeter and GPS receivers. Seasonal water level variation are observed at 0.8

m ÷1.1 m level. Tidal amplitude may reach 7.9 mm (M2 wave), 3.5 mm ÷ 6.7 mm (O1 and K1) and 20.9 mm (Mf) at Listvyanka. The diurnal and semi-diurnal tides can be explained by a tidal oscillation of the southern basin along a direction 70°N. First mode of seiche fluctuation has a period 4.6 hour with double amplitude 60 mm (February-March). Origin of seiche is connected with earthquakes, air pressure variation and tides. Motion and breaking process of ice shield system was studied along cracks between ice fields. Eigen-frequencies of ice blocks was registered with periods from 1 minute to 5 minutes and with double amplitude up to 12 mm. Model of blocks with elastico - viscous connections were close to observed data for eigen-frequencies after growing crack process. Young's modulus for the ice was determined from a one-dimension model as $E = 7 \cdot 10^9$ Pa. Viscosity of the ice was estimated from the delay curve to $10^{11} \div 10^{12}$ Pa·s.

References

Baikal Atlas (in Russian), 1993, RAS, Moscow, 160 p.

Dobretsov N., Psahie S., Ruzich V., 2007, Ice shield of Baikal Lake as a model for tectonic study. // Doklady Earth Sciences, vol.412, No.5, 1-5.

Dehant V, Defraigne P, Wahr J., 1999, Tides for a convective Earth. // J. Geoph. Res., 104, B1, 1035-1058.

B.Ducarme, V.Yu. Timofeev, M. Everaerts, P.Y.Gornov, V.A. Parovishnii, M. van Ruymbeke. 2008, A Trans-Siberian Tidal Gravity Profile (TSP) for the validation of the ocean tides loading corrections. // Journal of Geodynamics, 45, p.73-82.

Ducarme B., Venedikov A. P., Arnoso J., Vieira R., 2004, Determination of the long period tidal waves in the GGP superconducting gravity data. // J. of Geodynamics, 38, 307-324

Ducarme B., Vandercoilden L., Venedikov A.P., 2006, The analysis of LP waves and polar motion effects by ETERNA and VAV methods. // Bulletin Inf. Marées Terrestres, 141, 11201-11210.

Goldin S.V., Timofeev V.Y., Ardyukov D.G., 2005, Fields of the earth's surface displacement in the Chuya earthquake zone in Gornyi Altai. // Doklady Earth Sciences, vol.405A, No.9, 1408-1413.

Kingery W.D., 1963, Ice and Snow. Properties, Processes, and Applications, Cambridge, Massachusetts, 380 p.

Kouraev A.V., Semovski S.V., Shimaraev M.N., Mognard N.M., Legresy B., Remy F., 2007, The ice regime of Lake Baikal from historical and satellite data: Relationship to air temperature, dynamical, and other factors. // Limnol.Oceanogr., 52(3), 1268-1286.

Medvedev N.I., 2006, Mechanical-mathematics models by geodesy data: non-proliferation oscillation in earth crust. Candidate Thesis (in Russian). Yuzno-Sakhalink. 2006, 150.

Melchior P., 1983, The tides of the planet Earth, 2nd ed. Pergamon Press, Oxford, 641 pp.

Melchior P., 1992, Tidal interactions in the Earth Moon system. // Chronique U.G.G.I., N210, Mars/Avril, MHN, Luxembourg, 1992. p.76-114.

Nur A., 1977, Nonuniform Friction as a Physical Basis for Earthquake Mechanics: a Review // Proc. of Conference 2 Experimental Studies of Rock Friction Prediction. – California: Menlo Park, 241-254.

Pounder E.R., 1965, The Physics of Ice. Pergamon Press, Oxford-London-Edinburgh-New York-Paris-Frankfurt, 350 p..

Timofeev V.Yu., Ardyukov D.G., Calais E., Duchkov A.D., Zapreeva E.A., Kazantsev, Roosbeek F., Bruyninx C., 2006, Displacement fields and models of current motion in Gorny Altai. // Russian Geology and Geophysics, Vol. 47, No. 8, 923-937.

Timofeev V.Y., van Ruymbeke M., Woppelmann G., Everaerts M., Zapreeva E.A., Gornov P.Y., Ducarme B., 2006b, Tidal gravity observations in Eastern Siberia and along the Atlantic coast of France. Proc. 15th Int. Symp. On Earth Tides. // Journal of Geodynamics, 41, 30-38.

Timofeev V. Y., Ardyukov D. G., Gribanova E. I., van Ruymbeke M., Ducarme B., 2009, Tidal and long-period variations observed with tiltmeters, extensometers and well-sensor (Baikal rift, Talaya station). Bull. Inf. Marées Terrestres, 135.

Van Ruymbeke, Fr. Beauducel and A. Somerhausen, 2001, The Environmental Data Acquisition System (EDAS) developed at the Royal Observatory of Belgium. // Journal of the Geodetic Society of Japan, Vol. 47 (1).

Wenzel H.G., 1996, The nanogal software: earth tide data processing package ETERNA 3.30. // Bull. Inf. Maréees Terrestres, 124, 9425-9439.

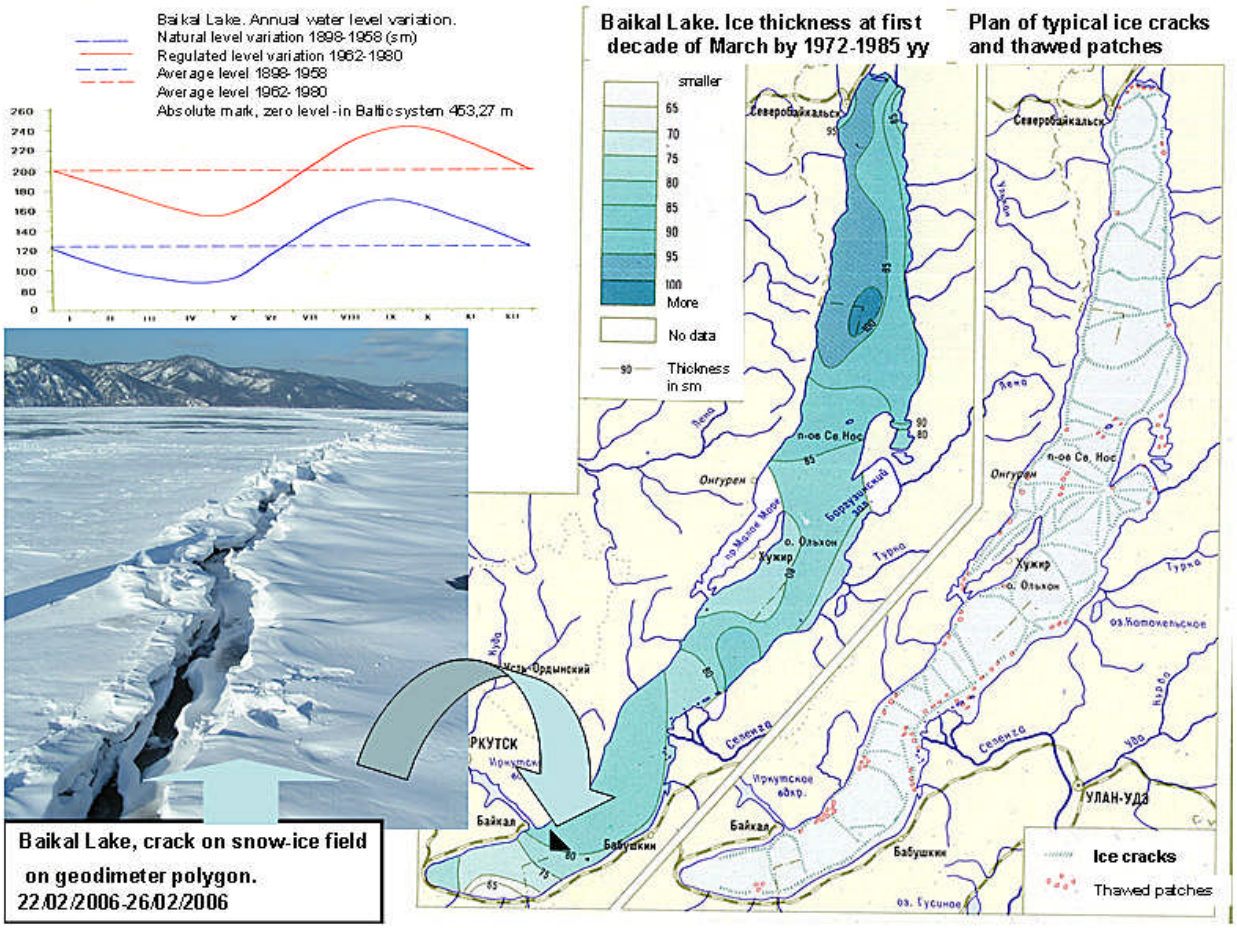

Fig. 1. Left slide – Baikal Lake, annual water level variation, before and after construction of Irkutsk power station;

– ice crack.

Right slide – Location of geodimeter polygon on snow-ice field;

– Map of ice thickness at first decade of March by 1972-1985 data;

– Sketch of typical ice cracks and thawed patches [Baikal Atlas, 1993].

Geodimeter polygon

GPS polygon and Tidal observation point (Listvianka Port)

Polygon of GPS observation on Baikal Lake (04/03/2007 – 09/03/2007), points of GPS station (circle – Irkutsk, Talaya), regional earthquakes on Baikal Lake (star, 20-15-21.4, 04/03/2007, 55.69 °N, 110.15° E, M = 4.1; 16-48-54.9, 5/03/2007, 54.97 °N, 109.34 ° E, M = 4.0).

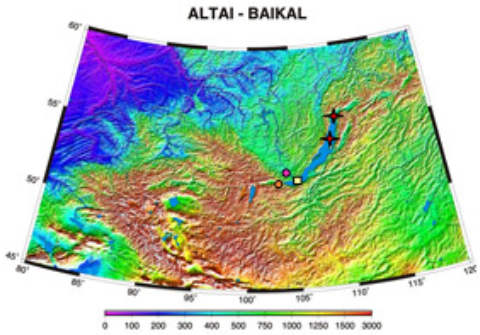

2007. Polygon of GPS observation on Baikal Lake, 25 m – distance from antenna to N-S ice crack.

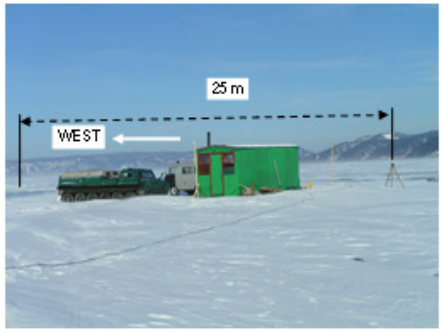

Figure 2. 2006-2008 expeditions on Baikal Lake.

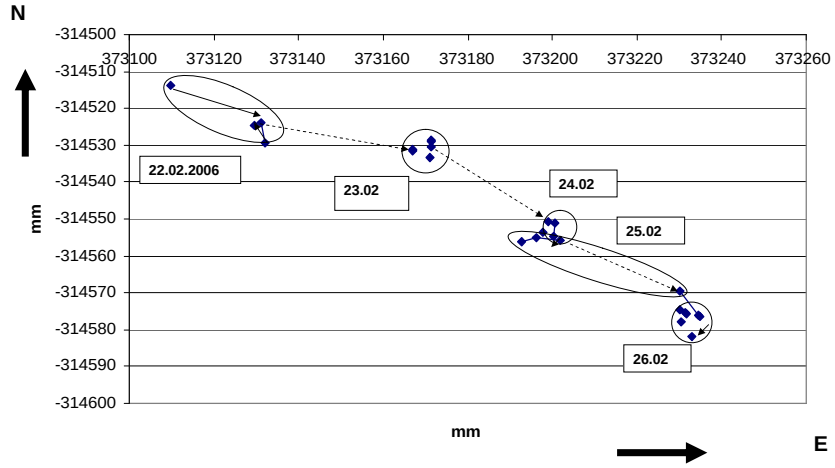

a)

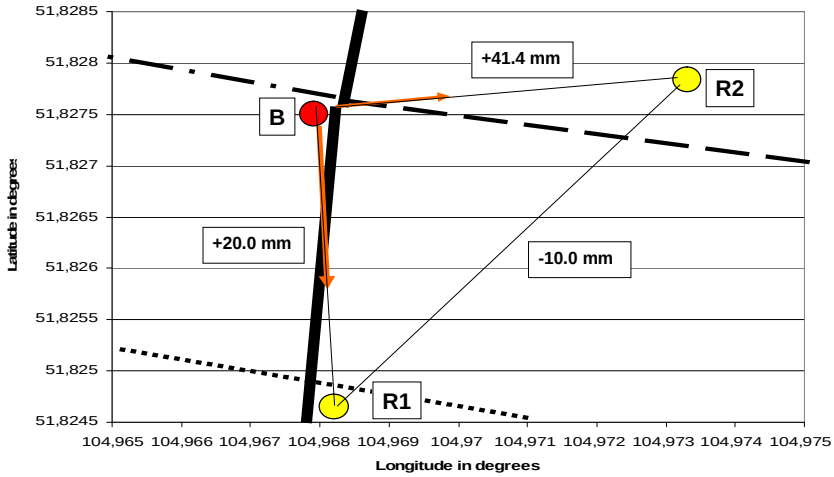

b)

Figure 3. a) Horizontal vector diagram by geodimeter data **from 22.02.2006 to 26.02.2006**
b) Geodimeter polygon (B-R1 = 314 m, B-R2 = 373 m, R1-R2 = 499 m), B – base, R1 and R2 – reflectors, solid line – main crack with shift-extension motion, interrupted line – trust zones. Change of lines from 10h to 18h **25/02/2006.** Values and orientation of main strain axes: compression $-0.2 \cdot 10^{-4}$, 38.1°N; extension $+1.9 \cdot 10^{-4}$.

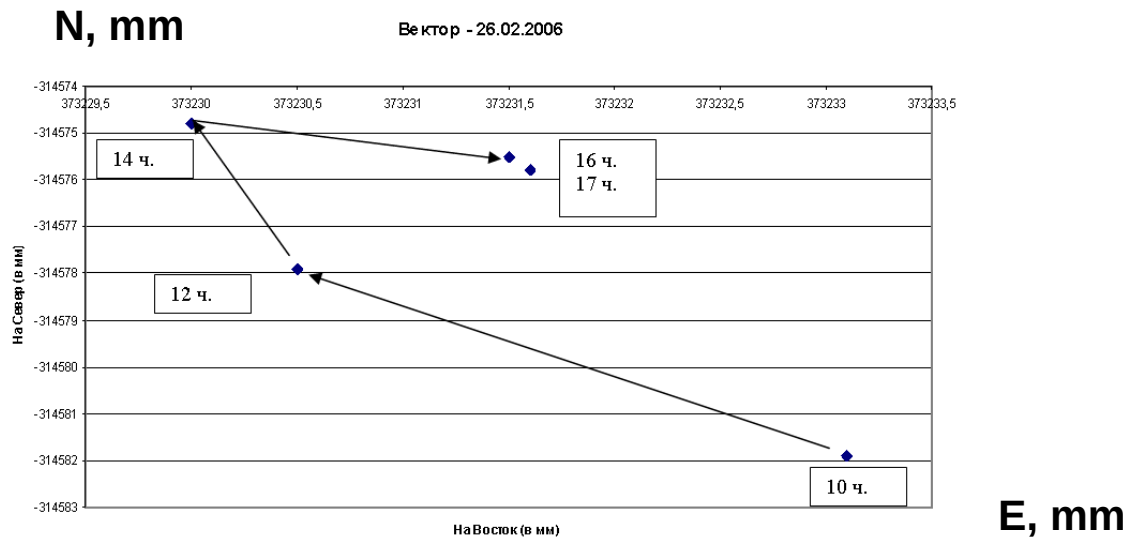

a)

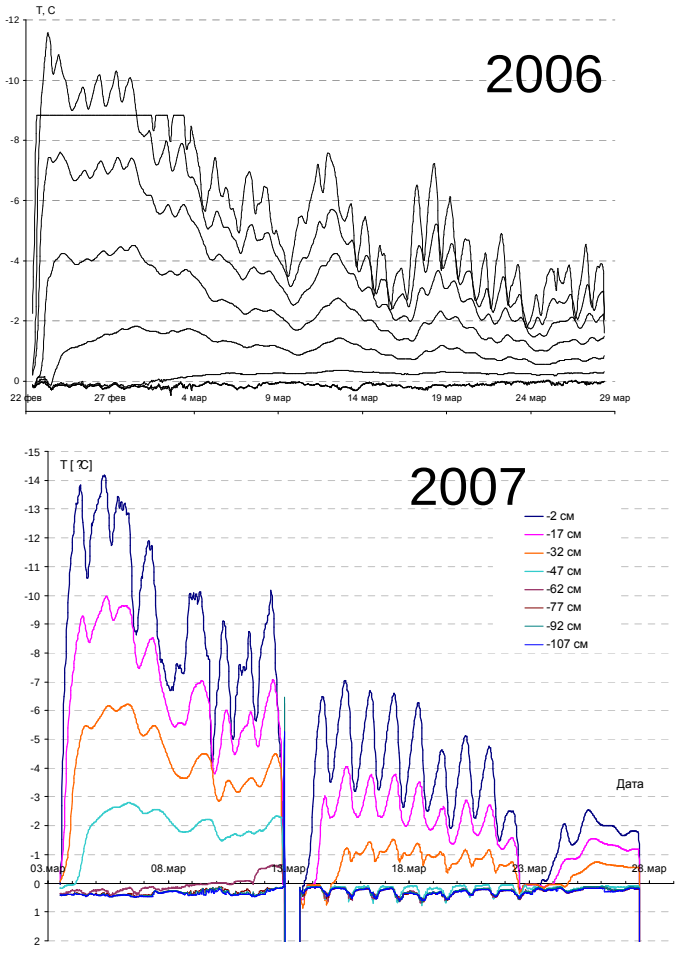

b)

Figure 4. a) Daily displacement of ice fields by geodimeter measurement from 10 h (L.T.) to 17 h 26.02.2006. 14 h – sound of breaking ice. Temperature: -26 degrees at night, -11 degrees (day), East wind, at evening – SW wind.

b) Daily temperature variation at different ice depths.

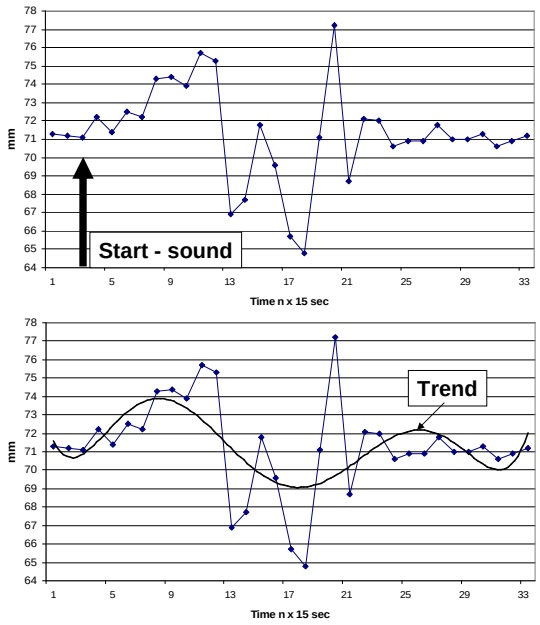

a)

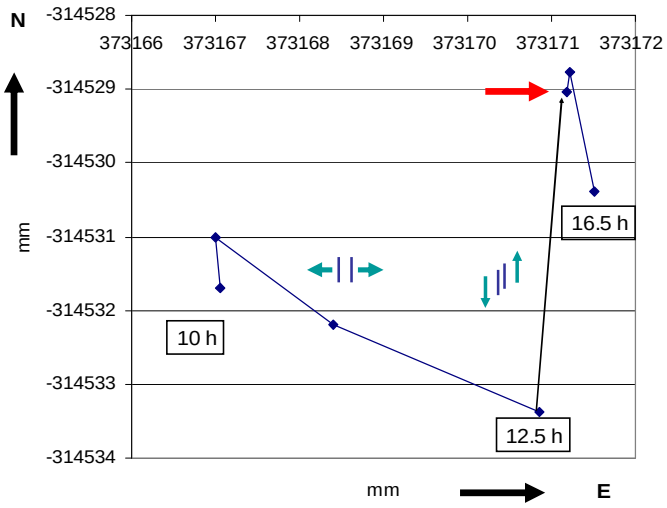

b)

Figure 5. a) Natural source of free oscillation and trend with delay. Line EAST [L(t) – 373100] mm, from 15h 17m to 15h 26m 23/02/2006. Double amplitude up to 12 mm.

b) Ice blocks relative motion. Horizontal displacement by geodimeter data from 10 h to 16.5 h (L.T.) **23/02/2006.** Arrow – moment of ice braking (sound). Night temperature -24 °C, day temperature -16 °C, wind – West.

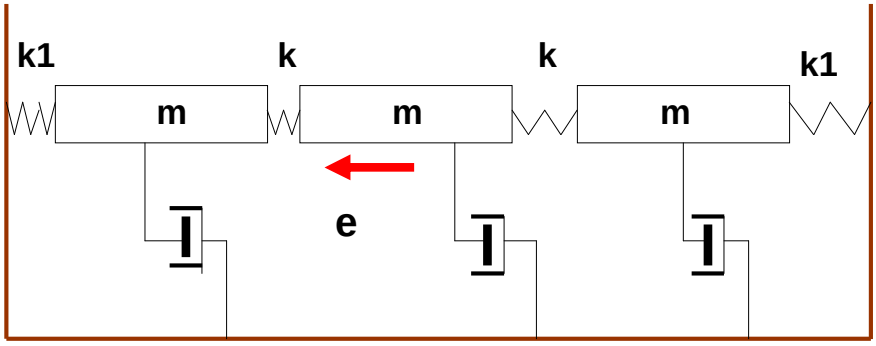

Figure 6. Model for blocks with elastico - viscous connections.

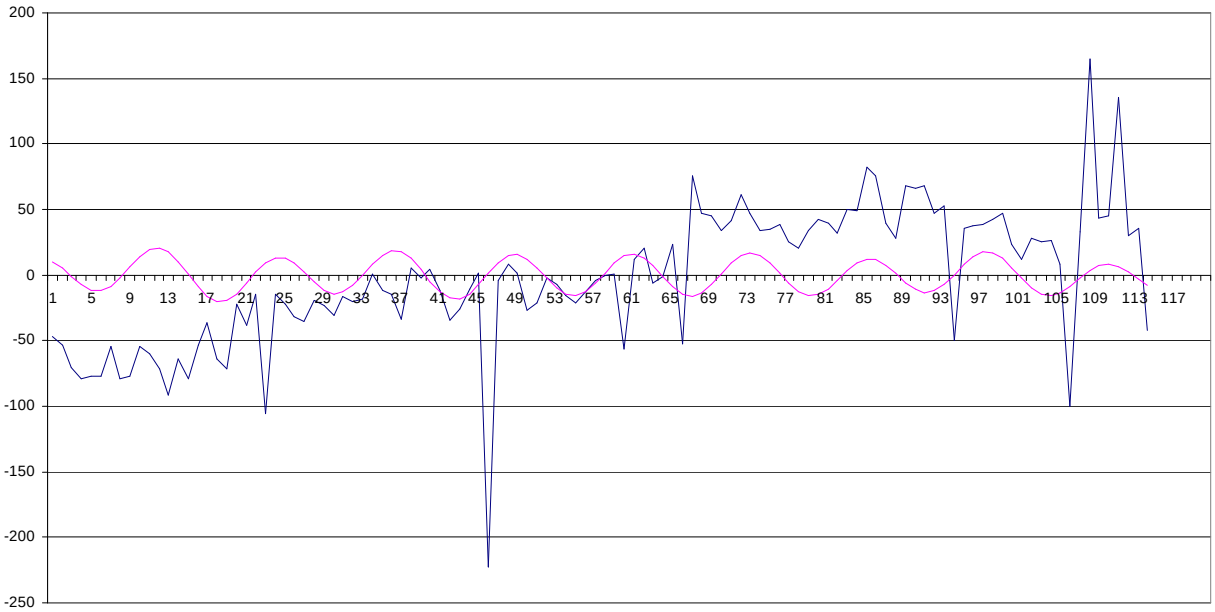

Figure 8. Vertical displacement by GPS 05.03.-08.03.2007

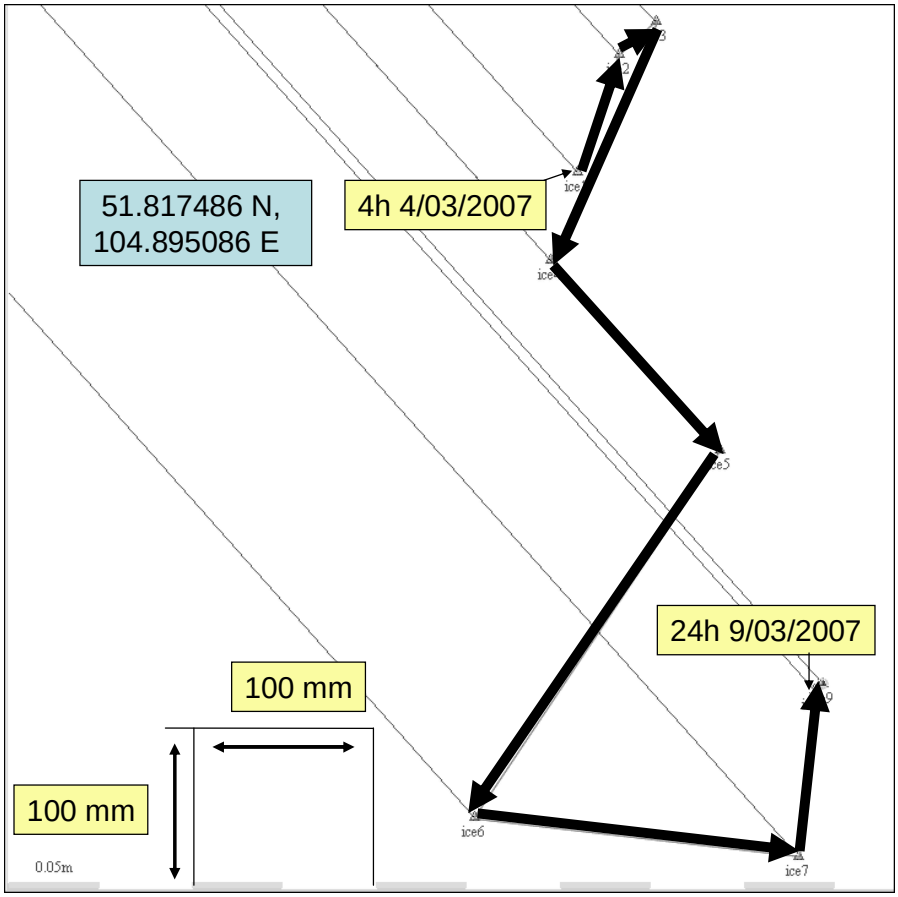

a)

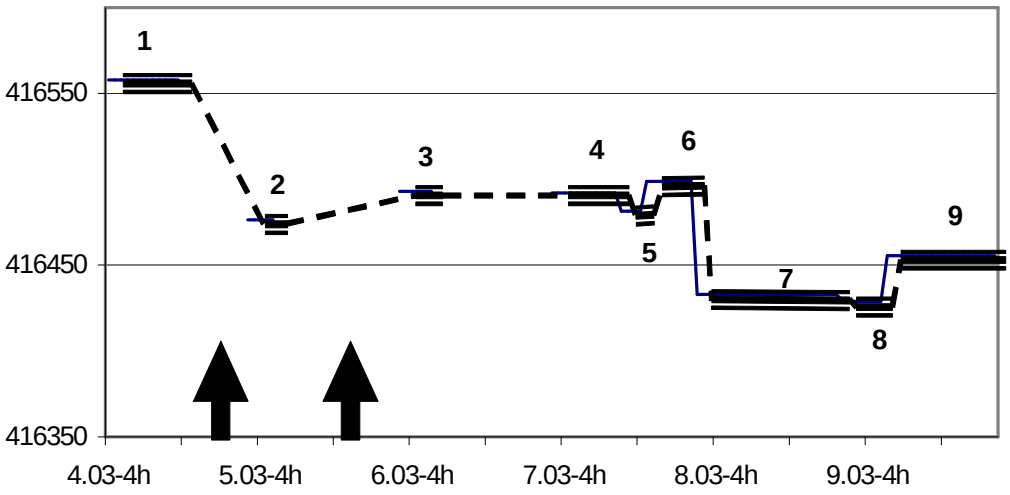

b)

Figure 7. Result of GPS observation - horizontal (a) and vertical (b, mm) displacements of ice plate from 04h 04/03/2007 to 24h 09/03/2007 (U.T., L.T. +8h). Calculation relative IRKT (Irkutsk) GPS station. Arrows – moments of regional earthquakes on Baikal Lake (20-15-21.4, 4.03.2007, 55.69 °N, 110.15° E, M = 4.1; 16-48-54.9, 5.03.2007, 54.97 °N, 109.34° E, M = 4.0). Moment “6-7” (night 7/03-8/03/2007) - brittle-breaking of ice – thrust motion from west (0.5 m thrust on ice plate). Subsidence 0.05 m was recorded at 25 m distance from crack line.

2008 ice expedition.

Positions of GPS point. BAZA and BALOK permanent station,

ICE1 and ICE2 net point (day period), blue lines – ice cracks and hummock border.

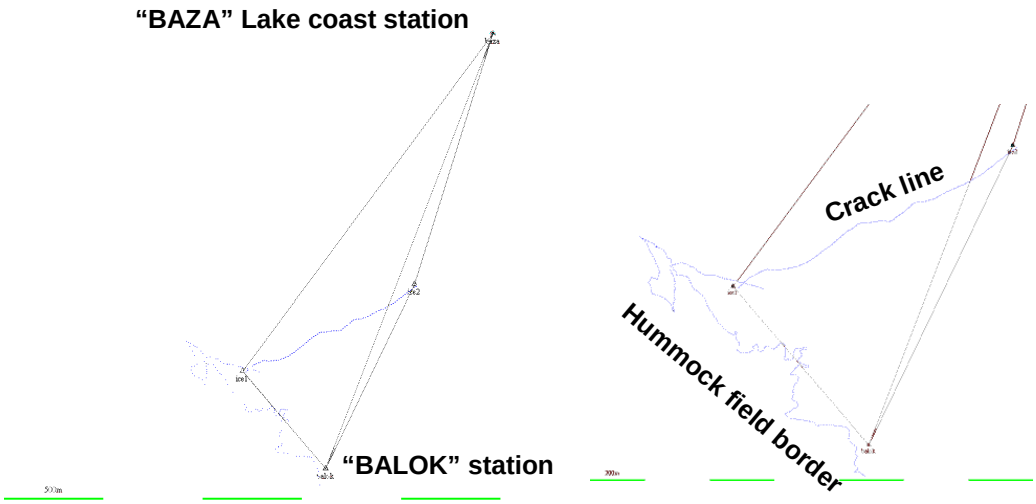

Figure 9. Positions of GPS points during. 2008 ice expedition.

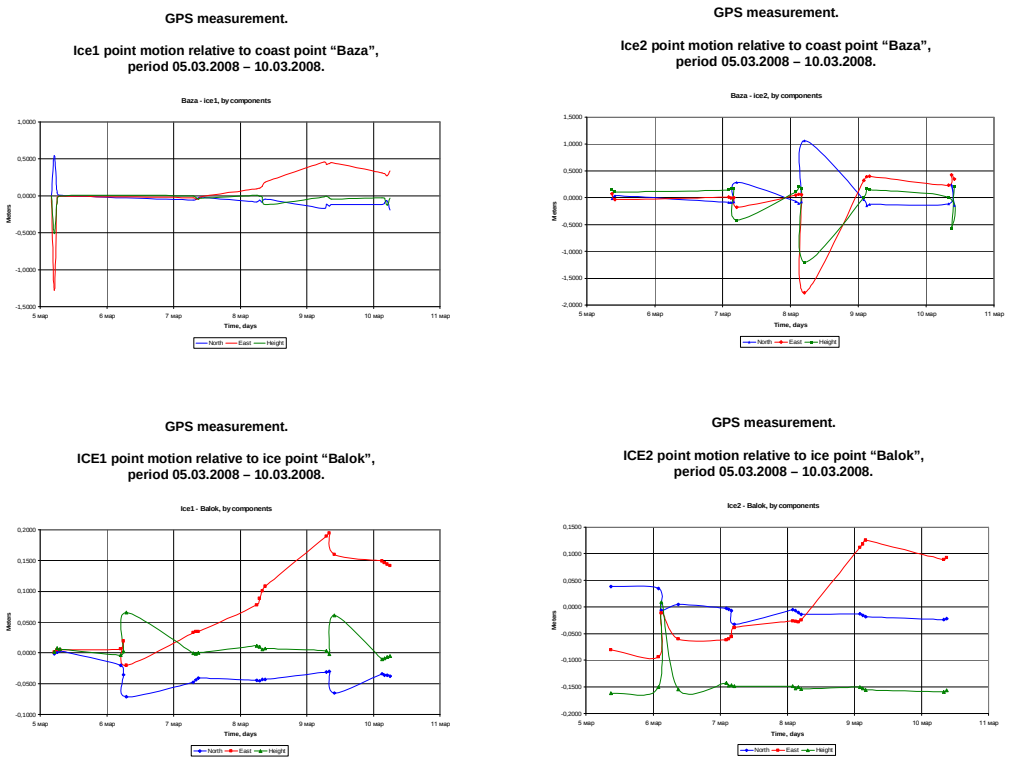

Figure 10. GPS measurement. 2008.

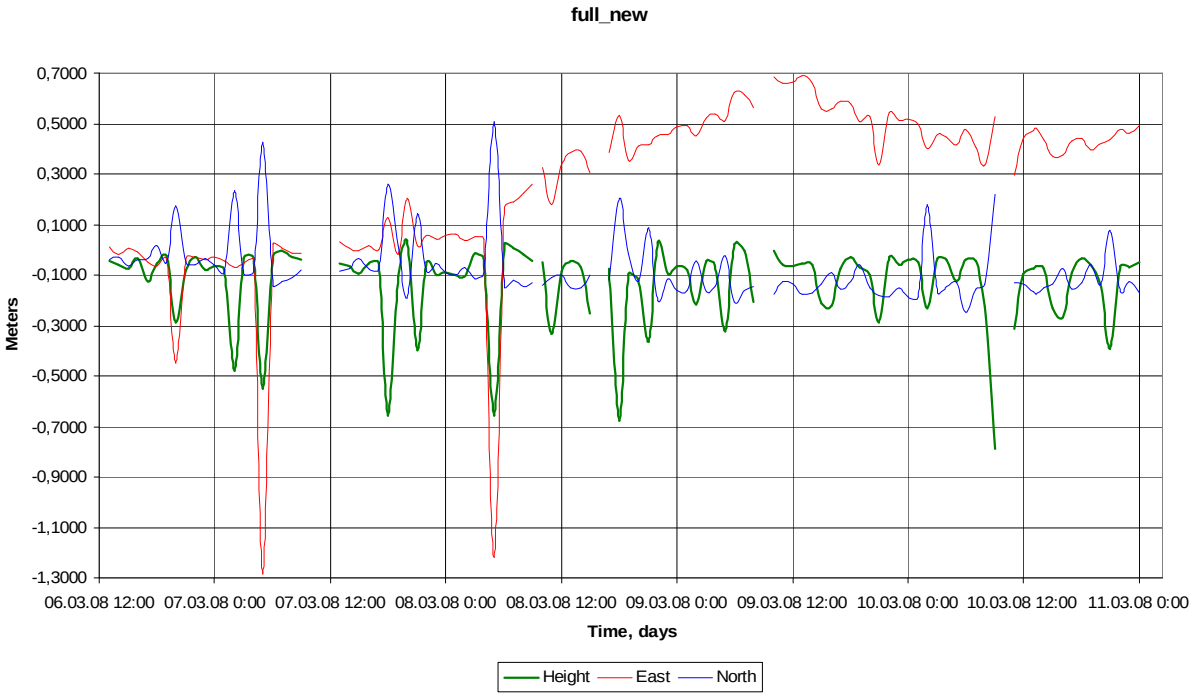

Figure 11. GPS measurement. Ice point “Balok” motion relative to coast point “Baza”, 12 h 06.03.2008 – 00h 08.03.2008. Seiche have 4÷5 h period.

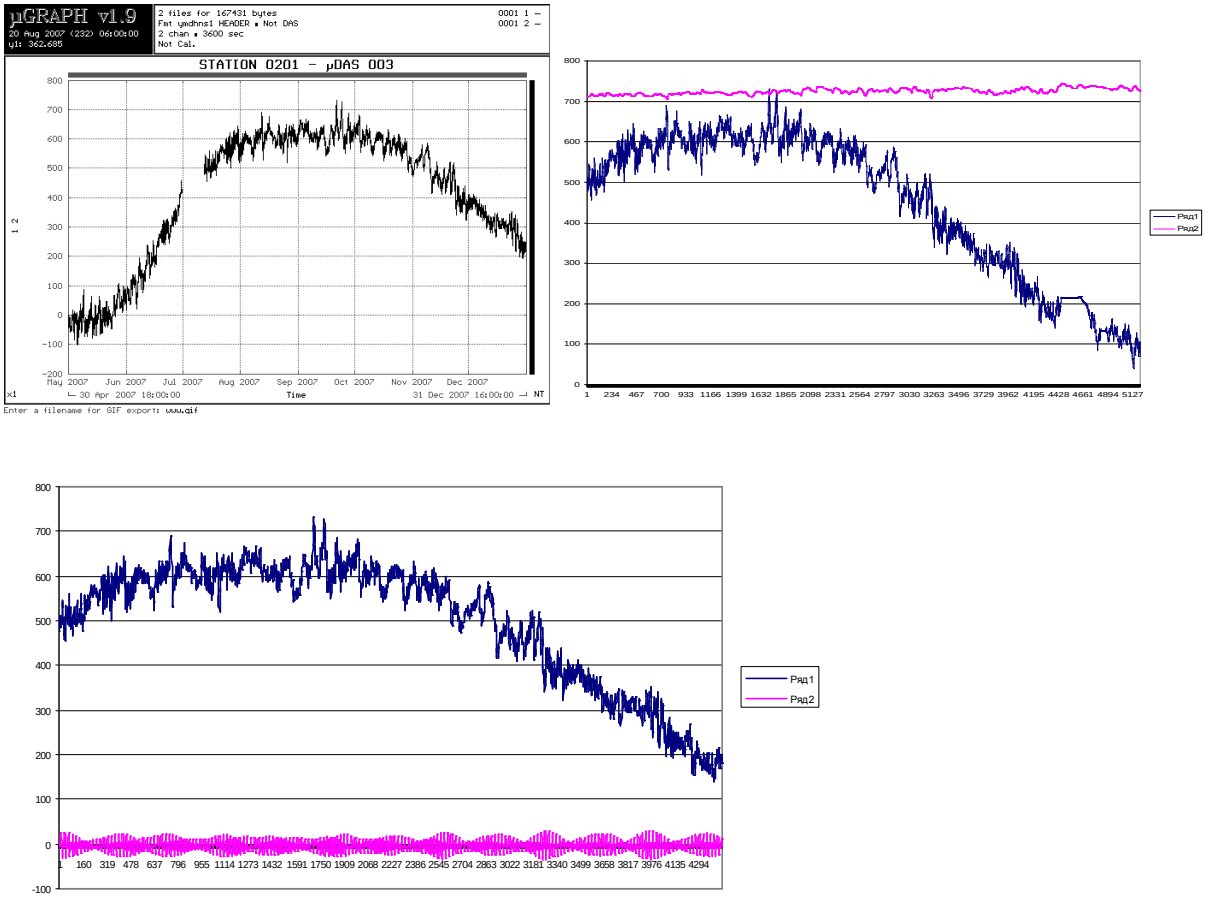

Figure 13.left: Baikal water level (mm) period from 19h 30.04.2007 to 16h 31.12.2007 (Annual variation 0.8 m)
Right:Baikal water level (1) and air pressure variation (2), period from 10h 12.07.2007 to 18h 12.02.2008.
Bottom:Baikal water level (1, mm) and theoretical tidal curve (2), period from 10h 12.07.2007 to 23h 12.01.2008

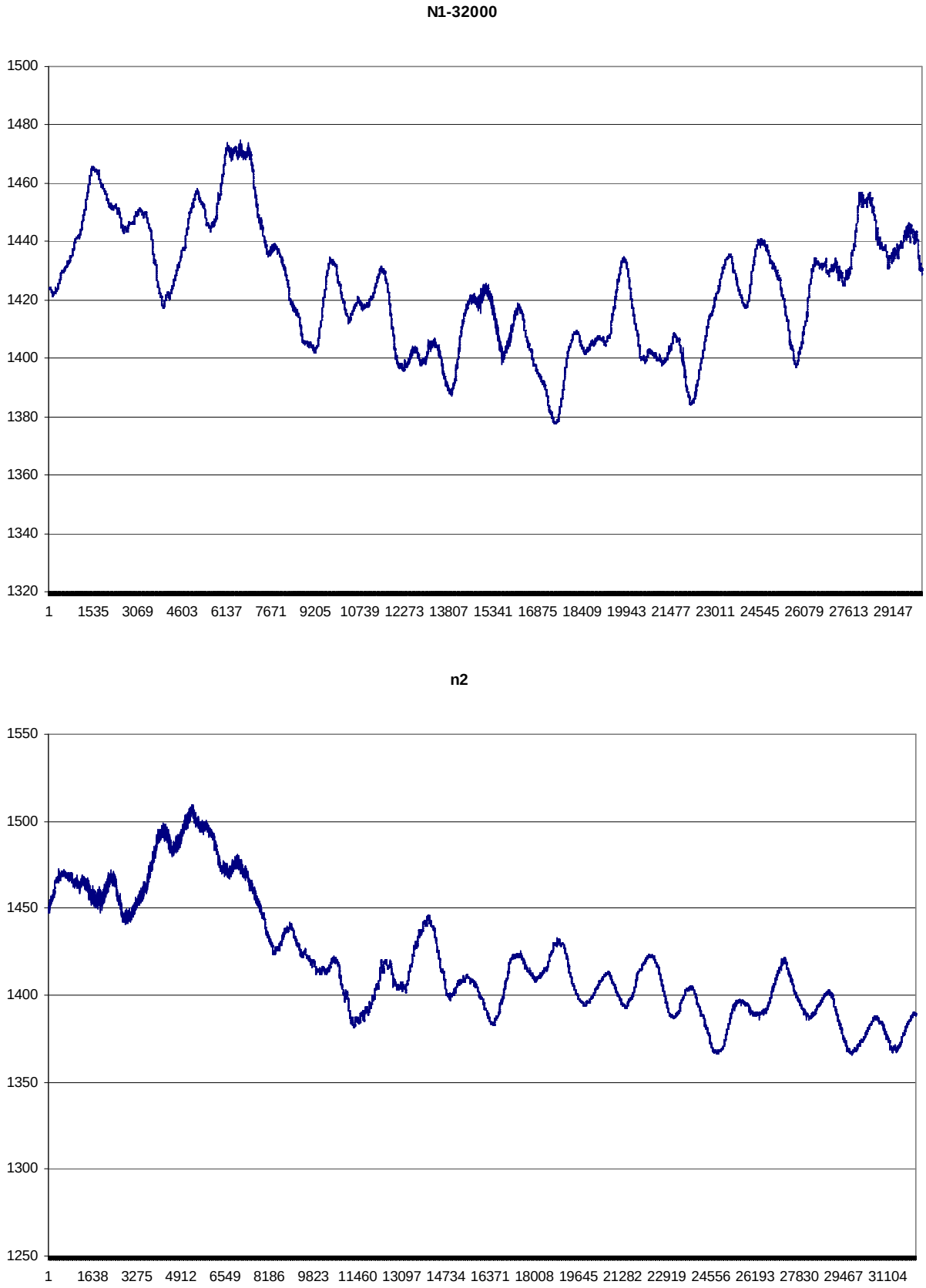

Figure 12. Baikal water level in mm. Point Listvyanka (10 sec. data). Tidal and seiche signals.

Top – from 21h 54m 44s 18.02.2008 to 09h 14m 34 s 22.02.2008.

Bottom – from 14h 47m 54s 22.02.2008 to 07h 41m 54 s 26.02.2008.

Tidal analysis by HICUM, water level in mm, different periods, amplitude for M2: 7.849; 7.793; 7.968 (by ETERNA: 7.964 mm), amplitude for Mf: 20.92 mm.

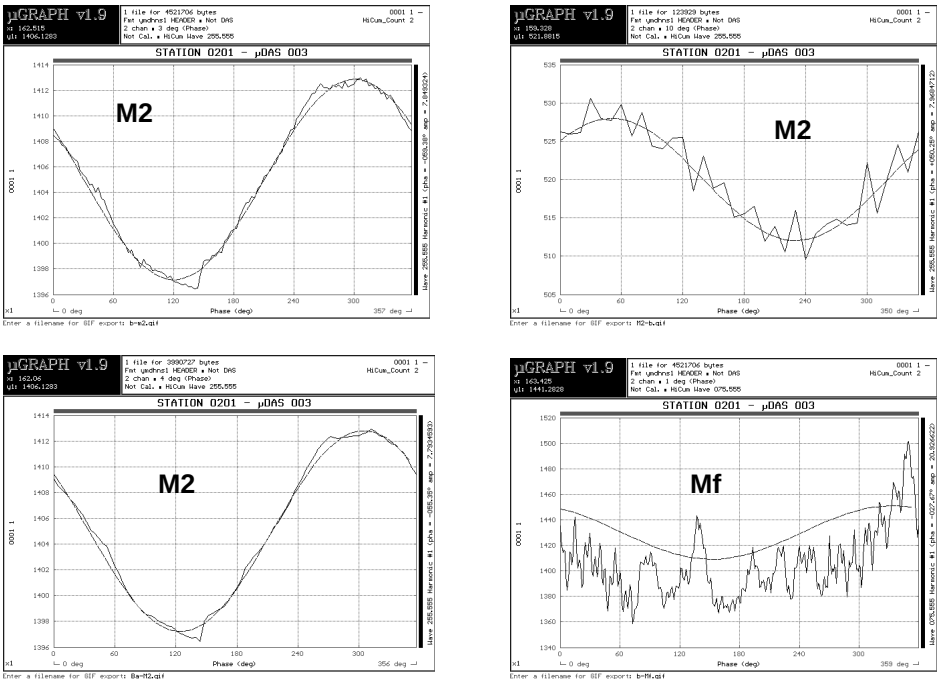

Figure 14. Tidal analysis by HICUM, water level in mm, different periods, amplitude for M2: 7.849; 7.793; 7.968 (by ETERNA: 7.964 mm), amplitude for Mf: 20.92 mm.

Tidal analysis by HICUM, water level in mm, different periods, amplitude for O1: 4.312; 4.639 (by ETERNA: 3.441 mm), amplitude for K1: 6.326; 6.877 mm.

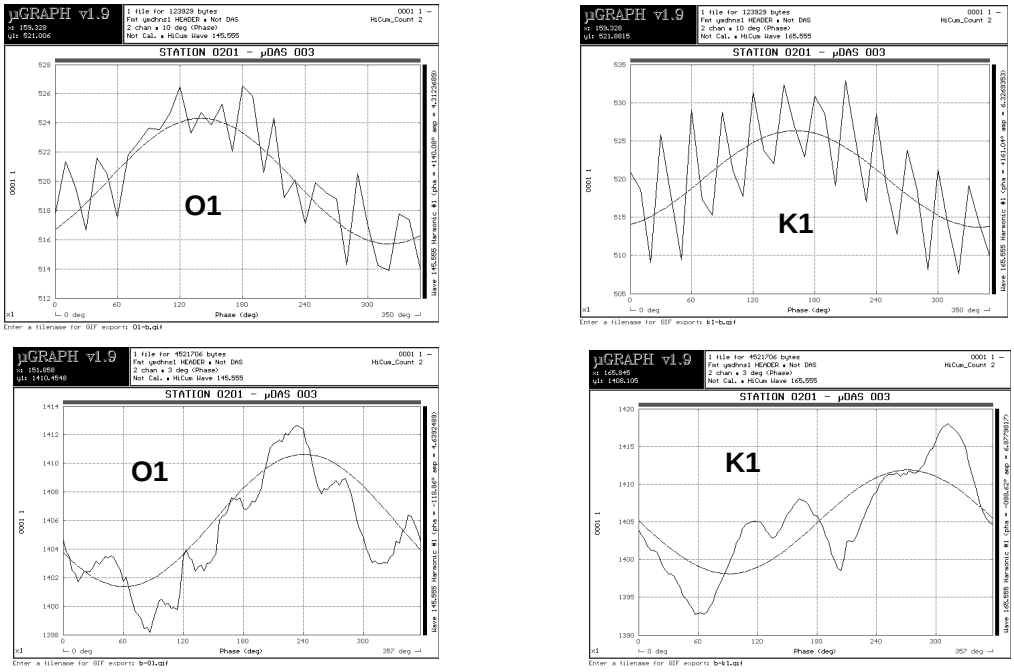

Figure 15. Tidal analysis by HICUM, water level in mm, different periods, amplitude for O1: 4.312; 4.639 (by ETERNA: 3.441 mm), amplitude for K1: 6.326; 6.877 mm.

Table 1. Baikal Lake water level tidal analysis by ETERNA (282 d.).

- Summary of observation data :
- 20070428100000...20070430160000 20070430180000...20070630160000
- 20070712100000...20080212180000 20080302 70000...20080305150000
- Initial epoch for tidal force : 2007. 4. 1. 0
- Number of recorded days in total : **282.00**
- CTED 1973 tidal potential used.
- UNITY window used for least squares adjustment.
- Numerical filter is PERTZEV 1959 with 51 coefficients.
- Estimation of noise by least squares method.
- Influence of autocorrelation not considered.
- Adjusted tidal parameters :

from	to	wave	ampl. [mm]	signal / noise	ampl.fac.	stdv.	phase lead [deg]	stdv. [deg]
286	428	Q1	0.652	5.2	0.66478	0.12691	-21.9829	7.2613
429	488	O1	3.442	26.6	0.67226	0.02528	13.0524	1.4485
489	537	M1	0.580	4.7	1.44160	0.30901	152.4077	17.7093
538	592	P1S1K1	4.532	35.9	0.62931	0.01755	19.3486	0.9961
593	634	J1	0.059	0.5	0.14763	0.29846	-57.6169	17.1020
635	736	OO1	0.290	3.2	1.31331	0.40871	18.6890	23.4445
737	839	2N2	0.270	2.4	0.90539	0.37681	39.5130	21.5894
840	890	N2	1.238	8.6	0.66200	0.07715	9.4261	4.4206
891	947	**M2**	**7.962**	51.7	**0.81537**	0.01578	**13.7928**	0.9042
948	987	L2	0.362	1.6	1.31082	0.83903	-23.6227	48.0790
988	1121	S2K2	3.562	24.0	0.78405	0.03268	26.0271	1.8774
1122	1214	M3	0.203	1.4	1.71064	1.23609	13.8662	70.8114

- Standard deviation of weight unit: 8.563
- degree of freedom: 6543
- Adjusted meteorological or hydrological parameters:
- no. regr.coeff. stdv. parameter unit
- 1 6.91506 0.14803 mas /

- Version ETERNA (1) ”tilt” in **90** degrees direction

Table 2. Tidal analysis by ETERNA used tilt version in 70° direction, water level in mm, air pressure – mm. p. p.. Period 28.04.2007 – 05.03.2008.

- Summary of observation data :
- 20070428100000...20070430160000
- 20070430180000...20070630160000
- 20070712100000...20080212180000 20080302
- 70000...20080305150000
- Initial epoch for tidal force : 2007. 4. 1. 0
- Number of recorded days in total : 282.00
- CTED 1973 tidal potential used.
- UNITY window used for least squares adjustment.
- Numerical filter is PERTZEV 1959 with 51 coefficients.
- Estimation of noise by least squares method.
- Influence of autocorrelation not considered.
- Adjusted tidal parameters :

from	to	wave	ampl. [mm]	signal / noise	ampl.fac.	stdv.	phase lead [deg]	stdv. [deg]
286	428	Q1	0.648	5.3	0.69969	0.13317	-27.8557	7.6228
429	488	O1	3.441	26.6	0.71091	0.02673	6.8399	1.5308
489	537	M1	0.616	4.7	1.61880	0.34300	144.8911	19.6561
538	592	P1S1K1	4.533	35.9	0.66591	0.01857	13.1618	1.0538
593	634	J1	0.063	0.5	0.16602	0.32352	-64.3833	18.5353
635	736	OO1	0.292	3.2	1.39926	0.43485	12.2403	24.9483
737	839	2N2	0.271	2.4	0.92786	0.38454	23.6946	22.0321
840	890	N2	1.235	8.6	0.67563	0.07869	-6.2061	4.5089
891	947	**M2**	**7.964**	51.7	**0.83440**	0.01614	**-2.1748**	0.9253
948	987	L2	0.331	1.5	1.22570	0.81193	-42.1139	46.5190
988	1121	S2K2	3.562	24.0	0.80225	0.03344	10.0549	1.9517
1122	1214	M3	0.203	1.4	1.75008	1.26458	-2.1077	72.4234

- Standard deviation of weight unit: 8.563
- degree of freedom: 6543
- Adjusted meteorological or hydrological parameters:
- no. regr.coeff. stdv. parameter unit
- 1 6.91587 0.14803 mas /

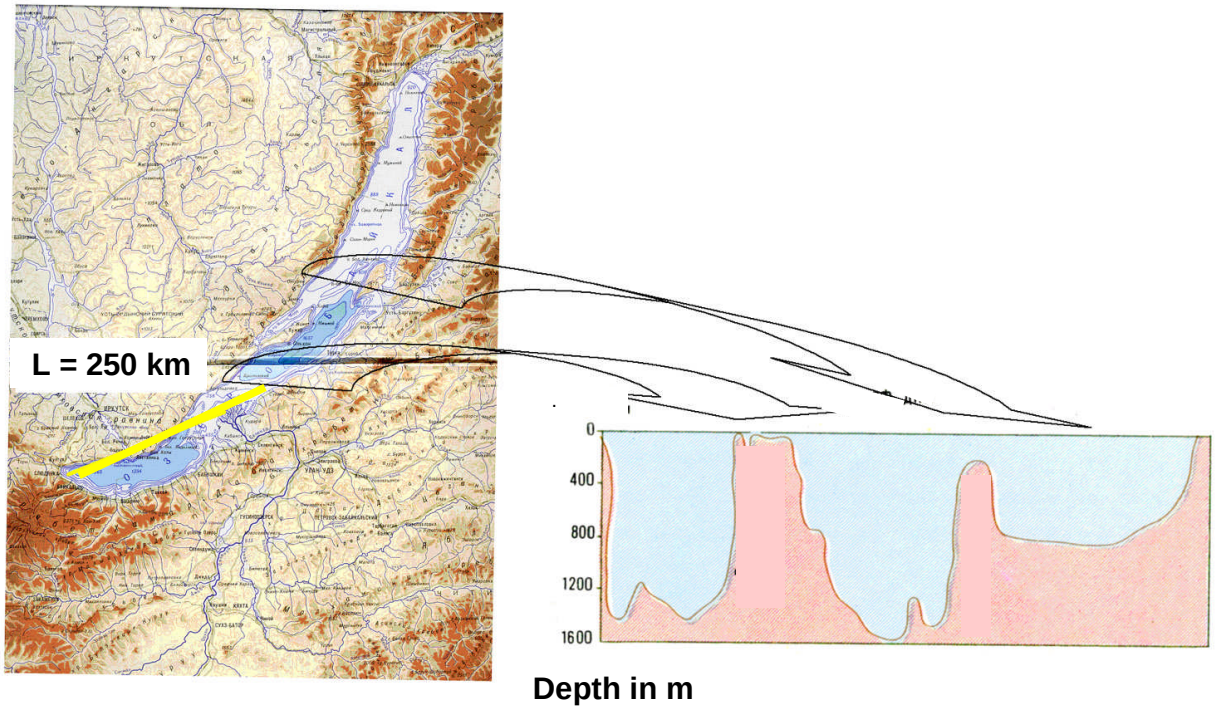

Figure 16. Baikal Lake: three hollows. Relief of Lake bottom from southern point to northern point [Baikal Atlas, 1993].

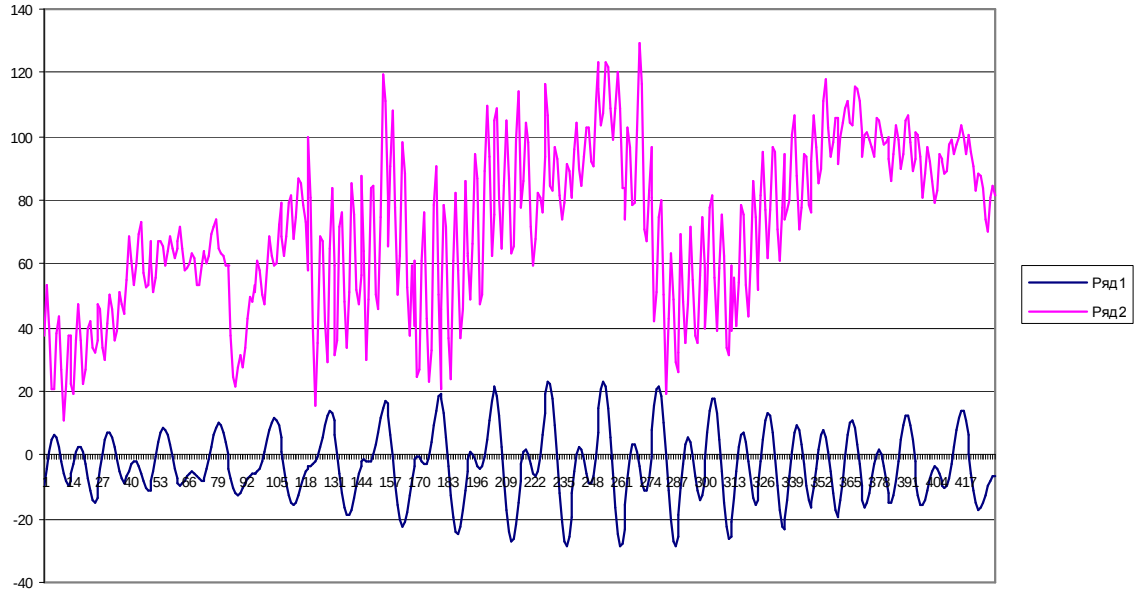

Figure 17. Baikal water level without tidal variation
– theoretical tidal curve (1, blue)
– seiche effect (2, red).
Seiches are generated at maximal tide. Double seiches amplitude reach 60 mm at Listvyanka point.

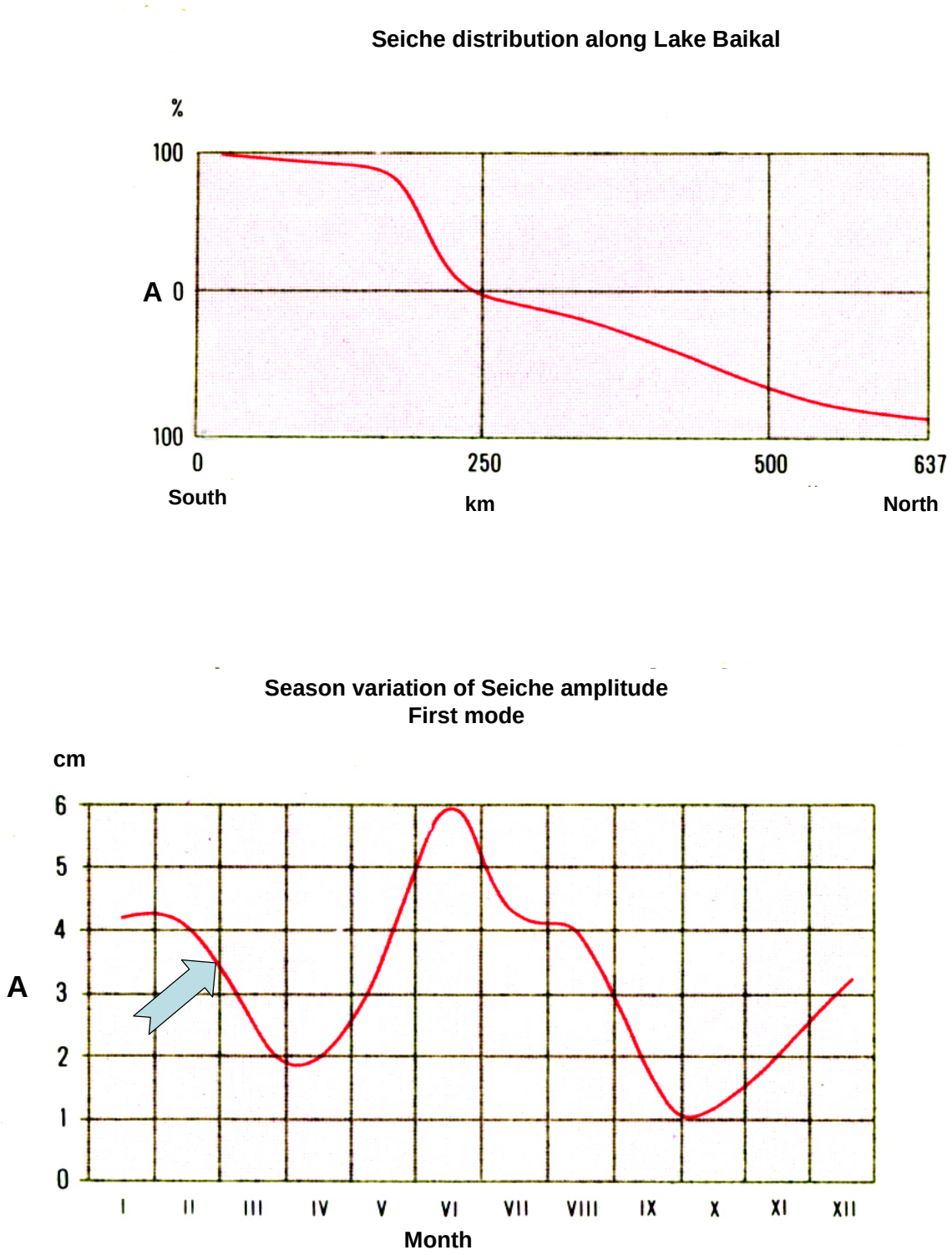

Figure 18. Seiche distribution along Lake Baikal (upper) and seasonal variations of Seiche amplitude in cm (lower) [Baikal Atlas, 1993].

Ocean tide loading displacement modelling: Accuracy assessment

Nigel T. Penna[1], Machiel S. Bos[2], Trevor F. Baker[3] and Hans-Georg Scherneck[4]

[1] School of Civil Engineering and Geosciences, Newcastle University, Newcastle upon Tyne, NE1 7RU, UK
[2] CIIMAR, Rua dos Bragas 289, University of Porto, 4050 – 123 Porto, Portugal
[3] Proudman Oceanographic Laboratory, 6 Brownlow Street, Liverpool, L3 5DA, UK
[4] Chalmers University of Technology, Department of Radio and Space Science, SE-412-96 Göteborg, Sweden, E-mail hgs@chalmers.se

Extended abstract

Different convolution methods used in the computation of ocean tide loading (OTL) displacement values are employed in the different software packages developed, which include CARGA (Bos and Baker, 2005), OLFG/OLMPP (Scherneck, 1991), SPOTL (Agnew, 1997) and GOTIC2 (Matsumoto et al, 2001). Their accuracy and suitability was assessed by us and detailed in Penna et al (2008), with this abstract providing a précis of the main findings of that paper. An extensive comparison of the usually dominant M2 OTL height displacement values was undertaken, firstly for a global distribution of 387 IGS sites, and also for a 0.125° grid across north-west Europe, that encompassed complicated coastlines and shallow seas, where ocean tide modelling is difficult. The values were computed using the CARGA, OLFG/OLMPP and SPOTL softwares with a range of recent ocean tide models, namely GOT00.2 (Ray, 1999), FES99 (Lefèvre et al, 2002), NAO.99b (Matsumoto et al, 2000) and FES2004 (Lyard et al, 2006), which encompassed different resolution regular grids (0.5º for GOT00.2 and NAO.99b, 0.25° for FES99 and 0.125° for FES2004). Furthermore, GOT00.2 and FES99 are the models recommended in the IERS 2003 conventions (McCarthy and Petit, 2004), and FES2004 is one of the two models recommended in their unratified updates. The OLFG/OLMPP software considered is particularly relevant since it drives the 'OTL web provider' (http://www.oso.chalmers.se/~loading/) recommended for OTL displacement computation in the IERS 2003 conventions and their unratified updates, and has therefore been used in many geodetic and geophysical studies.

Convolution method errors have traditionally been considered to have a much smaller contribution to the OTL displacement error budget (2-5% according to Bos and Baker (2005) and Agnew (1997), based on studies of inland gravity sites) than ocean tide model errors. To improve the convolution scheme, loading grids are refined and interpolated from the global model to fit the coastline, especially near an observing site. Penna et al (2008) summarised the different grid refinement methods employed by CARGA, OLFG/OLMPP and SPOTL, and, for the version of OLFG/OLMPP available since August 2007, demonstrated that excellent agreement arises between all three softwares for both the globally distributed IGS sites (only considered FES99 and FES2004 ocean tide models) and the north-west Europe grid (considered all four ocean tide models). Vector differences of M2 OTL height displacements between the three softwares for all four ocean tide models were invariably at the millimetre level or less for coastal sites, and less than 0.2 mm for sites more than ~150 km inland.

Before August 2007, for sites within ~150 km of the coastline, in addition to refining the ocean tide model grid by interpolation, the OLFG/OLMPP software employed a further requirement whereby local water mass redistribution (MRD) was undertaken to ensure constant water mass within the area of refinement (Scherneck, 1991). The MRD procedure was intended to improve the coastline of purely hydrodynamic models, since by construction their mass is conserved, and change of area near a coast is anticipated to have only a secondary effect on the oscillation systems in the basins.

Due to an unfortunate flag setting, MRD was applied to all models, not only the purely hydrodynamic ones, and this resulted in pre-August 2007 M2 OTL height displacement vector differences between OLFG/OLMPP and both CARGA and SPOTL of up to 20% for coastal sites when using the FES99 or NAO.99b model, as reported by Penna et al (2008). With the finer resolution FES2004 model, the impact of MRD was negligible. The inappropriateness of MRD for the FES99, NAO.99b and GOT00.2 ocean tide models was confirmed by (ibid) from GPS observations, which also confirmed the equivalence and accuracy of OTL displacement values computed using any of CARGA, SPOTL and OLFG/OLMPP (August 2007 onwards). Following the work described in (ibid), the 'OTL web provider' was changed in August 2007 to remove the MRD option.

The factors contributing to the usually sub-millimetre differences exhibited between the OTL displacements obtained from CARGA, OLFG/OLMPP (August 2007 onwards) and SPOTL were considered by Penna et al (2008). Changing from the PREM Green's function (Francis and Mazzega, 1990) used by CARGA to the Gutenberg-Bullen Green's function (Farrell, 1972) used by OLFG/OLMPP led to changes in displacement of ~0.25 mm near coasts and less than 0.1 mm inland i.e. an agreement of 2-5%. Differences arise of about 2 mm around Antarctic since the coastlines of OLFG/OLMPP, taken from the GMT package (Wessel and Smith, 1998) follow along floating sections of the ice shelves, whereas CARGA employs a strictly land-sea dividing coastline. Other variations arise due to using different values for sea water density, affecting the displacements by up to 0.3 mm for sites where the M2 OTL displacement reaches up to around 30 mm. An impact of grid definition of the ocean tide models was found: a systematic difference of the loading effects between one group of grids that balance the fractions of land and sea, respectively, that intrude into the opposite-flagged grid cells, and ocean tide model grids that on average prefer to include coastal land in sea-flagged cells (the opposite has no representative). Finally, other causes of the differences can be attributed to the three softwares not using identical interpolation schemes: CARGA and SPOTL use bilinear, whereas OLFG/OLMPP uses parabolic (in contrast to what Penna et al. (2008) state).

It was confirmed by Penna et al (2008) that ocean tide model errors still contribute the largest portion of the OTL displacement error budget, by comparing M2 OTL height displacements computed using the CARGA software and each of the CSR4.0 (Eanes and Bettadpur, 1996), FES99, FES2004, GOT00.2, NAO.99b and TPXO6.2 (Egbert and Erofeeva, 2002) ocean tide models. The same 387 IGS sites considered for the software global comparisons were considered, and the RMS vector differences from the six-model mean were computed. Whilst at most of the inland sites, RMS agreements were less than 0.4 mm, at some coastal sites, differences exceeded 3 mm, and exceeded 1 mm at 25 sites. There was no one model which was found to be consistently discrepant, suggesting that at present there is not a single ocean tide model that performs the best globally.

Whilst Penna et al (2008) only considered OTL displacement, the community of tide gravity researchers in tidal gravimetry is encouraged to utilise the gravity option of the OTL web provider. Loading effects for gravity are computed equivalently to radial displacement with respect of sub-gridding for coastal stations. Farrell's gravity Green's function can be convolved over each of the 18 global ocean models currently installed. The attraction effect at topographic height is included. However, we caution that the sub-gridding and refinement to the GMT full-resolution coastline at stations within 1 km of the coast or with viewing angles to the coast of more than 5º sub-horizontal, may incur limitations in precision. We look forward to a cooperative effort in a systematic evaluation.

References

Agnew DC (1997) NLOADF: A program for computing ocean-tide loading. J Geophys Res 102(B3):5109-5110

Bos MS, Baker TF (2005) An estimate of the errors in gravity ocean tide loading computations. J Geod 79(13):50-63

Eanes RJ, Bettadpur S (1996) The CSR3.0 Global Ocean Tide Model: Diurnal and Semi-Diurnal Ocean Tides from TOPEX/POSEIDON Altimetry. CSR-TM-9605 The University of Texas Center for Space Research

Egbert GD, Erofeeva SY (2002) Efficient inverse modeling of barotropic ocean tides. J Atm Oceano Tech 19(2):183-204

Farrell WE (1972) Deformation of the Earth by surface loads. Rev Geophys Space Phys 10(3):761--797

Francis O, Mazzega P (1990) Global charts of ocean tide loading effects. J Geophys Res 95(C7):11411-11424

Lefèvre F, Lyard FH, Le Provost C, Schrama EJO (2002) FES99: A global tide finite element solutions assimilating tide gauge and altimetric information. J Atmos Ocean Technol, 19(9):1345-1356

Lyard F, Lefèvre F, Letellier T, Francis O (2006) Modelling the global ocean tides: Modern insights from FES2004. Ocean Dynam 56(5-6):394-415

Matsumoto K, Takanezawa T, Ooe M (2000) Ocean tide models developed by assimilating TOPEX/POSEIDON altimeter data into hydrodynamical model: A global model and a regional model around Japan. J Oceanogr 56:567581

Matsumoto K, Sato T, Takanezawa T, Ooe M (2001) GOTIC2: A program for computation of oceanic tidal loading effect. J Geod Soc Japan 47:243-248

McCarthy DD, Petit G (2004) IERS Conventions 2003. IERS Technical Note 32.

Penna NT, Bos MS, Baker TF, Scherneck, H-G (2008) Assessing the accuracy of predicted ocean tide loading displacement values. J Geod 82(12):893--907, doi:10.1007/s00190-008-0220-2.

Ray RD (1999) A global ocean tide model from TOPEX/POSEIDON altimetry: GOT99.2. NASA Tech Memo TM-209478, 58 pp

Scherneck H-G (1991) A parametrized solid earth tide model and ocean tide loading effects for global geodetic base-line measurements. Geophys J Int 106(3):677-694

Wessel P, Smith WHF (1998) New, improved versions of the Generic Mapping Tools released. Eos Trans AGU 79(47):579

Limitations of
High Precision Tidal Prediction

B. Ducarme
Royal Observatory of Belgium, Av. Circulaire 3, B-1180 Brussels
Institut d'Astronomie et de Géophysique Georges Lemaître,
Université Catholique de Louvain, Chemin du Cyclotron 2, B-1348 Louvain-la-Neuve
bf.ducarme@gmail.com

ABSTRACT : The most demanding applications are tidal gravity predictions. We examine if the nms^{-2} precision can be reached. It correspond roughly to a 4.10^{-4} of the tidal range (TR) at mid latitude. High precision tidal prediction requires either tidal factors derived from tidal observations or modelled tidal factors based on the response of the Earth to tidal forces and on the ocean tides contribution. Both methods rely on a precise knowledge of the astronomical tides. The accuracy of the astronomical tides is very large and different tidal prediction programs agree within 10^{-5}TR. A reduced tidal development (1200 terms in Tamura) still insures a precision of 2.10^{-4}TR. For tidal predictions based on observations the calibration is the main limiting factor and 0.1% remains a target still difficult to reach. The records length limits the separation of the different tidal groups. If the tidal factors of different tidal waves within the same group are not the same, systematic errors are introduced. For example neglecting the resonance around ψ_1 in the K_1 group, can introduce an error at the level of 3.10^{-4}TR. For tidal predictions based on modelled tidal factors the choice of the model for the response of the Earth to tidal forces is critical as differences between recent models are slightly larger than 0.1%. The best models seem to fit the observations within 5.10^{-4}. The evaluation of the indirect effect of the ocean tides is critical and general conclusions are only valid at distances larger than 100km from the coast, where improved grid is not compulsory for tidal loading computations. In the best cases we can reach a precision of 5.10^{-4}TR. Our conclusion is that the accuracy of 0.1% is generally difficult to reach and that 5.10^{-4} is nowadays the limit of accuracy using long series of observations of regularly calibrated instruments.

Keywords: tidal predictions, body tides, astronomical tides, ocean tides loading

1. Introduction:

Among the different applications of tidal prediction tidal gravity is the most demanding one. Absolute gravity measurements reach nowadays a precision of 10^{-9}g or $10nms^{-2}$ (1µgal). A good metrological practice requires an accuracy 10 times better for all the corrections to be applied, including tidal gravity corrections. Tidal predictions should reach an accuracy of $1nms^{-2}$, which corresponds roughly to a 4.10^{-4} of a $2{,}500nms^{-2}$ (250µgal) tidal range (TR). Moreover long period (LP) tides have to be included. However as high precision absolute measurements require observations during one day or more, a large part of the tidal effect is averaged out, but not the LP tides. For gravity prospecting the measurements are always differential and the precision required is one order of magnitude lower. As a matter of fact tidal predictions with an accuracy of 0.1% will generally be sufficient. However in the following considerations we shall check if the level of the nms^{-2} (4.10^{-4}TR) can be reached. The considerations developed for gravity tides can be easily extrapolated for the other tidal components. Another point is that we should consider here the maximum discrepancy and not the standard deviation of the tidal prediction The reason is that in gravity prospecting we

consider isolated values. As pointed above absolute measurements are the exception as they average the short period tides.

Astronomical tides are very accurately computed from tidal potential developments (see section 2), but for an elastic Earth it is necessary to take into account the deformation of the Earth and the additional change of potential induced by this deformation. The result is known as "body tides". For gravity, the amplitude change is expressed by the ratio δ_E between the tides on the elastic Earth and the amplitude of the astronomical tides A_{th}. As the tidal forces are applied also to the fluid parts of the Earth i.e. the ocean and the atmosphere, the reaction of these fluids produces additional gravity, tilt and strain changes superimposed exactly on the frequencies of the body tides. After correction of the atmospheric effects, the different constituents of the tidal effects at a given tidal frequency can be represented by rotating vectors (Fig. 1).

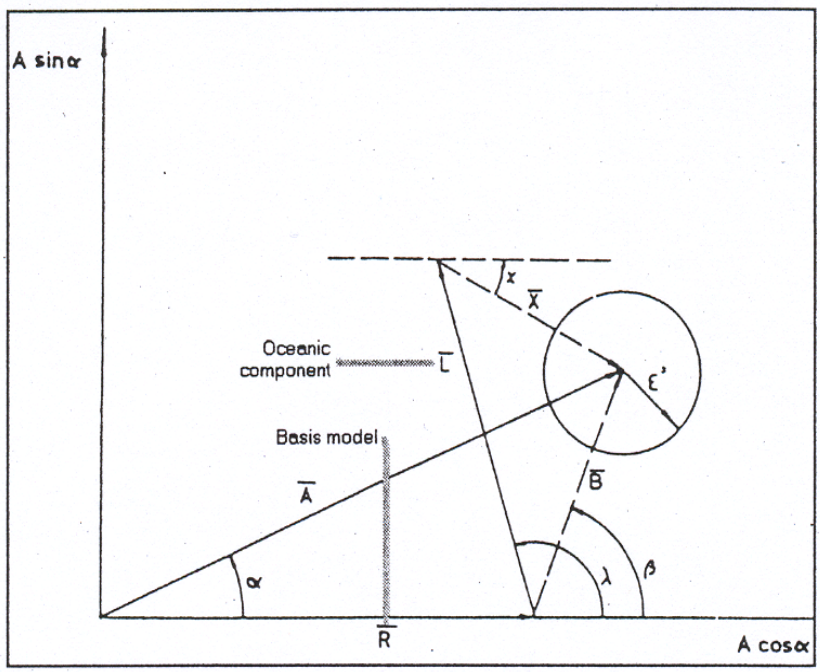

Figure 1: Phasor plot at a given tidal frequency showing the relationship between the observed tidal amplitude vector **A**(A,α), the Earth model **R**(R,0), the computed ocean tides load vector **L**(L,λ), the tidal residue **B**(B,β)=**A**-**R** and the corrected residue **X**(X,χ)=**B**-**L**, after Melchior (1994). See the text for further explanation.

Let us consider:

• the observed amplitude vector

A = ($\delta A t_h$,α), where δ is the observed tidal amplitude factor and α is the observed phase difference;

• the body tides tidal amplitude vector

R=($\delta_E A_{th}$,0), where δ_E is the expected tidal amplitude factor according to a given Earth model;

• the ocean load vector

L(L,λ) indirect effect computed from a given ocean tide model

For tidal prediction we can follow two approaches:

• a direct approach based on the tidal factors (δ,α), derived from tidal records.

• an indirect approach based on predicted tidal factors (δ_m, α_m), derived from the modelled tidal vector

$$\mathbf{A_m}(\delta_m A_{th}, \alpha_m) = \mathbf{R}(\delta_E A_{th}, 0) + \mathbf{L}(L, \lambda) \quad (1)$$

The two approaches should be equivalent if:
-the instrument is well calibrated;
-the Earth response and the tidal loading are well modelled.
We shall first consider the different factors influencing the precision of the tidal prediction.
The accuracy of the determination of observed tidal factors depends on:
- the calibration of the instrument (section 3.1)
- the astronomical tides (section 2)
- the length of the tidal record (section 3.2)
For the predicted tidal factors we should take into account:
- the response of the Earth to tidal forces (section 4.1)
- the ocean tides contribution (section 4.2)
- the astronomical tides (section 2)
For tilt and strain it should be necessary to model also the topography and cavity effects besides ocean tides contributions.
As the astronomical tides computation is a common factor we shall first consider this topic.

2. Astronomical tides computations

The first factor determining the precision of the tidal predictions is the number of terms or tidal waves considered in the tidal development. A recent study of the most recent tidal developments by Kudryavtsev (2004) confirmed the increase of precision with the number of terms: RATGP95 (Roosbeek, 1996, 6,499 terms, 5ngal), HW95 (Hartmann and Wenzel, 1995, 12,935terms, 1.23ngal), KSM03 (Kudryavtsev, 2004, 28,806terms, 0.39ngal). HW95, used as a standard by the ETERNA software (Wenzel, 1996), insures thus a precision of 5.10^{-6}TR. A previous tidal development TAM1200 (Tamura,1987, 1,200 terms) is already correct at the level of 2.10^{-4}TR (Ducarme, 2006). It is still widely used in BYTAP-G (Tamura et al., 1991), VAV (Venedikov and Vieira, 2004), T-soft (Van Camp and Vauterin, 2005) and ICET software.

The first step of the tidal prediction is the precise evaluation of the direct influence of the Moon, the Sun and the planets, generally called the “astronomical tides”. It is based on the developments of the tidal potential (Melchior, 1978). To derive a tidal prediction we have to consider a scale factor often referred as “Doodson” constant, a geometrical part depending on the position at the surface of the Earth (geodetic coefficients), which is different for each tidal component, and the harmonic part, which is a sum of sinusoidal terms. The development of the tidal potential provides for each term a normalised amplitude and an argument which is a linear combination of the astronomical arguments of the celestial bodies. Only 6 arguments, chosen by Doodson, are required for the Luni-solar tides. Concerning the planetary influences, Tamura was the first to introduce tidal terms coming from Jupiter and Venus, arriving to a total of 8 arguments. Roosbeek and Hartmann-Wenzel introduced additional arguments for Mars, Mercury and Saturn to arrive to a total of 11 astronomic elements.
Comparisons between the ICET and ETERNA software can be found in Ducarme, 2006. The tidal prediction computed using the TAM1200 potential is equivalent in PREDICT (ETERNA) and MT80TW (ICET) to better than 10^{-5}TR.

3. Precision of the observed tidal factors

The main uncertainty on the observed tidal factors comes from the calibration of the instruments. If the record length is less than one year the liquid core resonance will produce spurious effects inside the K_1 group. It should be noted also that the LP tides are generally not well determined as they require very long tidal records. It is always possible to use modeled tidal factors to replace missing observed values. A discussion of the modeling of the LP tides will be given in section 4.2.

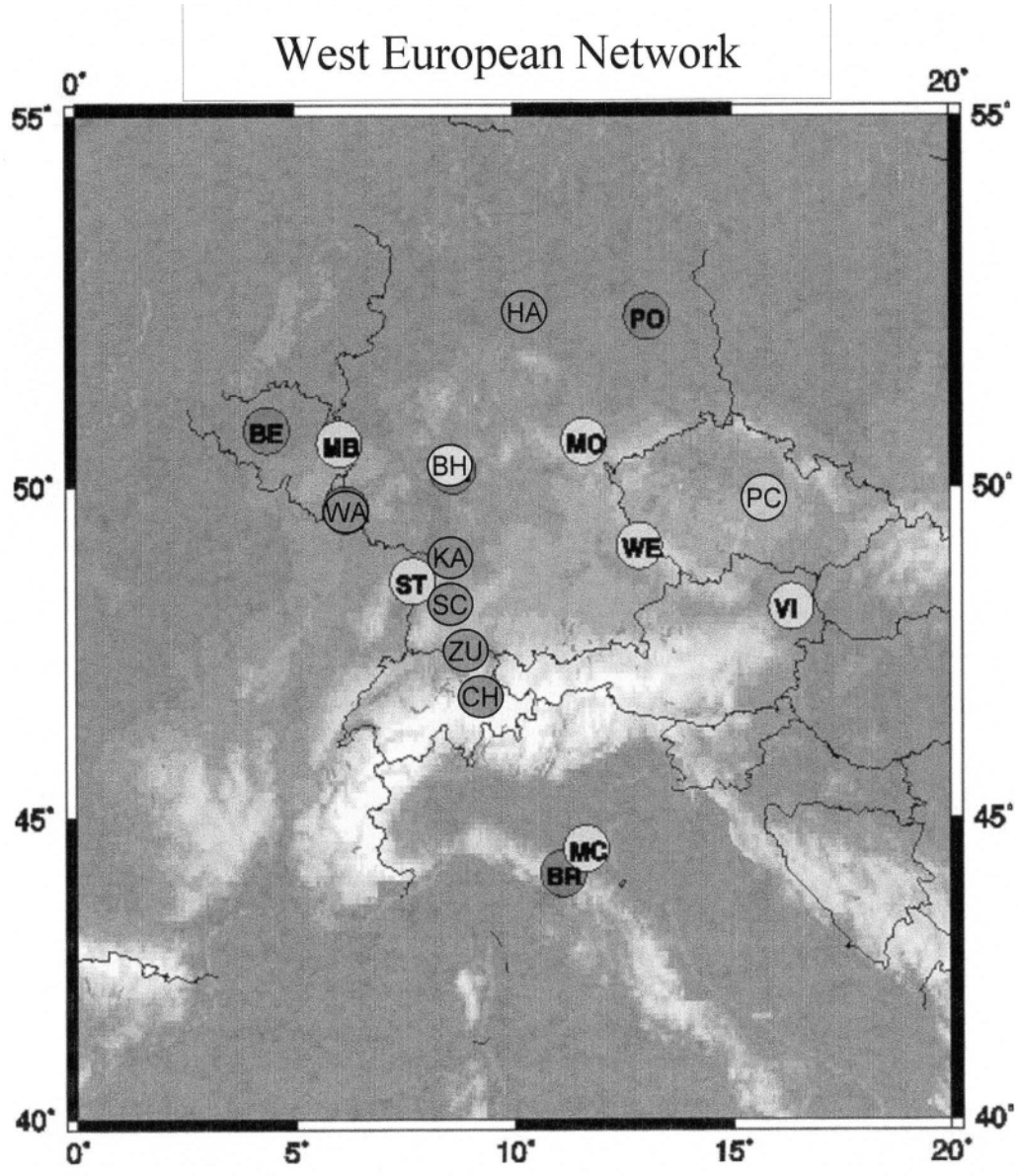

Figure 2. Selected stations in the West European network (Ducarme et al., 2008)

New GGP: MB (Membach), ST (Strasbourg), BH (Bad Homburg), MC (Medicina), MO (Moxa), WE (Wettzell), VI (Vienna).
Older stations: BE (Brussels), WA (Walferdange), KA (Karlsruhe), SC (Schiltach), ZU(Zürich), CH (Chur), HA (Hanover), PO (Potsdam), PC (Pecny).
BR (Brasimone) not used

3.1 Calibration of the gravimeters

It is necessary to model the instrument transfer function in amplitude and phase, at least at the tidal frequencies. Very precise techniques have been developed for the determination of the transfer function (Richter and Wenzel, 1991 ;Van Camp et al., 2000). Time lag corrections are precise at the level of the second i.e. 0.01° on M_2 or 2.10^{-4} TR at the equator. An extensive study including 16 tidal gravity station in Western Europe (Fig. 2) arrived to the conclusion that the level of 0.1% is already difficult to reach for the amplitude calibration (Ducarme et al., 2008b). This network is subdivided in two parts: 7 stations of the Global Geodynamics Project (GGP) (Crossley et al., 1999) equipped with modern "compact tidal" (CT) and "double sphere" (CD) superconducting gravimeters (SG) and 9 other ones, where older model T SG's or spring gravimeters were used.

The GGP SG's have been calibrated using parallel tidal recording with absolute FG5 gravimeters, as described in Francis (1997). Most of the instruments used in the additional stations have been calibrated against the Hanover vertical calibration line (Kangieser and Torge, 1981; Kangieser et al., 1983), either directly or indirectly.

The precision of a single calibration can be derived from the difference between the tidal factors obtained with collocated instruments. SG's simultaneously calibrated using the same absolute FG5 gravimeter show that the agreement is of the order of 0.05% (Ducarme et al., 2008b). Regularly repeated calibrations in Strasbourg lowered the RMS error to 0.03% (Rosat et al., 2008).

Referring to Figure 1, we can define the so called "corrected" tidal parameters: amplitude factor δ_c and phase difference α_c, by the relation.

$$\mathbf{A_c}(\delta_c A_{th}, \alpha_c) = \mathbf{A} - \mathbf{L} \qquad (2)$$

As the ocean tides loading is well constrained in this part of Europe, the variations observed in the corrected amplitude factors can be considered as reflecting the calibration errors. The standard deviation of the seven GGP stations calibrated with FG5 instruments is 0.08%. The dispersion of the nine additional stations is only slightly larger (Ducarme et al., 2008b).

A promising approach for the calibration of gravimeters is the use of inertial accelerations. For that purpose the instrument is placed on a platform and submitted to vertical accelerations at different frequencies. Such a platform was developed for spring gravimeters (van Ruymbeke,1989; van Ruymbeke et al., 2008). A precision of 0.1% has been achieved. For SG's the three usual supports are replaced by step motors which are gently lifting up and down the instrument in a sinusoidal way (Richter et al.,1995; Wilmes et al., 2008). All elements of the system are designed to insure a precision of 10^{-4}. However the precision is still limited to 0.05%.

As a conclusion we can state that the best precision achieved nowadays is:

•Superconducting gravimeters

- parallel registration with absolute gravimeters
  3.10^{-4} to 10^{-3}
- inertial accelerations
  scheduled 10^{-4} effective 0.510^{-3}

•Spring gravimeters

- vertical baseline 10^{-3}
- inertial accelerations 10^{-3}

It should be noted that the normalisation of spring gravimeters at a fundamental station, as it was realised for example during the Trans World Tidal Gravity Profiles (Melchior, 1994), did not generally insure a precision better than 3.10^{-3} (Ducarme et al., 2008a).

3.2 Effect of the record length

As the ocean tides loading is strongly frequency dependant, we cannot extrapolate the tidal factors obtained for one wave to a neighboring one. It is thus important to resolve a maximum of tidal groups to avoid systematic errors. Records shorter than 6 months should be avoided as the main waves P_1 and K_2 cannot be separated from their neighbors K_1 and S_2.
Moreover, due to the liquid core resonance, the Nearly Diurnal Free Wobble (NDFW) modifies the body tides amplitude factors inside the diurnal band (Melchior,1978; Dehant et al., 1999). The resonance effect is concentrated inside the K_1 group. A minimum time span of one year is required to resolve the complex tidal structure of this group, which includes the two annual (ψ_1 and S_1) and semi-annual (φ_1 and P_1) modulations of K_1. P_1 amplitude factor is reduced of 0.45%, and K_1 of 1.7%, while ψ_1 is amplified of 10% and φ_1 of 1.4%. If the record length is shorter than 6 months, the error will reach 7.10^{-4}TR at a latitude of 50°, due to the differential resonance between K_1 and P_1. Tidal records shorter than 1 year will not allow the separation of the annual modulations inside the K_1 group and produce residues at the level of 3.10^{-4}TR. However this effect can be strongly reduced by the introduction of a resonance model inside the group. It has been implemented in MT80TW.

4. Precision of predicted tidal factors

Besides the astronomical tides evaluation, the precision of the predicted tidal factors depends on the precision of the **R** and **L** vectors i.e. the precision of the body tides model and of the tidal loading computation.

4.1 The body tides models

Different body tides models are used by the different tidal prediction software.
•PREDICT is using latitude dependent tidal parameters for an elliptical, rotating, inelastic and oceanless Earth computed from the Wahr-Dehant-Zschau model (Dehant, 1987).
•MT80TW computes tidal predictions with δ_E values extracted from
- either (Dehant et al., 1999) :
  the DDW99 elastic (H)
  the DDW99 non-hydrostatic/inelastic (NH) models
- or the MAT01/NH inelastic (Mathews, 2001) model.

These models differ at the level of 10^{-3} (Table 1).
To discriminate the different theoretical models we compare the values of δ_E with the experimentally determined corrected amplitude factor δ_c computed by the relation (2).
A study based on the global GGP network (1997-2003) (Ducarme et al., 2007) provided a mean value $\delta_C(O_1) = 1.1546 \pm .0006$
It agrees within 0.1% with:
- the value $\delta_E = 1.1543$ computed from the DDW99/NH model
- and the value $\delta_E = 1.1540$ given by MAT01

A more recent study of the West European network (Ducarme et al., 2008b, Fig. 2) gave:

•For O1 the value δ_C =1.15340±0.00023 falling between the DDW99/H (1.1528) and the MAT01/NH (1.1540) inelastic models.
•For M2 the value δ_C =1.16211±0.00020 fitting very well the DDW99/NH (1.1620) and MAT01/NH (1.1616) inelastic models.
• For K1 the mean result δ_C =1.13525±0.00032 fitting the MAT01/NH (1.1349) inelastic model to better than 0.05%.
The conclusion is that MAT01/NH inelastic model seems to be the best choice, with an error close to 5.10^{-4}.

Table 1: Theoretical amplitude factors at 45° latitude

	O1 δ_{th}	K1 δ_{th}	M2 δ_{th}	O1/K1	M2/O1
DDW/H	1.1528	1.1324	1.1605	1.0180	1.0067
MAT01/NH	1.1540	1.1349	1.1616	1.0168	1.0066
DDW/NH	1.1543	1.1345	1.1620	1.0174	1.0066

4.2 The tidal loading computation

In continental stations the loading effect is generally at the level of a few microgal for the main waves, but one can observe huge effects in coastal areas. Moreover the variation of the tidal factors for a given value of the load vector depends of the amplitude of the astronomical tides at this latitude. As the diurnal gravity tides vanish at the equator, the corresponding tidal factors are not reliable at low latitude. It is the same at very high latitudes for both diurnal and semi-diurnal tides. It is thus difficult to issue general statements concerning the precision of modeled tidal factors and our examples are taken from middle latitude stations.
The ocean tides models provide at least the 8 main diurnal (Q_1, O_1, P_1, K_1) and semi-diurnal (N_2, M_2, S_2, K_2) and the fortnightly tide M_f. These waves cover most of the tidal spectrum. However in the diurnal band the frequencies higher than 1.024cycle/day (periods lower than 23h45m), corresponding to the small constituents J_1 and OO_1, are not always available. As the contribution of these groups represents only 6.5% of the diurnal tides, we can use the body tides values as a first approximation.
The LP tides deserve a careful treatment. Two recent studies (Ducarme et al, 2004; Boy et al, 2006) showed that, for the fortnightly lunar wave M_f, the tidal loading computations based on recent ocean tides models were in agreement with tidal gravity observations of superconducting gravimeters performed in the frame of GGP. The observations cannot determine precisely enough the monthly lunar wave M_m so that it is not yet possible to confirm its modelling. However Boy et al. showed that the ratio of the tidal loading vectors **L** for M_m and M_f is roughly equal to their amplitude ratio in the gravity tides and that the phases are similar. We can thus include M_m and M_f in one and a same group. In Siberia (Ducarme et al., 2008a) the 3 recent models (NAO99, TPX06, FES04) agree closely for M_f with a standard deviation better than 0.1% in amplitude and 0.05° in phase.
For the annual and semi-annual solar waves Sa and Ssa the tidal loading is not the main perturbation. The contributions from meteorological and hydrogeological sources are preponderant. Tidal gravity analyses on GGP data sets determined observed tidal factors larger than 2 for Sa (see for example Ducarme et al, 2006), while global models are required for effective pressure corrections (Neumeyer et al., 2004) and continental water storage fluctuations induce strong seasonal effects (Peter et al, 1995; Neumeyer et al, 2006). As these very long period tidal waves deserve a special treatment we suggest to use the body tides model values for tidal predictions.

The constant tidal effect called M_0S_0 should be treated with a special care in order to follow the resolutions of the International Association of Geodesy (IAG). For Gravity one should follow the "zero tide" correction principle i.e. one should remove only the astronomical part of the M_0S_0 tide and not the constant deformation. Clearly speaking the amplitude factor of M_0S_0 should be put equal to 1.
If tidal gravity observations have been performed in the area, it is often possible to select a best fitting ocean tides model, but generally the use of the mean of several models is largely improving the precision (Zahran, 2000; Zahran et al., 2005). In Figure 3 we consider 9 different ocean tides models (ORI96, CSR3, CSR4, FES95, FES02, FES04, NAO99, GOT00 and TPX06) and a sub-group of 6 more recent models (CSR4, FES02, FES04, GOT00, NAO99, ORI96, TPX06).

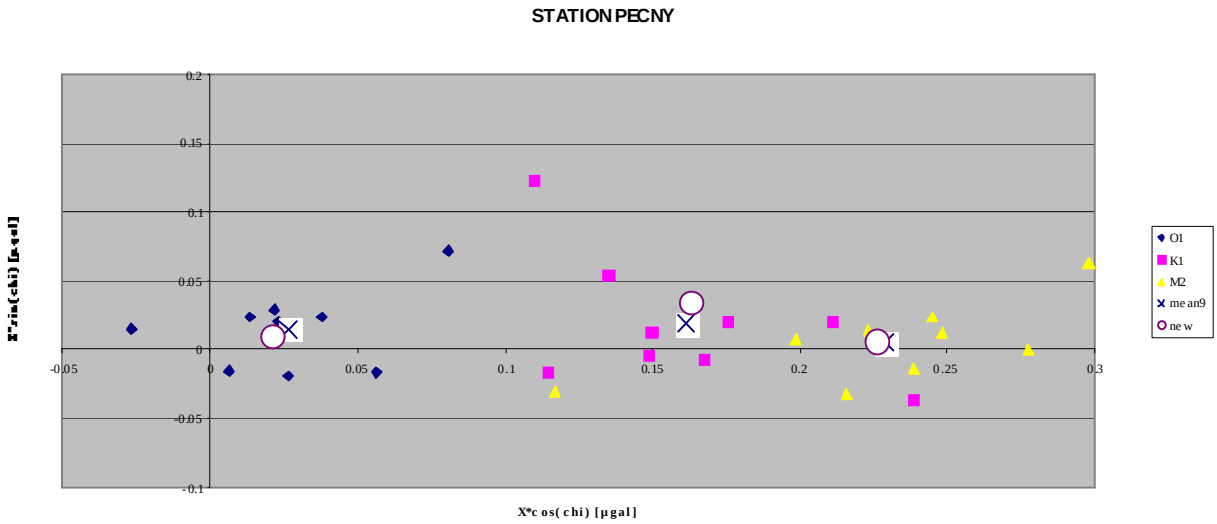

Figure 3: dispersion of the final residue **X** computed from 9 ocean tides models for a continental station (Pecny, CZ)
X: mean of 9 models, O: mean of 6 recent models

Let us consider the 16 European stations of Figure 2. The standard deviation of the 9 different ocean tides models is close to 0.3µgal for O_1 and M_2, i.e. 0.1% of the amplitude of these tidal waves. The use of the mean of 9 different models could reduce the accidental error contribution down to 3.10^{-4} of the tidal range.
Let us consider the trans-Siberian tidal gravity profile (TSP, Ducarme et al., 2008a). On the Siberian territory the tidal factors modelled using 9 different ocean tides models have a standard deviation close to 0.1% (0.05°) for the diurnal waves and 0.2% (0.1°) for M_2. Using the mean of 9 ocean tides models we can thus insure a precision of 0.03% (0.015°) in the diurnal band and 0.06% (0.03°) in the semi-diurnal one. The RMS error of 3 recent models of the LP tide M_f is lower than 0.025%. The global RMS error due to load computations can be kept below 5.10^{-4}TR.

The case of 4 gravity stations installed along the Atlantic coast of France (Timofeev et al., 2006), at 100km from the sea shore, is less favourable, due to the very large semi-diurnal ocean tides loading of the Gulf of Biscay. The standard deviation of the 9 different ocean tides models is close to 0.3µgal for O1, but it reaches 1µgal for M2! It follows that the use of the mean of 9 ocean tides models will still have a global uncertainty at the level of 0.2µgal, close to 10^{-3}TR. Among the different ocean tide models the best fit with the observed tidal factors

was obtained using CSR3, CSR4 or FES02 with less than 0.05% in amplitude and 0.1° in phase.
We can conclude that the use of the mean of several tidal models can reduce the uncertainty to 5.10^{-4}TR for inland stations in well constrained areas, but that at 100km from the coast the uncertainty can easily reach 10^{-3}TR.

5. Statements concerning the final precision

For each of the two approaches we can draw a table giving the best precision that can be reached as well as the normal one. The three main contributions are listed together with the expected global precision. For the astronomical tides usual means that the TAM1200 tidal potential is used.
Table 2 presents the case of the observed tidal factors. As expected the main error source is the calibration. A precision better than 5.10^{-4} was only achieved by the SG of Strasbourg. It is probably more realistic to consider a precision of 0.1% for the time being. At this level of precision a reduced tidal development is sufficient for the astronomical tides computation.
For spring gravimeters only the best instruments can insure a precision of 0.1%. A more conservative figure is 0.3%.
For the modeled tidal factors (Table 3) the two main error sources are the tidal loading evaluation and the uncertainties on the response of the Earth to the tidal forces. Even in the best case the error budget is close to 0.1%. For coastal stations the error on tidal loading evaluation is very difficult to estimate. Tidal gravity observations can help to determine the best models for the considered region.

Table 2: Precision on the observed tidal factors for superconducting gravimeters (SG) and spring gravimeters

Calibration		Astr. tides		Rec.length		Total	
best	usual	best	usual	>1y.	<1y.	best	usual
SG							
$\leq 5.10^{-4}$	10^{-3}	5.10^{-6}	2.10^{-4}	-	3.10^{-4}	$\leq 5.10^{-4}$	10^{-3}
spring							
10^{-3}	3.10^{-3}	5.10^{-6}	2.10^{-4}	-	3.10^{-4}	10^{-3}	3.10^{-3}

Table 3: Precision of the modelled tidal factors

Loading		Earth mod.		Astr. tides		Total	
inland	<100km	best	any	best	usual	best	usual
5.10^{-4}	$>10^{-3}$	5.10^{-4}	10^{-3}	5.10^{-6}	2.10^{-4}	7.10^{-4}	$>10^{-3}$

6. ICET contribution

Which approach is the most efficient?
•The determination of precise observed tidal parameters is time consuming and requires expensive instruments.
•Modelled tidal parameters are inexpensive to compute but unreliable for coastal stations.
The International Centre for Earth Tides (ICET) prepared two kinds of modelled tidal factors, available from its web site http://www.upf.pf/ICET/.

For 1,000 stations around the world very precise tidal parameters based on different means of ocean tides models are proposed. We computed modeled tidal factors using 9 different ocean tides models (ORI96, CSR3, CSR4, FES95, FES02, FES04, NAO99, GOT00 and TPX06). The tidal loading vector **L** was evaluated by performing a convolution integral between the ocean tide models and the load Green's function computed by Farrell (1972). The Green's functions are tabulated according to the angular distance between the station and the load. The water mass is condensed at the center of each cell and the Green's function is interpolated according to the angular distance. This computation is rather delicate for coastal stations if the models are computed on a coarse grid, as the stations can be located very close to the center of the cell. The numerical effect can be largely overestimated. To avoid this problem our tidal loading computation checks the position of the station with respect to the center of the grid. If the station is located inside the cell, this cell is eliminated from the integration and the result is considered as not reliable (Melchior et al., 1980). We can consider two groups of models, the older models up to 1996 (ORI96, CSR3, FES95) on one hand, and the new generation of models (CSR4, FES02, FES04, GOTOO, NA099 and TPX06) on the other. For the first generation of models, the effect of the imperfect mass conservation is corrected on the basis of the code developed by Moens (Melchior et al., 1980). Following Zahran's (2000, 2005) suggestion, we computed mean tidal loadings for different combinations of models: all the 9 models or only the 6 recent ones.
As many of the ocean tide models do not provide the smaller tidal constituents J_1, OO_1, M_3, M_4, we provide only the theoretical amplitude factors of the corresponding groups. For the long period constituents we use always the mean of the 3 recent models NAO99, TPX06 and FES04 to compute the loading for the fortnightly tide M_f and we include the monthly tide M_m as well as the shorter period tides in one and the same group M_f. As explained in section 4.1, we use the body tides model values for the annual and semi-annual solar waves Sa and Ssa.
To evaluate the real precision of the prediction based on modelled tidal factors we compared it with a prediction based on observed tidal factors in one of the best calibrated stations: Moxa

(Fig. 2). The tidal coefficients are given in Table 4. Due to the large difference in the tidal parameters for the Ssa group, a strong semi-annual wave shows up with an amplitude of $2nms^{-2}$ in the difference between the two tidal predictions (Figure 4). For the shorter periods the differences does not exceed $\pm 3nms^{-2}$, i.e. 1.2 10^{-3}TR. There is a scale difference of 4.10^{-4} producing a systematic effect of $\pm 0.5nms^{-2}$. It is a mixture of the errors due to the inaccuracy of the calibration and of the body tides model. The residual error is close to $\pm 2.5nms^{-2}$ i.e. 0.1% and corresponds principally to the inaccuracy of the ocean tides computation. The associated standard deviation is only $1nms^{-2}$ (4.10^{-4}TR). If we do not consider the LP tides, the error on the tidal correction of absolute gravity determinations obtained by observations averaged on several days will be of the same order of magnitude. It justifies the statement made in the introduction .

For less accurate tidal predictions we propose global tidal gravity parameters on a 0.5°x0.5° grid using the CSR3 or NAO99 ocean tide model for 9 waves (M_f, Q_1, O_1, P_1, K_1, N_2, M_2, S_2, K_2). Zhou J.C. et al. (2007) used the CSR3 ocean tides model together with a purely elastic Earth model. Ocean load vectors have been computed using the Agnew (1996, 1997) software. The NAO99 model was used at ICET with the Melchior et al. (1980) software. The computed load vectors were associated to a non hydrostatic/inelastic Earth model (Dehant et al., 1999) to compute modeled tidal parameters.

Interpolation software is proposed on the ICET WEB site to provide an output compatible with the most common tidal prediction software. The proposed software is an update of the WPAREX program developed by H. G. Wenzel for a bilinear interpolation inside the grid. If the input coordinates are not surrounded by 4 grid points error message is issued and the values at the closest point are selected..

If one of the grid points is too close from one cell of the ocean tides model a warning is issued, as the load vector computation is probably not accurate at this point.

Table 4: Observed (δ, α) and modelled (δ_m, α_m) tidal gravity factors for station Moxa.
N: number of waves in Tamura, 1987

Tidal Group	N	Frequency range (cycle per day)		δ	α (°)	δ_m	α_m (°)
						DDW99/NH 6 recent models	
M0S0	2	.000000	.000001	1.0000	0.000	1.0000	0.000
Ssa	32	.000002	.020884	1.2358	0.760	1.1570	0.000
Mf	247	.020884	.501369	1.1454	0.450	1.1411	0.410
Q1	143	.501370	.911390	1.1461	-0.186	1.1468	-0.132
O1	106	.911391	.981854	1.1488	0.124	1.1501	0.097
P1	17	.981855	.998631	1.1493	0.179	1.1503	0.161
K1	40	.998632	1.023622	1.1363	0.224	1.1358	0.156
J1	43	1.023623	1.044800	1.1566	0.166	1.1560	0.000
OO1	102	1.064841	1.470243	1.1535	0.118	1.1560	0.000
N2	149	1.470244	1.914128	1.1762	2.167	1.1784	2.062
M2	95	1.914129	1.984282	1.1850	1.581	1.1859	1.510
S2	17	1.984283	2.002736	1.1835	0.344	1.1866	0.607
K2	116	2.002737	2.451943	1.1859	0.581	1.1838	0.546
M3	81	2.451944	3.381378	1.0695	0.454	1.0700	0.000

Systematic comparisons between the precisely computed and the interpolated tidal gravity parameters for 24 GGP stations around the world showed that the differences on the mean amplitude factors are small i.e. less than 4.10^{-4} (Zhou J.C. et al., 2007). However the interpolated tidal parameters may become questionable at very high latitude or for the diurnal waves at the equator (section 4.2).

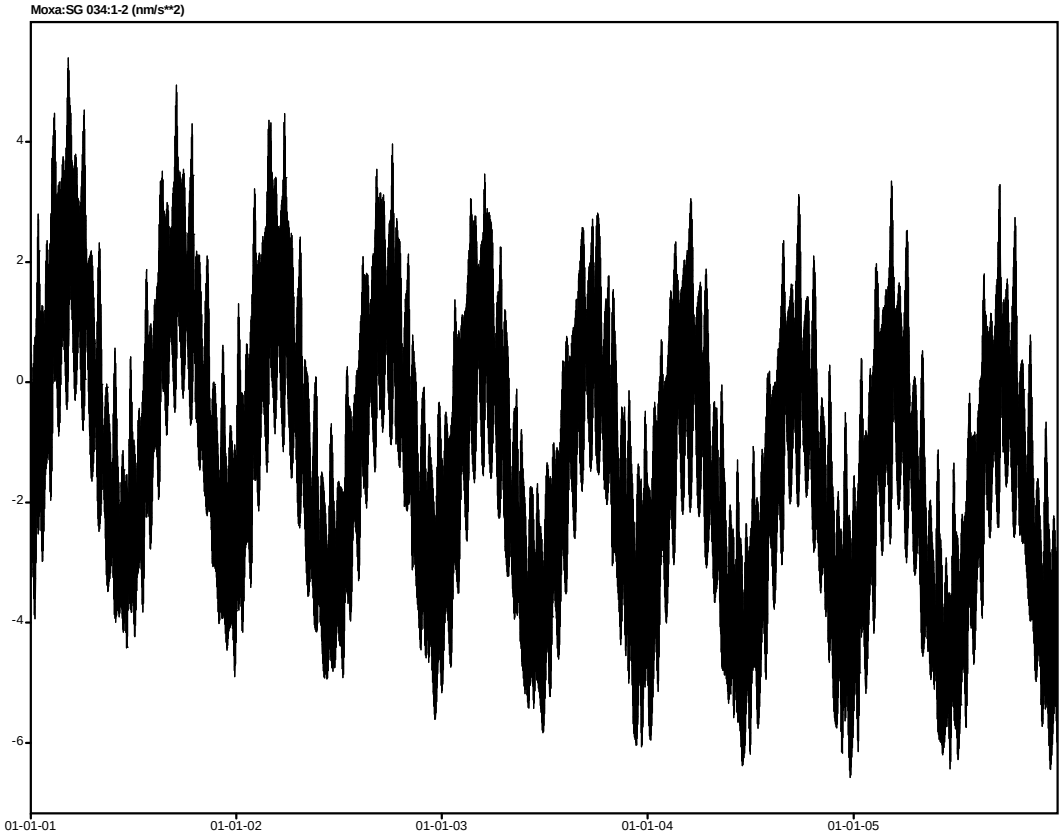

Figure 4. Difference between tidal prediction using the observed tidal parameters at Moxa and a modelling based on the DDW99/NH body tides model and the mean of 6 recent ocean tides models (Table 4). Units are nms^{-2}

7. Conclusions

The final accuracy of tidal prediction based on previous tidal observations depends on the correct evaluation of the astronomical tides, the length of the tidal records and the accuracy of the calibration of the instrument.

Tidal predictions can also be performed on the grounds of "predicted tidal factors". The different elements contributing to the precision of such tidal predictions are:

- the astronomical tides;
- the response of the Earth to the tidal force;
- the ocean tides contribution.

The accuracy of the astronomical tides is very large and different tidal prediction programs agree within 10^{-5} of the tidal range (TR). A reduced tidal development (1200 terms in Tamura) still insures a precision of 2.10^{-4} TR.

For tidal prediction based on observation the records length limits the separation of the different tidal groups. If the tidal factors of different tidal waves within the same group are not

the same, systematic errors are introduced. The two main sources of difference between waves with close frequencies are the FCN in the diurnal band and differential ocean tides effects. Neglecting the resonance around ψ_1, can introduce an error at the level of 3.10^{-4}. Differential ocean tides effect depends on the magnitude of the local effects.
The calibration remains thus the main limiting factor and 0.1% remains a target still difficult to reach. The standard deviation on the corrected tidal factors of 16 selected stations in Europe reaches 0.1% in amplitude and 0.02° in phase.

For tidal predictions based on modelled tidal factors the choice of the model for the response of the Earth to tidal forces is critical as difference between recent models are slightly larger than 0.1%. Investigations based on 16 stations in western Europe showed that the MAT01 model fits the observations within 0.05% for O_1 as well as for M_2.
The tidal loading evaluation is critical and general conclusions are only valid at distances larger than 100km from the coast, where improved grid is not compulsory for tidal loading evaluation. We present case studies for Europe and Siberia. In the best cases we can reach a precision of 0.05%. In these areas the global error due to Earth model and tidal loading is thus below 0.1%. This level of precision is confirmed by tests performed on one of the best GGP station.
Up to now it is thus quite impossible to reach an accuracy of 4.10^{-4}TR for tidal prediction on a real Earth. It is even difficult to reach 10^{-3}TR, which is suitable for tidal correction of absolute gravity observations. At this level of precision a reduced tidal development is sufficient for the computation of astronomical tides. The modelling of tides with periods larger than 6 months is still unreliable.
As it is much less expensive to compute modelled tidal factors than to perform tidal gravity observations, the International Centre for Earth Tides (ICET) prepared two kinds of modelled tidal factors, available from its web site http://www.upf.pf/ICET/. For 1,000 stations around the world very precise tidal parameters based on different means of ocean tides models were computed. For less accurate tidal predictions we propose global tidal gravity parameters on a 0.5°x0.5° grid using the CSR3 or the NAO99 ocean tide model for 9 waves (M_f, Q_1, O_1, P_1, K_1, N_2, M_2, S_2, K_2). An interpolation software is also available.

Acknowledgements

The author had fruitful discussions with O. Francis concerning tidal predictions suitable for absolute gravity measurements and with H. Wilmes on the precision reached by the inertial calibrating method for superconducting gravimeters.

Bibliography

Agnew, D.C., 1996, SPOTL: some programs for ocean tide loading. SIO Reference series 96-8, scripts institution of oceanography, Woods Hole
Agnew, D.C., 1997: NLOADF: a program for computing ocean-tide loading. J. Geophys. Res., 102 (B3), 5109-5110.
Boy J.P., Llubes M., Ray R., Hinderer J., Florsch N., 2006: Validation of long-period oceanic tidal models with superconducting gravimeters. J. of Geodynamics, 41, 112-118.
Crossley, D., Hinderer, J., Casula, G., Francis, O., Hsu, H. T., Imanishi, Y., Jentzsch, G., Kääriaïnen, J., Merriam, J., Meurers, B., Neumeyer, J., Richter, B., Shibuya, K., Sato, T., Van Dam, T., 1999: Network of superconducting gravimeters benefits a number of disciplines. EOS, 80, 11, 121/125-126.
Dehant, V., 1987: Tidal parameters for an inelastic Earth. Physics of the Earth and Planetary Interiors, 49, 97-116, 1987.

Dehant V., Defraigne P., Wahr J., 1999: Tides for a convective Earth. J. Geoph. Res., 104, B1, 1035-1058.
Ducarme B., Venedikov A.P., Arnoso J., Vieira R., 2004: Determination of the long period tidal waves in the GGP superconducting gravity data. Journal of Geodynamics, 38, 307-324
Ducarme, B., 2006: Comparison of some tidal prediction programs and accuracy assessment of tidal gravity predictions. Bull. Inf. Marées Terrestres, 141, 11175-11184
Ducarme, B., Neumeyer, J., Vandercoilden, L., Venedikov, A. P., 2006: The analysis of long period tides by ETERNA and VAV programs with or without 3D pressure correction. Bull. Inf. Marées Terrestres, 141, 11201-11210
Ducarme, B., Sun, H. P., Xu, J. Q., 2007 : Determination of the free core nutation period from tidal gravity observations of the GGP superconducting gravimeter network. Journal of Geodesy, 81, 179-187 *(DOI: 10.1007/s00190-006-0098-9)*
Ducarme, B., Timofeev, V. Y., Everaerts, M., Gornov, P. Y., Parovishnii, V. A., van Ruymbeke, M., 2008a: A Trans Siberian tidal gravity profile (TSP) for the validation of tidal gravity loading corrections. J. of Geodynamics,45, 73-82, *(DOI:10.1016/j.jog.2007.07.001)*
Ducarme, B., Rosat, S., Xu, J.Q., Vandercoilden, L., Sun, H.P., 2008b: European tidal gravity observations: Comparison with Earth Tides models and estimation of the Free Core Nutation (FCN) parameters. Accepted for publication in IAG Proc., Symp. GS003 "Earth Rotation and Geodynamics", XXIV IUGG General Assembly, Perugia, I.
Farrell, W.E., 1972: Deformation of the Earth by surface load. Rev. Geophys., 10, 761-779
Francis, O., 1997: Calibration of the C021 superconducting gravimeter in Membach (Belgium) using 47 days of absolute gravity measurements. International association of Geodesy Symp., Gravity, Geoid and Marine Geodesy, Segawa et al. (eds.), 117, 212-219
Hartmann, T. and Wenzel H.-G., 1995: Catalogue HW95 of the tide generating potential. Bull. Inf. Marées Terrestres, 123, 9278-9301.
Kangieser, E., Torge, W., 1981: Calibration of LaCoste-Romberg gravity meters, Model G and D. Bull. Inf. Bur. Grav. Int., 49,50-63.
Kangieser, E., Kummer K., Torge, W., Wenzel H.-G, 1983: Das Gravimeter-Eichsystem Hanover. Wissenschaftliche Arbeiten der Fachrichtung Vermessungswesen der Universität Hannover, 1203
Kudryavtsev, S.M., 2004: Improved harmonic development of the Earth tide generating potential. J. of Geodesy, 77, 229-838
Mathews, P.M., 2001: Love numbers and gravimetric factor for diurnal tides. Proc. 14th Int. Symp. on Earth Tides, Journal of the Geodetic Society of Japan, 47, 1, 231-236.
Melchior, P., 1978: The tides of the planet Earth. Pergamon Press, 609pp.
Melchior P., Moens M., Ducarme B., 1980: Computations of tidal gravity loading and attraction effects. Bull Obs. Marées Terrestres, Obs. Roy. Belg., 4, 5, 95-133.
Melchior, P., 1994: A new data bank for tidal gravity measurements (DB92). Physics Earth Planet. Interiors, 82, 125-155.
Neumeyer J., Hagedorn J., Leitloff J., Schmidt T., 2004: Gravity reduction with three-dimensional atmospheric pressure data for precise ground gravity measurements. Journal of Geodynamics, 38, 437-450.
Neumeyer, J., Schmidt, T., Stoeber, C., 2006: Improved determination of the atmospheric attraction with 3D air density data and its reduction on ground gravity measurements. IAG Symposia, Dynamic Planet 2005, Cairns, Australia, August 22-26 2005, 130, 541-548
Peter, G., Klopping, F.J., Berstis, K.J., 1995: Observing and modeling gravity changes caused by soil moisture and groundwater table variations with superconducting gravimeters in Richmond, Florida, U.S.A.. Cahiers du Centre Européen de Géodynamique et de Séismologie, 11, 147-158.

Richter, B. and Wenzel, H.-G., 1991: Precise instrumental phase lag determination by the step response method. Bull. Inf. Marées Terrestres, 111, 8032-8052.
Richter, B., Wilmes, H., Nowak, I., 1995: The Frankfurt calibration system for relative gravimeters. Metrologia, 32, 217-223.
Roosbeek, F., 1996: RATGP95: A harmonic development of the tide generating potential using an analytical method. Geoph. Journal Int., 126, 197-204.
Rosat, S., Boy, J., Ferhat, G., Hinderer, J., Amalvict, M., Gegout, P., Luck, B., 2008: Analysis of ten-year (1997-2007) record of time-varying gravity in Strasbourg using absolute and superconducting gravimeters: new results on the calibration and comparison with GPS. New Challenges in Earth's Dynamics, 1-5 Sept. 2008, Jena. To be published in Journal of Geodynamics.
Tamura Y., 1987: A harmonic development of the tide-generating potential. Bull. Inf; Marées Terrestres, 99, 6813-6855.
Tamura,Y., Sato, T., Ooe, M., Ishiguro, M., 1991: A Procedure for Tidal Analysis with a Bayesian Information Criterion, Geophysical Journal International, 104, 507-516.
Timofeev, V.Y., van Ruymbeke, M., Woppelmann, G., Everaerts, M., Zapreeva, E.A., Gornov, P.Y., Ducarme, B., 2006:Tidal gravity observations in Eastern Siberia and along the Atlantic coast of France. Proc. 15 Int. Symp. Earth Tides, J. Geodynamics, 41, 30-38.
Van Camp, M. Vauterin, P., Wenzel, H.G., Schott, P., Francis, O., 2000: Accurate transfer function determination for superconducting gravimeters, Geophys. Res. Let., **27**, 37-40.
Van Camp, M. and Vauterin P., 2005: Tsoft: graphical and interactive software for the analysis of time series and Earth tides. Computers & Geosciences, 31, 631-640.
van Ruymbeke, M., 1989: A calibration system for gravimeters using a sinusoidal acceleration resulting from a vertical periodic movement, Bull. Geod., 63, 223-235
van Ruymbeke, M., Naslin, M., Zhu, P., Noël, J., 2008: New developments in the calibration of gravitational instruments. Proc. New Challenges in Earth's Dynamics, 1-5 Sept. 2008, Jena. To be published in Journal of Geodynamics.
Venedikov, A.P., Vieira, R., 2004: Guidebook for the practical use of the computer program VAV – version 2003. Bull. Inf. Marées Terrestres, 139, 11037-11102.
Wenzel, H.-G., 1996: The nanogal software: Earth tide data processing package ETERNA 3.30. Bull. Inf. Marées Terrestres, 124, 9425-9439.
Wilmes, H., Nowak, I., Falk, R., Wziontek, H., 2008: Estimation of the transfer function and and calibration parameters of superconducting gravimeters. Proc. New Challenges in Earth's Dynamics, 1-5 Sept. 2008, Jena. To be published in Journal of Geodynamics.
Zahran, K.H., 2000: Accuracy assessment of Ocean Tide loading computations for precise geodetic observations. PhD thesis, Universität Hannover.
Zahran, K. H., Jentzsch, G., Seeber, G., 2005: World-wide synthetic tide parameters for gravity and vertical and horizontal displacements. J. Geod., 79, 293-299
Zhou J. C., Sun H. P., Ducarme B., 2007 : Validating the synthetic tidal gravity parameters with superconducting gravimeter observations. Bull. Inf. Marées Terrestres, 143, 11489-11497

Determination of degree-2 Love and Shida numbers from VLBI

H. Špičáková, J. Böhm, P.J. Mendes Cerveira, H. Schuh

Institute of Geodesy and Geophysics, Vienna University of Technology, Austria
hana@mars.hg.tuwien.ac.at

Abstract

Love and Shida numbers describe the Earth's response to external forces exerted by celestial bodies due to the elasticity of the Earth. Modern space geodetic techniques, such as VLBI (Very Long Baseline Interferometry), allow the empirical validation of theoretical Love and Shida numbers. In the VLBI analysis software package OCCAM tidal displacements on the Earth's surface are modelled according to the International Earth rotation and Reference systems Service (IERS) Conventions 2003. Snapshots of corrections to the nominal displacements for the complete Earth's surface with a spatial resolution of 1°x1° are shown.
Nominal degree-2 Love and Shida numbers, h_2 and l_2, were determined from the continuous 15 days VLBI campaign CONT05. Frequency dependence was considered in the diurnal band due to the retrograde Free Core Nutation (FCN) resonance: we determined h_2 and l_2 at those diurnal tidal waves with the largest amplitudes, two of them lying very close to the resonance frequency.

Keywords: Love number, Shida number, Tidal displacement, VLBI

1 Introduction

Lunisolar gravitational attraction causes rhythmic undulations of the Earth's surface. This tidal deformation arises from the variations in the Earth's gravitational field caused by the Moon/Sun over the surface of the Earth relative to its strength at the geocentre. The Earth deforms because it has a certain degree of elasticity. The Love number h and the Shida number l are dimensionless parameters, which characterize the ability of the Earth to react to tide-generating forces. If the Earth would be a completely rigid body, h and l would be equal to zero and there would be no tidal deformation of the surface. The total range of vertical surface deformation, which is caused by the pure solid Earth tides, can reach up to tens of centimetres.
Very Long Baseline Interferometry (VLBI) measures the difference between the arrival time of a plane radio wavefront emitted by an extragalactic source at two Earth-based antennas. The tidal deformation of the Earth surface is fully projected in the variation of the antenna position. Considering the steady improvements during the last two decades in the quality of observations, VLBI determines the relative position of the stations with an accuracy of a few millimetres. Therefore it is essential to have a precise model of the solid Earth tides displacement with sub-millimetre accuracy. The idea of this work is to reestimate parameters of elasticity of the solid Earth tide model. We used the model from Mathews et al. (1995), as recommended in the IERS Conventions 2003 (McCarthy and Petit, 2004). From the 15 days VLBI campaign CONT05 we determined nominal degree-2 Love and Shida numbers, and additionally Love numbers at six different frequencies in the diurnal band in order to demonstrate the feasibility of the approach.

2 Modelling tidal displacements

2.1 Tidal displacement with nominal Love and Shida number h_2 and l_2

Considering the Earth being "Spherical, Non-Rotating, Elastic and Isotropic", what is the most basic model, the tidal displacement (u_R, u_E, u_N) at a given station (latitude φ, longitude λ) in the local system (Radial, East, North) is described by equations (E1) to (E3). In this model the total tidal displacement is computed as the sum of displacement components over the spherical degree n of the tide generating potential V_n. For each spherical degree exists one proportionality factor for radial displacement (Love number h) and one proportionality factor for tangential displacement (Shida number l), which determines how strong is the effect of the potential component on the displacement. The parameter g stands for the surface acceleration due to gravity force. For practical computation we used expression of the tidal potential in Cartesian coordinates. The displacement component $\boldsymbol{u}^{(2)}$ (E4) to (E6) which is generated by the second degree potential is given by, e.g., Sovers et al. (1998). The tide generating potential is expressed there by the geocentric coordinates of the attracting body (X_a, Y_a, Z_a), the geocentric coordinates of the station (x_s, y_s, z_s), the vector $\boldsymbol{R_s}$ from the geocentre to the station, the vector $\boldsymbol{R_a}$ from the geocentre to the Moon/Sun and by the ratio of the mass of the attracting body to the mass of the Earth μ_a.

$$u_{\mathrm{R}} = \sum_{n=2}^{\infty} h_n \cdot \frac{1}{\mathrm{g}} \cdot V_n \qquad \text{(E1)}$$

$$u_{\mathrm{E}} = \sum_{n=2}^{\infty} l_n \cdot \frac{1}{\mathrm{g} \cdot \cos\varphi} \cdot \frac{\partial V_n}{\partial \lambda} \qquad \text{(E2)}$$

$$u_{\mathrm{N}} = \sum_{n=2}^{\infty} l_n \cdot \frac{1}{\mathrm{g}} \cdot \frac{\partial V_n}{\partial \varphi} \qquad \text{(E3)}$$

$$u_{\mathrm{R}}^{(2)} = h_2 \cdot \sum_a \frac{3\mu_a R_s^2}{R_a^5} \left[\frac{(\boldsymbol{R_s} \cdot \boldsymbol{R_a})^2}{2} - \frac{R_s^2 R_a^2}{6} \right] \qquad \text{(E4)}$$

$$u_{\mathrm{E}}^{(2)} = l_2 \cdot \sum_a \frac{3\mu_a R_s^3}{R_a^5} (\boldsymbol{R_s} \cdot \boldsymbol{R_a}) \frac{(x_s Y_a - y_s X_a)}{\sqrt{x_s^2 + y_s^2}} \qquad \text{(E5)}$$

$$u_{\mathrm{N}}^{(2)} = l_2 \cdot \sum_a \frac{3\mu_a R_s^2}{R_a^5} (\boldsymbol{R_s} \cdot \boldsymbol{R_a}) \left[\sqrt{x_s^2 + y_s^2}\, Z_a - \frac{z_s}{\sqrt{x_s^2 + y_s^2}} (x_s X_a + y_s Y_a) \right] \qquad \text{(E6)}$$

2.2 Corrections to the tidal displacement in radial direction with frequency dependent Love numbers $h_{21(f)}$

Under consideration of a more precise Earth model with fluid core and elastic mantle, the tidal response of the solid Earth becomes frequency dependent in the diurnal band. The rotational axis of the fluid core is slightly inclined with respect to the axis of rotation of the elastic mantle. In this situation forces arise at the elliptical core-mantle boundary, which try to realign the two axes and this leads to a resonance with the tidal force.
Corrections to radial displacement (E7) coming from the harmonic terms of the second degree tidal potential in the diurnal band (i.e., from the first order of the potential) are given in, e.g., McCarthy and Petit (2004).

$$\delta u_{\mathrm{R}(f)}^{(21)} = -\frac{3}{2}\sqrt{\frac{5}{24\pi}} H_f \delta h_{21(f)} \sin(2\varphi) \sin(\theta_f + \lambda) \qquad \text{(E7)}$$

with

H_f	Cartwright-Tayler amplitude of the tidal term,
$\delta h_{21(f)}$	difference of $h_{21}(f)$ from the nominal value h_2,
φ, λ	station coordinates (in latitude and longitude),
θ_f	tidal harmonic argument.

2.3 Effect of inexact value h_2 on radial displacement

To get an idea, how large the effect of an inexact Love number is, we computed the radial displacement at two stations once with the correct Love number $h_2 = 0.6078$ (solid line) and once with the wrong Love number $h_2 = 0.5078$ (dotted line). As follows from figure (F1) the difference of 0.1 in the nominal Love number h_2 causes a displacement error up to 6 cm (station HartRAO, South Africa, at 11:00 UTC on January 1st, 2006).

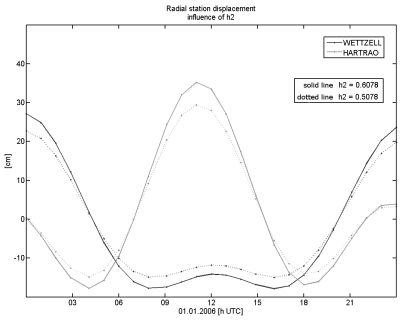

Figure (F1): Effect of wrong degree-2 Love number. By a difference of 0.1 in the nominal value reaches the displacement error in radial direction up to 6 cm.

2.4 Modelled radial components of tidal displacement following the IERS Conventions 2003

Currently, the recommended model in the IERS Conventions 2003 (McCarthy and Petit, 2004) for the computation of the variation of the station coordinates due to the solid Earth tides consists of a two-step procedure. In the first step, corrections are applied in the time domain, with one real nominal value of the Love number for all degree-2 tides ($h_2 = 0.6078$). The out-of-phase displacement due to the imaginary parts of the Love numbers is computed with one value for the diurnal tides ($h_{21}^{I} = -0.0025$) and one value for the semidiurnal tides ($h_{22}^{I} = -0.0022$). In the second step, corrections caused by the intra-band variation of the real degree-2 Love numbers in the diurnal and long-period band are taken into account. The contribution to the displacement from the variation of the imaginary parts of the Love numbers is significant only in the long-period band and from the K_1 tide in the diurnal band, as stated in Mathews et al. (1997).

We decided to compute and visualise the individual contribution to the total tidal displacement in radial direction for the complete Earth's surface with a spatial resolution of 1°x1° on Figures (F2) to (F9). The snap shots are taken for January 1st, 2006 at 0:00 UTC. The configuration of the perturbing bodies is shown in Figure (F10), where the Sun's ephemerides are reduced by a factor of 100. Moon and Sun just passed through their closest position, when they were aligned at new Moon. So, January 1st is the first day after which the amplitude of the tidal displacement reached the maximum and is now slowly decreasing.

In Figures (F2) and (F3) the displacement arising from the second degree tidal potential is divided into the contributions of Moon and Sun, respectively. It can be seen, that the bulges, which are caused by the Moon are slightly more than twice as large as those caused by the Sun. The same separation is shown in (F4) and (F5), where the forming potential is of third degree. In Figure (F5) it can be seen, that concerning degree 3 the contribution of the Sun is quite ignorable. The largest displacement is only 0.01 mm. The out-of-phase contributions to radial displacement are computed with nominal values for the whole band: diurnal (F6) and semidiurnal (F7). In Figure (F8) the correction from 11 constituents in the diurnal band is plotted, showing individual contributions with more than 0.05 mm in amplitude. The variation in frequency arises from the resonance behaviour of the Earth, caused by the presence of the fluid core; its total effect can amount up to ±15 mm. In the long period band (F9) the frequency dependence arises from the mantle anelasticity. Contributions of five terms having a radial correction of more than 0.05 mm in amplitude were considered causing a total displacement of up to ±1 mm. The list with the constituents (including real and imaginary parts) was taken from McCarthy and Petit (2004).

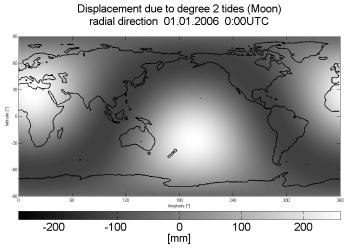

Figure (F2): Displacement in radial direction due to second degree tides on January 1st, 2006 at 0:00 UTC, only Moon's contribution.

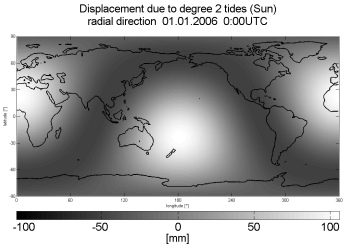

Figure (F3): Displacement in radial direction due to second degree tides on January 1st, 2006 at 0:00 UTC, only Sun's contribution.

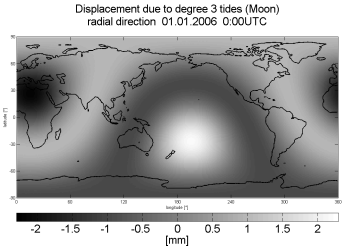

Figure (F4): Displacement in radial direction due to third degree tides on January 1st, 2006 at 0:00 UTC, only Moon's contribution.

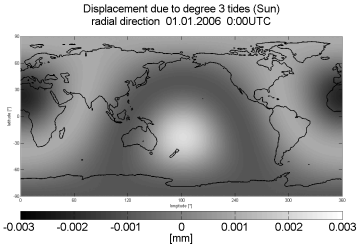

Figure (F5): Displacement in radial direction due to third degree tides on January 1st, 2006 at 0:00 UTC, only Sun's contribution.

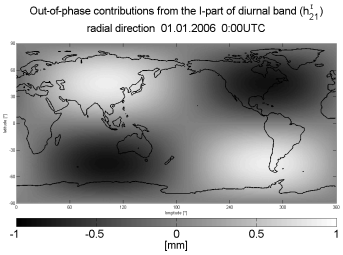

Figure (F6): *tesseral part*
Corrections to displacement in radial direction for the out-of-phase part of diurnal band on January 1st, 2006 at 0:00 UTC.

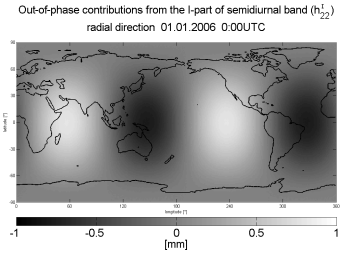

Figure (F7): *sectorial part*
Corrections to displacement in radial direction for the out-of-phase part of semidiurnal band on January 1st, 2006 at 0:00 UTC.

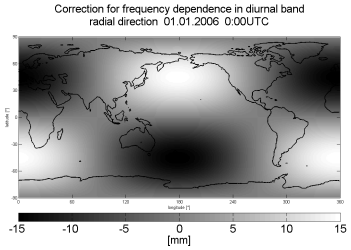

Figure (F8): *tesseral part*
Corrections to displacement in radial direction for frequency dependence in the diurnal band on January 1st, 2006 at 0:00 UTC.

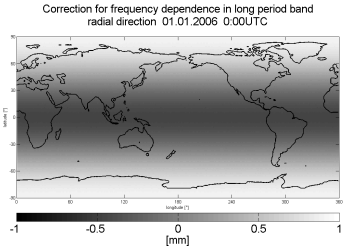

Figure (F9): *zonal part*
Corrections to displacement in radial direction for frequency dependence in the long period band (in-phase and out-of-phase) on January 1st, 2006 at 0:00 UTC.

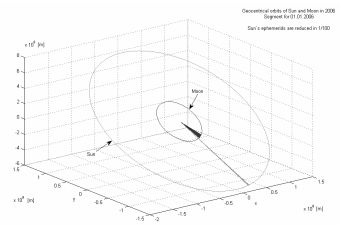

Figure (F10): Geocentric orbits of the Sun and the Moon on January 1st, 2006. Sun's ephemerides are reduced by a factor of 100.

3 Estimation of Love and Shida numbers from VLBI

3.1 VLBI data analysis

The partial derivatives of the tidal displacement w.r.t. the real part of the nominal value of the degree-2 Love and Shida numbers and w.r.t. the real parts of six frequency-dependent Love numbers in the diurnal band have been added to the VLBI software package OCCAM (Titov et al., 2004). We used data from the CONT05 campaign. CONT05 was a two-week campaign of continuous VLBI sessions, scheduled for observing in September 2005 and coordinated by the International VLBI Service for Geodesy and Astrometry (IVS). The observations started on September 12th and ended on September 27th. The station network consisted of 11 stations.

The main settings of the software for the VLBI data analysis were:
- Catalogue of the radio sources: ICRF-Ext.1,
- Catalogue of the stations: ITRF2000,
- Cut-off elevation angle: 5.0°,
- No estimation of source coordinates.

3.2 Results from the CONT05 campaign

a) Nominal degree-2 Love and Shida numbers

Several configurations of the computational approach were applied. Table (T1) shows the mean values of estimated nominal degree-2 Love and Shida numbers for individual (sequential) sessions. The values in the first column refer to the free network solution, where the station coordinates were estimated with an NNR/NNT condition (no net rotation/no net translation). The results obtained from parameter estimation with fixed station coordinates are given in the second column. In both columns, h_2 and l_2 were estimated in parallel. The following two columns refer again to a free network and fixed network, respectively. However, in this case only the Love number h_2 (or only the Shida number l_2) was determined. Figure (F11) shows that the values obtained from the fixed network and from the free solution are shifted by an offset of about 0.02 for the Love number h_2. For the Shida number l_2 (F12) the values are nearly the same. Focusing on the solid and dashed lines it follows, that a simultaneous estimation of the Love and Shida numbers provides almost the same results as a separate estimation of h_2 and l_2.

mean values of estimated nominal degree-2 Love and Shida numbers				
	parallel estimation of h_2 and l_2		separate estimation of h_2 or l_2	
	free network	fixed network	free network	fixed network
h_2	0.6184	0.5899	0.6193	0.5917
standard deviation	±0.0070	±0.0058	±0.0068	±0.0055
l_2	0.0823	0.0824	0.0817	0.0828
standard deviation	±0.0009	±0.0008	±0.0009	±0.0008

Table (T1): Mean values of h_2 and l_2 estimated from the CONT05 campaign.

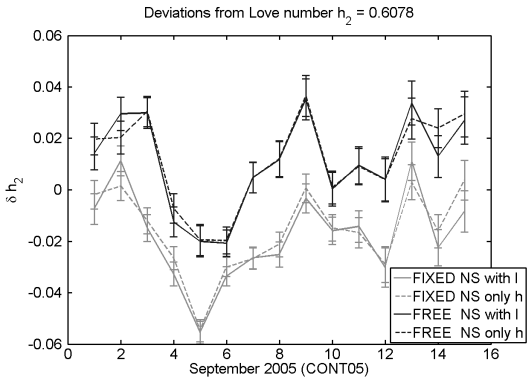

Figure (F11): Deviations from the nominal Love number h_2 estimated for daily intervals during the CONT05 campaign. Grey and black lines show the values obtained from a fixed and free network, respectively. Results from the approach, where the Shida number l_2 was simultaneously estimated are plotted in solid lines, whereas the dotted lines show the separate h_2 estimation.

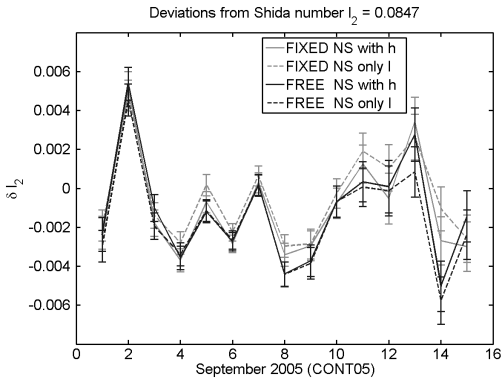

Figure (F12): Deviations from the nominal Shida number l_2 estimated for daily intervals during the CONT05 campaign. Grey and black lines show the values obtained from a fixed and free network, respectively. Results from the approach, where the Love number h_2 was simultaneously estimated are plotted in solid lines, whereas the dotted lines show the separate l_2 estimation.

b) Frequency dependent Love numbers in the diurnal band

We also tried to estimate the Love numbers corresponding to six selected tidal waves in the diurnal band (O_1, P_1, K_1, ψ_1, Φ_1, J_1). The first two digits in the argument number of the tidal wave (Table (T2), second column) represent the group number, which characterizes the block of waves separable from one month of observations. From our period of data (15 days) it

would be only possible to separate the wave O_1 ($n_1n_2 = 14$) from the group $n_1n_2 = 16$, because the cipher n_2 differs by two times of the Moon's mean longitude; the first digit n_1 stays for the species number in the sense of Laplace, where $n_1 = 1$ represents the tesseral spherical harmonic function. To evade this limitation we had to use finesse in the estimation approach. Our strategy was to solve always for one wave only, while the others were kept fixed. This procedure was applied at each tidal wave, so we went six times through the whole data analysis process. Our goal was to find out, if also from a short time interval any reasonable results could be obtained knowing that our procedure is mathematically not fully correct as it neglects all correlations between the parameters of the various terms.

Figure (F13), together with Table (T2), shows the mean estimated value of frequency dependent Love numbers in the diurnal band from the CONT05 campaign (black dots). These are compared to the results achieved by Haas and Schuh (1996) who had used more than 10 years of VLBI data which are plotted in grey lines. The dotted line interpolates between the currently adopted Love number values (McCarthy and Petit, 2004) for the diurnal band. The frequency of the Nearly Diurnal Free Wobble (NDFW) in the terrestrial frame (corresponding to Free Core Nutation (FCN) in the celestial frame) was fixed. It is evident, that the formal errors of the very weak tides, close to the resonance, are larger than those of the strong tides and also larger than of the results obtained by Haas and Schuh (1996) due to the much longer time span of VLBI data used in the latter solution. Nevertheless, it is interesting that a similar shift of $h_{21}(\psi_1)$ is found which was already reported by Haas and Schuh (1996). The point is that the estimated value is opposite to the resonance curve. The "official value" is 1.0569, whereas the results of Haas and Schuh (1996) and this work provide negative values of -0.136 ± 0.228 and –1.484±1.459, respectively. However, it should be paid attention to the large formal errors. Also the weak J_1 tide does not correspond to its expected value. The reason is in the low amplitude and – as already mentioned – the short time span of VLBI data used here. On the other hand, the results for the three strong tides K_1, O_1, P_1 do agree to theory within their formal errors. The differences to their theoretical values are less than twice their standard deviation.

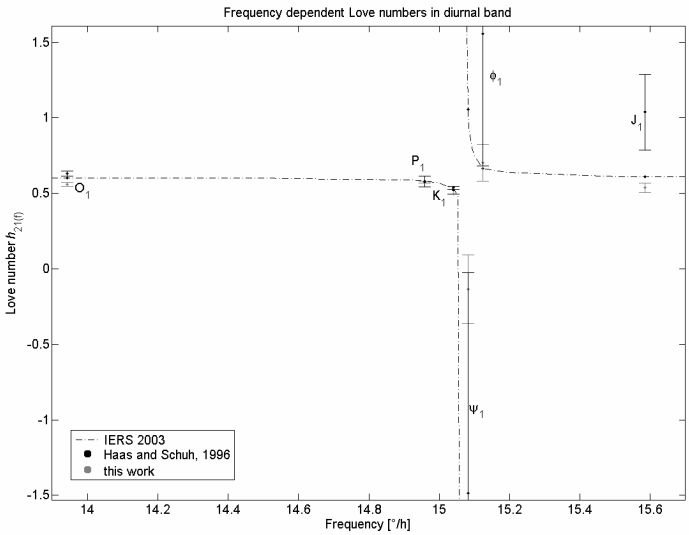

Figure (F13): Estimates of frequency dependent Love numbers in the diurnal band.

Tide	Argument number	Amplitude [mm]	Love number $h_{21(f)}$		
			IERS 2003	Haas and Schuh (1996)	This work
O_1	145.555	–262	0.6028	0.560±0.012	0.631±0.016
P_1	163.555	–122	0.5817	0.574±0.005	0.578±0.036
K_1	165.555	369	0.5236	0.496±0.002	0.537±0.012
ψ_1	166.554	3	1.0569	–0.136±0.228	–1.484±1.459
Φ_1	167.555	5	0.6645	0.702±0.121	1.559±0.879
J_1	175.455	21	0.6108	0.538±0.031	1.039±0.250

Table (T2): Estimates of frequency dependent Love numbers for six tidal waves in the diurnal band.

4 Conclusions

● Nominal second degree Love and Shida numbers of the solid Earth tide model could be already determined from fifteen 24-hour VLBI sessions of the CONT05 campaign.
● The estimated value of the nominal value h_2 is 0.618±0.007, which differs by 0.011 from its theoretical value. The estimate of the Shida number l_2 is 0.082±0.001 and has a difference of about –0.002 from its theoretical value. Better results with respect to the predicted values were found with a free network solution instead of fixed station coordinates.
● One possible reason for the larger uncertainty in the estimates of h_2 compared to l_2 is that it depends on the vertical displacements of the VLBI stations. The vertical component (i.e. height) is usually less precise in space geodetic observations than the horizontal component. It can be subject to errors caused by the time delay of the signals through the atmosphere (errors in the models for the troposphere, e.g. mapping functions) or by atmosphere loading and ocean loading corrections, which are mainly in radial direction.
● Frequency-dependent Love numbers were achieved in an iterative approach for the three largest tidal waves K_1, O_1, P_1, for which the estimated values differ from the theoretical values by less than twice their standard deviation. For the three weak tidal waves J_1, ψ_1, Φ_1, being close to the NDFW resonance, we obtained values with large standard deviations.
● It was demonstrated, that Love numbers for strong tides can be determined from VLBI data covering only a short time interval. The formal errors of the results would decrease with the number of observables used and thus the optimal accuracy could be achieved by doing a so-called global solution using all existing VLBI data since 1984.

5 References

Haas, R., Schuh, H.: *Determination of frequency dependent Love and Shida numbers from VLBI data*. Geophysical Research Letters. Vol. 23 No. 12/1996, pp. 1509-1512.

IERS Conventions (2003). Dennis D., McCarthy and Gérard Petit. (IERS Technical Note; 32) Frankfurt am Main: Verlag des Bundesamts für Kartographie und Geodäsie. 2004. paperback. ISBN 3-89888-884-3 (print version).

Mathews, P.M., Buffett, B.A., Shapiro, I.I.: *Love numbers for a rotating spheroidal Earth: New definition and numerical values*. Geophysical Research Letters. Vol. 22 No. 5/1995, pp. 579-582.

Mathews, P.M., Dehant, V., Gipson, J.M.: *Tidal station displacements*. Journal of Geophysical Research. Vol. 102 No. B9/1997, pp. 20469-20477.

Melchior, P.: *The tides of the Planet Earth*. Pergamon Press. Oxford 1983. Second edition.

Sovers, O.J., Fanselow, J.L., Jacobs, C.S.: *Astrometry & Geodesy with Radio Interferometry: Experiments, Models, Results.* Rev. Mod. Phys.. Vol. 70 No. 4/1998, pp. 1393-1454.

Titov, O., Tesmer, V., Boehm, J.: *OCCAM v. 6.0 software for VLBI data analysis*. IVS 2004 General Meeting Proceedings, edited by Nancy R. Vandenberg and Karen D. Baver, NASA/CP-2004-212255. 2004, pp. 267-271.

Pre, co and post-seismic motion for Altay region by GPS and gravity observations

V.Yu. Timofeev, D.G. Ardyukov, Y.F. Stus, E.N. Kalish*, E.V.Boiko, R.G. Sedusov, A.V. Timofeev, **B. Ducarme*

Trofimuk Institute of Petroleum Geology and Geophysics SB RAS, Novosibirsk, Russia.
**Institute of Automation and Electrometry SB RAS, Novosibirsk, Russia.*
***Royal Observatory of Belgium, Brussels, Belgium*

Abstract

We used GPS method to investigate the preseismic, coseismic and postseismic deformation due to the 27 September 2003, M_w = 7.3 Chuya (Altay) earthquake, which occurred south of Russian Altay mountains in southern Siberia near the Russia-Mongolia-China border. On the basis of GPS data measured during the campaigns of observation covering the period 2000-2007, we determined the magnitude and space distribution of 3D displacement fields for different epochs. Geodynamical GPS network consists of 23 sites and extends over structural elements of Russian Altay and surroundings territory (from 49.5°N to 54.8°N, from 81.2°E to 91.4°E). GPS data have been analyzed by GAMIT-GLOBK. Evidence was available of the existence of preseismic (2000-2003 years), coseismic (2003-2004 years) and postseismic (2004-2007 years) processes in this region. We used absolute gravity observation to check vertical motion at base points. Map of preseismic contemporary rates showed values from 0.5 to 10 mm/y and features in 3D velocity field. Russian Altay preseismic motion is connected with present-day displacement in West China and Mongolia. By analysis of the GPS data for 2003-2004 we got the map of coseismic displacements, reflecting the right-lateral strike-slip process in epicentral zone (130°N÷140°N orientation for rupture line). Coseismic horizontal displacements depend on distance between rupture line and GPS benchmarks position, for example, we obtained values from 350 mm at 15 km to 25 mm at 90 km. Vertical motion was smaller (10 ÷ 40 mm). GPS data for 6 benchmarks in epicenter zone show correlation with 2-D model with parameters - for jump on rupture line – 2 m, for maximal depth – 15 km, for shear strain 4 MPa. 3D modeling of coseismic process allowed us to understand displacement field for vertical motion at the end of earthquake rupture (10 ÷ 40 mm jump). Coseismic deformation on 10^{-6} level extended over the epicentral zone (100 km). Postseismic displacement field (2004-2007 years) showed the right-lateral motion in epicenter zone (3 ÷ 7 mm/y). Postseismic data allowed to develop a postseismic model for Chuya earthquake and to determine lower crust parameters (viscosity 10^{21} Pa·s). Analyses of 2000-2007 data allowed us to separate ongoing seismic motion from tectonic motion for West part of Russian Altay (2 mm/y to NW).

Key words: Pre, co- and post-seimic motion by GPS and absolute gravity, earthquake source parameters, viscosity-elastic model.

1. INTRODUCTION

Until recently crustal dynamics in the Altay-Sayan region could be investigated only by the classical geodetic techniques (transit or repeated leveling surveys) within local sites. Satellite surveys have been used since 2000 as part of international project “Present-day Deformation in the Altay-Sayan Region, Siberia, from GPS Geodesy, Absolute Gravimetry and Structural Analysis: Implications for Intracontinental Deformation Process in Central Asia” (grant 97-30874 from INTAS). The objectives of the project include the estimation of recent crustal movements and motions on faults, velocity and strain measurements, integration with data

acquired in the Tien Shan and Baikal region. It was expected to create a united GPS network from Tien Shan to the Baikal rift through East Kazakhstan and Altay-Sayan regions and to join Chinese GPS networks. Such network will record horizontal velocities over the greatest part of Asia and shed more light on the effect of India-Eurasia collision on current deformation in the southern surroundings of Siberia.

The Russian Altay and Sayan regions constitute the northern boundary of the active deformation zone of Central Asia, together with the Baikal rift zone further east. This major intracontinental tectonic feature is associated with strong seismic activity and surface deformations. The territory of Russian Altay is highly elevated area (up to 4500 m) with strike-slip faults, oblique thrusts, thrusts and normal faults. Analysis of earthquake focal mechanisms and stress tension inversion suggests in Altay-Sayan area two zones with different orientation of main stress axes [Peltzer&Saucier, 1996; Calais et.al., 2000, 2002, 2003]. To the east, in the Sayans, southern Tuva and northern Mongolia, a NNE-directed near horizontal compression dominates. To the west, in Russian Altay, a NNW-directed horizontal compression dominates. Last strong Chuya earthquake (27/09/2003, 49,999°N, 87,852°E, Mw = 7.3 ÷ 7.5) happened on Russian Altay territory where GPS network observations had been performed previously. Chuya (Altay) earthquake was the largest event striking the Russian Altay mountains in the last centuries. The objective of our study is to estimate pre-seismic, co-seismic and post-seismic velocity fields in the Chuya earthquake zone and in surroundings territory using GPS method. Choice of co- and post-seismic process models is the second task of our investigation. Third task is the estimation of tectonic part in Russian Altay velocity field (2000-2007 yy.).

2. ONGOING CRUSTAL MOVEMENTS IN RUSSIAN ALTAY (2000-2007 yy.)

We started GPS measurement in Russian Altay region, an area extending from 49°N till 55°N and from 80°E till 90°E, in 2000 (Fig, 1). Geodynamical GPS network consists of 25 sites where we use 3 GPS receivers Trimble 4700 simultaneously and 1 receiver Trimble 4700 at the permanent station NVSK not far from Novosibirsk. Most of the benchmarks are situated on bed rock. It should be noted that the deposits included permanent frosted ground in Chuya and Kurai depressions. Observations were always performed during the month of July to eliminate the seasonal influence [Timofeev et al., 2003, 2006]. This network results together with observations in surrounding territories were presented in our 97-30874/INTAS report [Calais at al, 2002, 2003]. We measured NNE displacements in Western China. East-direction motion for Center Mongolia and NW displacements for Eastern Kazakhastan. GPS measurements during four campaigns on the Altay network (2000-2003 yy.) were processed using Eurasian reference frame data (relative to 30 permanent stations) by the GAMIT-GLOBK software [Boucher et al., 2001]. The solution showed motion with respect to stable stations (NVSK, ELTS, KRUT) situated in a non deformed flat territory located at the north of Gorny Altay (Fig. 2). For this period the error was near 0.6 ÷1.0 mm for horizontal velocity and near 2.5 mm for vertical velocity. Most of the measured horizontal velocities were ranging from 0.2 to 4.0 mm/y and reach 5 ÷ 10 mm/y only for points in the extreme south. Note that the last measurement cycle ended in August 2003 just before the Chuya earthquake (M = 7.3, 27/09/2003) which struck the southern part of the studied territory [Goldin et al, 2003]. The fault plane solution for the Chuya earthquake indicated NS compression and EW extension. Vertical velocities before earthquake reflect this effect. We investigated the behavior of the north component of horizontal velocity along the S-N profile from the Lhasa station (LHAS, Tibet) to Novosibirsk (NVSK), through Urumchi (URUM, Western China), and epicenter area , i.e. along the direction orthogonal to the zone of active deformation in Asia. The velocities include northward component which changes linearly from 20÷22 mm/y at 29.6°N to 0÷2 mm/y at 55°N (Fig. 3). Velocities abruptly decrease after the UKOK benchmark (Ukok plateau, heights from 2500 m to 4000 m), i.e. in front of the future epicentral area. The preseismic NS velocities had been analyzed and have provided the deficit of

~ 5 mm/y at epicentral zone [this deficit noted too in Nissen et al, 2007]. The previous large earthquake in the Altay-Sayan region occurred about 250 years ago in this area. It was a M = 7.7 earthquake on 09/12/1761 at 50.0°N; 90.0°E [New catalogue, 1977] . Thus in the frame of linear model, the accumulated deficit of northward displacement is about 1,25 m or about 2 m in the nodal plane (2003, Chuya earthquake), which approximately corresponds to the seismic moment of 10^{20} N·m [http://neic.usgs.gov/neis/FM/neic-zfak-g.html]

The preseismic velocity field was studied and the existence of two dominant directions of motion (NW block and NE block) was shown in the studied territory (Fig. 2). The turn point for the NW and NE components was situated near Chuya earthquake epicenter. In the south the NE direction of motion agrees with GPS data for northwestern Mongolia (5-6 mm/y) and China (URUM, Urumchi, 11 mm/y). For deformation we can mention the NW extension of $5 \cdot 10^{-8}$ along the line of CHAG-KURA-ULAG-CHIK-SEMI-USTK and the NE compression up to $2 \cdot 10^{-7}$ along the line UKOK-CHAG-YAZU.

GPS measurements after the Chuya event started in the spring of 2004, just after melting ice-snow cover. In May we carried out measurements at two sites (KURA, CHAG) located in the epicentral area (Fig. 4) and one site (ARTB) at 300 km to north of the main shock. In July 2004 we observed Altay network (Fig. 5). Processed data from sites within 100 km of the main shock showed the greatest coseismic deformation in the epicentral area. Continued seismic process had produced the noise. The difference between the May and July results represents the afterslip delay (Fig. 4):5 mm in a 2.5 month period. The co-seismic jump indicated a right-lateral slip along the earthquake rupture. Our benchmarks are located from 15 km to 90 km mainly on NW flank of Chuya earthquake. The horizontal displacement depends on the distance from the nodal plane: it decreased from 0.35 m at 15 km to 0.02 m at 90 km away from the rupture. The rupture line orientation was obtained by KURA result (155° N) and by CHAG result (125° N) and the average value determined through KURA-CHAG GPS result is 140° N ± 15° is similar to seismological data [Nissen et al, 2008, http://neic.usgs.gov/neis/FM/neic-zfak-g.html, Starovoit et al., 2003]. Vertical jump reached its maximum (0.03÷0.05 m) near the fault (15÷35 km distance from earthquake rupture). These results correspond to the sum of seismic effects accumulated during one-year period (from July 2003 to July 2004). Horizontal component predominate over vertical displacements for co-seismic motion. Analysis of the May-July-2004 data have shown that most of elastic effect took place during the first months after Chuya earthquake. The first-order effects, which correspond to a right-lateral strike slip, can be interpreted in the frame of the elastic rebound model. The applicability of the elastic rebound model is supported by the evidence of NW motion before the event (Fig 2, 5).

Postseismic velocity field was obtained for epicentral area during the 2004-2007-period (Fig. 5, Table 1). Postseismic motion presented the same sign as coseismic effect with smaller rate. Average velocity for epicenter area is 4÷5 mm/y (CHIB, AKTA, ULAG, KURA, CHAG) at distances ranging from 15 km to 50 km, average distance 35÷40 km.

Absolute gravity observation at NVSK, USTK and KAYT station were used to check vertical displacements for Altay network. Absolute gravity data were processed with corrections (tidal, polar motion, air pressure and other) recommended by International Center [Stus et al., 1995]. Results for Altay station USTK located on bed rock is presented on Fig. 6. Gravity value was stable in the range of standard error (2 microgal). This stable station was used as base point.

Some reports [Nissen et al., 2007, Barbot et al., 2008] presented SAR result for Chuya earthquake quoting 1 m vertical displacement near fault rupture line. This effect may be connected with landslip activity at Chuya-Kurai ranges side of rupture zone [Starovoit et al., 2003] and partly with lifting of permanent frozen ground at Chuya-Kurai depressions side. Weather anomaly was observed during the summer before Chuya earthquake and during the next winter. Usually Chuya-Kurai depressions and surrounding territory has very dry summer and winter condition like desert, but 2003-summer and 2003/2004 winter had rainy weather condition.

Processing of Russian Altay network data for 2000-2007 yy. period without the epicenter area results are shown on Fig. 2. This analyses allowed us separate seismic motion and tectonic part for West part of Russian Altay (2 mm/y to NW). This motion may be only a part of Russian Altay compression (5 ÷ 7 mm/y), other part may be included in the NE and East motion of Sayan-Tuva region situated at the East of Russian Altay.

3. MODEL OF COSEISMIC PROCESS AND CHUYA EARTHQUAKE SOURCE PARAMETERS

Current GPS velocities show for Russian Altay a shortening at 5÷7 mm/y level. Lying around 2500 km north from the Himalaya, the Russian Altay mountains comprise the most distant region of active continental shortening at 35÷45 mm/y level in the India-Eurasia collision zone. Most authors regard the Asian earthquakes process as the result of this effect. At a tectonic scale shortening would be realized partly by means of earthquake effect.

For strike-slip earthquake process the elastic rebound model appeared already one century ago [Reid, 1911; Stacey, 1969]. In a strictly elastic earth, complete elastic rebound would take place in a few seconds the only slow deformation would be the accumulation of tectonic strain. But single series GPS or SAR observations separated of some months period, and seismic process would study as a sum of main shocks, aftershocks and afterslip effect (Fig. 4). Our GPS network have not such a data density as SAR method, its benchmarks are situated far from earthquake rupture, but cover a more extensive territory.

We discussed this process for Chuya earthquake in frame of elastic theory at half space [Nur&Mavko, 1974; Savage&Burford, 1993; Segall, 2002; Turcott&Schubert, 1982]. Coseismic deformation can be explained by simple models based on solutions in an elastic half-space. When we have strike-slip events along subvertical rupture, with a length ($\boldsymbol{L}$) much larger than the depth ($\boldsymbol{a}$) or $\boldsymbol{L} >> \boldsymbol{a}$, we can use 2D model (infinite length).

For Screw Dislocation Model (SDM, single source, Figure 7) the horizontal displacement $\Delta\omega_z$ along axis X on the surface can be written as

$$\Delta\omega_z = (\Delta\omega/2) \cdot [1 - (2/\pi) \operatorname{arctg} (x/a)]. \quad (1)$$

where $\Delta\omega$ is the slip in the fault plane.

In the next 2-D Model (2DM, source is infinite belt, Figure 8) we have strike-slip motion along the vertical infinite fault (along axis Z) at depth $\boldsymbol{a}$ (axis Y). For half-space (y>0) we have equilibrium equation for force along axis Z:

$$\partial\sigma_{xz}/\partial x + \partial\sigma_{yz}/\partial y = 0,$$

or for motion ω_z we have Laplace equation:

$$\partial^2\omega_z/\partial^2 x + \partial^2\omega_z/\partial^2 y = 0. \quad (2)$$

At the surface we have a distribution of the displacement along axis X depending from two parameters – depth ($\boldsymbol{a}$) and slip along the crack ($\Delta\omega = (\sigma_{xz,0}/G)\cdot 2\boldsymbol{a}$) :

$$\Delta\omega_z = \pm\Delta\omega \cdot [(1 + x^2/a^2)^{1/2} - |x|/a] / 2. \quad (3)$$

The effects for these models (SDM and 2DM) are quite similar (Fig. 9). Two parameters (the slip - $\boldsymbol{\Delta\omega}$ and the depth – $\boldsymbol{a}$) control displacement distribution. If we take GPS results for coseismic jumps at different distances from main shock (27/09/2003), earthquake source parameters ($\boldsymbol{\Delta\omega}$ and $\boldsymbol{a}$) can be computed by SDM and 2DM. Using results for CHAG and YAZU points we received $\boldsymbol{\Delta\omega}$ = 1.7 m, $\boldsymbol{a}$ = 8.6 km (SDM) and $\boldsymbol{\Delta\omega}$ = 1.9 m, $\boldsymbol{a}$ = 10.0 km (2DM). Second solution is more correct for our annual GPS observation as it include aseismic creep and afterslip effect. These results are in good agreement with seismological results. Similar displacement curve for Chuya earthquake coseismic displacements across fault was obtained by InSAR method [E.Nissen at al., 2007]. It is known that the seismological estimations of Chuya earthquake coordinates differ up to 10÷20 km due to unknown crust parameters for this region.

At next steps of analyses we used 130°N orientation of subvertical nodal plane, which crossed the main shock point with coordinates (49,999°N, 87,852°E), for parallel displacement

calculation. The results for 2D model and experimental results are shown at Figure 10. Using experimental GPS data for center of zone (CHAG and KURA) and theoretical distribution (2DM, (2)) we can determine parameters $\boldsymbol{a}$ and $\boldsymbol{\Delta\omega}$. In this case we have: $\boldsymbol{a}$ = 16.5 km and $\boldsymbol{\Delta\omega}$ = 1.8 m. The same value for slip was received by seismological study (2 m) and by geomorphology data (0.5 ÷ 5.0 m).

For elastic modulus G values ranging from 30 GPa to 55 GPa, depth from 9 km to 16 km and displacement 2 m we have estimated the shear stress range - from 2 MPa to 6 MPa, and the average - 4 MPa.

This method (2DM) was tested successfully for Western Kunlunshan Pass region where strong earthquake (M = 8.1) with left-lateral slip (5 ÷ 7 m) happened on 14.11.2001 [X. Shan, 2004]. In this case mean value for depth agree with seismological data too.

For Chuya earthquake using slip value ($\Delta\omega$ = 2 m) we tested the depth value in different part of epicenter zone (figure 10) and estimated the length of the fault (140 km). Depth reduced from 15 km (at the center) up to 0 km at the ends of nodal plane. Using this model the frames of shift deformation were calculated (Figure 9). Co-seismic deformation for triangles: UKOK-CHIK-KAIT; CHAG-KURA-YAZU; KURA-BALY-YAZU; ULAG-KURA-BALY, was estimated by GPS results (Figure 11). Coseismic deformation on 10^{-6} level extends over epicentral area (near 100 km from the main shock epicenter).

For study of 3D coseismic jump and for vertical displacement especially at the ends of the rupture we used 3-D model [Okada, 1985]: vertical finite shear fault with constant slip (2 m), spatial depth's distribution and 140 km length of fault at the surface. This solution is surface integration of single source (see formula (1)) Calculation are carried out with normal Poisson's ratio (ν = 0.25). Fault model consists of three planes, the origin (0, 0) being at the epicenter of main shock (27/09/2003):

1. for 0 < a < 5 km, L = 130 km, from -57 km to +73 km;
2. for 5 < a < 10 km, L = 97 km, from -46 km to +51 km;
3. for 10 < a < 15 km, L = 42 km, from -20 km to +22 km.

The results correspond to our experimental data, for example, station UKOK:
model (x, y, **z**) 246.9 mm, 96.2 mm and **25.6 mm** (265 mm vector)
and the experiment (x, y, **z**) 204.0 mm, 192.5 mm and **28.7 mm** (280 mm vector)).
Differences are connected with the nodal plane location at the end of the rupture and the non vertical position of nodal plane at the end of earthquake rupture.

Using the above mentioned 3-planes model (slip 2m and G = $3.3 \cdot 10^{10}$ Pa), earthquake source parameters were determined: seismic moment $M_0 = 0.9 \cdot 10^{20}$ N·m, earthquake magnitude $M_w = 7.2$ ($M_w = \frac{1}{2}(\log M_0 - 5.5)$).

We can compare earthquake magnitude and rupture length by empirical scaling relationships between magnitude and surface rupture length. Authors [Johnson&Segall, 2004] suggest magnitude, M_w, and rupture length, L, are related as

$$M_w = 1.1 \cdot \log (L) + 5.0 \qquad (4)$$

Using this relationship, Chuya earthquake with a rupture length in the range 75 ÷ 140 km would have a magnitude in a range M_w = 7.0 ÷ 7.4.

4. POSTSEISMIC DISPLACEMENT (2004 - 2007 yy.) AND VISCOELASTIC MODELS

We used GPS network to study the postseismic transients. The postseismic displacement field (2004-2007, Table 1) has the same sign as the coseismic one (Figure 5). The observed postseismic signal extends from epicenter zone, with wavelengths much larger than locking depth (8 ÷ 16 km), but of the order of the fault length (80 ÷ 150 km). As noted by [Barbot et al, 2008] the polarity of the postseismic displacement around the fault does not warrant the poroelastic rebound in the upper crust, suggesting a very low permeability or fluid saturation of the crustal rocks in the Chuya&Kurai depressions and Chuya Range. Concerning the possibility

of a rapid pore fluid flow within the first seven months following the earthquake, we have no constraints from our GPS data. We cannot rule out the afterslip process during the first year following the earthquake as it was discussed [Barbot et al, 2008]. This effect can be present at May-July 2004 result (Figure 4).

The screw dislocation or 2DM provides only a very limited description of plate-boundary faulting. A somewhat more realistic model involves an elastic layer of thickness H overlying a Maxwell viscoelastic half-space [Segall, 2002]. The Maxwell material has relaxation time $\tau_R = 2\eta/\mu$, where η is the viscosity and μ is the shear modulus. At time t = 0 slip Δu occurs on the fault from the surface to depth $D \leq H$. The velocity on the Earth's surface as a function of position perpendicular to the faults, x, number of seismic activity process, n, and time, t, is

$$v(x, t) = (\Delta u/\pi\cdot\tau_R)\cdot \exp(-t/\tau_R) \sum_{n=1}^{\infty}[(t/\tau_R)^{n-1}/(n-1)!]\cdot F_n(x, D, H), \qquad (5)$$

where the spatial distribution is given by

$$F_n(x, D, H) = [\tan^{-1}(D+2nH/x) + \tan^{-1}(D-2nH/x)] = \tan^{-1}[2xD/x^2+ (2nH)^2- D^2],$$

if n =1

$$v(x, t) = (\Delta u/\pi\cdot\tau_R)\cdot \exp(-t/\tau_R) \tan^{-1}[2xD/x^2+ (2nH)^2- D^2]. \qquad (6)$$

The post-seismic velocity is a function of the coseismic slip Δu, the depth of faulting D, the elastic layer thickness H, the material relaxation τ_R and the time since the last large earthquake t.

The temporal dependence depends only on the dimensionless ration t/τ_R and relaxation time τ_R (see Fig. 12, $(\Delta u/\pi\cdot\tau_R)\cdot \exp(-t/\tau_R)$). The spatial distribution is given by a function of position perpendicular to the faults, x, the depth of faulting D, and the elastic layer thickness H (see Fig. 13, $\tan^{-1}[2xD/x^2+ (2nH)^2- D^2]$). From parameters presented at Table 1 (3-4 mm/y for epicenter zone), at Fig. 12 and 13 we can estimate Maxwell time $\tau_R \geq 100$ years.

A model of viscoelastic relaxation is convenient to describe postseismic effect of Chuya earthquake. In order to determine the characteristics of time-dependent deformation which follows the sudden slip on large earthquake faults, one considers two-layers in the crust, an elastic layer H overlying a viscoelastic layer h (Elsasser model, Figure 14). Assuming that at time t = 0 sufficient tectonic stress has accumulated to cause sudden faulting, the solution to the elastic-viscoelastic model was obtained in two steps: first the static displacements were solved and stresses due to a fault in an elastic layer welded to an viscoelastic layer. But, as time goes on, the deformation changes as a result of the relaxation in lower viscoelastic layer, formal effect is like an earthquake source drop. Important parameters for viscoelastic model are stress jump, earthquake depth, thickness of elastic layer and viscoelastic layer, elastic modulus and viscoelastic modulus, rate of deformation or motion, elapsed time since the event, velocity at surface at different distances from the epicenter and nodal line. Usually two-layers model is used. As shown in the papers [Barbot, 2008; Wang et al., 2003] three-layers model with weak mantle does not change results insignificantly. Two layers model used following parameters: elastic layer (thickness H), viscous layer (thickness h) and the fault along axis Z; right-lateral postseismic velocity ($\partial\omega_{zE}/\partial t$), stress jump σ_{xz}. We consider in the two-layers model a 20 km elastic upper crust and a 25 km viscoelastic lower crust [Elsasser, 1971, Calais et,al, 2002]. Preliminary result for post-seismic average velocity observed at distance range 15÷50 km was estimated as 5 mm/y, the stress jump for Chuya earthquake was estimated as 4 MPa, elastic modulus for crust G = 33÷55 GPa. For the viscosity of lower crust we have:

$$\eta = \sigma_{xz}\cdot h / (\partial\omega_{zE}/\partial t) = 5\div 8\cdot 10^{20}\ \text{Pa}\cdot\text{s}, \qquad (7)$$

Relaxation time for Russian Altay (Elsasser time $\tau = \eta/2G$) was estimated as 200÷300 years. Elsasser time and Maxwell time connect by equation [Elsasser, 1969]:

$$\tau_M = [\pi^2 \cdot H/(16h)] \cdot \tau_E, \quad (8)$$

for our parameters (H =20 km and h = 25 km) we have $\tau_M = 0.49 \cdot \tau_E$.

These parameters corresponded to two-layers model with the largest wavelength of the deformation [Barbot et al, 2008].

5. CONCLUSIONS

GPS observations show NW motion in Western part of Russian Altay (2 mm/y), as a part of NNE convergence (7 mm/y) is accommodated across the Russian Altay mountains. Present-day velocity field is deformed in its south-east part by Chuya earthquake process. Features in velocity field before Chuya earthquake were obtained by GPS networks. Future epicenter was located at the junction between NW group and NE group of motion. Anomalous horizontal velocities were measured in southern part of Russian Altay at 3÷10 mm/y level. Vertical velocities have shown an increase to the north of the epicenter and a decrease to the south of the epicenter. In the frame of linear tectonics we had accumulation of horizontal displacement before Chuya earthquake (2 meters). Coseismic displacements reflected the right-lateral jump in epicenter zone with determined rupture orientation 140° N ± 15°. Coseismic displacement depended from the distance between nodal plane and GPS benchmarks (from 350 mm (at 15 km) to 25 mm (at 90 km)). 2-D model for surface displacements have been used to describe these phenomena. Using experimental data and modeling, we have estimated parameters of earthquake source: for slip – 2 m, for maximal depth – 15 km, for rupture length – 140 km, for shear stress - 4 MPa, for seismic moment - $0.9 \cdot 10^{20}$ N·m and for magnitude M = 7.2. Preliminary results for post-seismic process show a right-lateral motion with velocity near 4 mm/y. Using two layers model (brittle-elastic upper crust and viscoelastic lower crust) the estimation for effective lower crust viscosity is: $8 \cdot 10^{20}$ Pa·s. Relaxation time in this case was estimated as 300 years.

References

Barbot S., Hamiel Y., Fialko Y., 2008, Space geodetic investigation of the coseismic and posrseismic deformation due to the 2003 M_w 7.2 Altay earthquake: Implications for the local lithospheric rheology. // Journal of Geophysical Research, v.113, B03403, doi: 10,1029/2007JB005063.

Boucher C., Altamimi Z., Sillard P., Feissel-Vernier M.. (2001) The ITRF 2000. // IERS Technical Note, 2001, No.31., 270 p..

Calais E., Amarjargal S., 2000, New constraints on current deformation in Asia from continuous GPS measurements at Ulan Baatar, Mongolia. // Geoph. Res. Letters, v. 27, No. 10, 1527-1530.

Calais E., Vergnolle M., Deverchere J., 2002, Are post-seismic effects of the M 8.4 Bolnay earthquake (1905 July 23) still influencing GPS velocities in the Mongolia-Baikal area? // Geophys. J. Int., 149, 157-168.

Calais E., Vergnolle M., San'kov V., Lukhnev A., Miroshnichenko A., Amarjargal S., Deverchere J., 2003, GPS measurements of crustal deformation in the Baikal-Mongolia area (1994-2002): Implications for current kinematics of Asia. // J. Geophys. Res., 108 (B10), 2501, doi: 10,1029/2002JB002373.

Elsasser W.H., Convection and stress propagation in the upper mantle. // "The Application of Modern Physics to the Earth and Planetary Interior, ed. Runcorn, S.K., Wiley, New York, 1969, 223-246.

Elsasser W.H., Two-Layer Model of Upper-Mantle Circulation. // J. Geophys. Res., 1971, v.74, n.20, p.4744-4753.

Fialko Y., 2004, Evidence of fluid-filled upper crust from observations of postseismic deformation due the 1992 M_w 7.3 Landers earthquake. // Jour.Geophys.Res., v.109, B08401, doi.:10.1029/2004JB002985.

Freed A.M., Burgmann R., Calais E., Freymueller J., Hreinsdottir S., 2006. Implications of deformation following the 2002 Denali, Alaska, earthquake for postseismic relaxation processes and lithopheric rheology. // Jour.Geophys.Res., v. 111, B01401, doi.:10.1029/2005JB003894.

Goldin S.V., Timofeev V.Y., Ardyukov D.G. Fields of the earth's surface displacement in the Chuya earthquake zone in Gornyi Altay. // Doklady Earth Sciences, vol.405A, No.9, 2005, 1408-1413.

Johnson K.M., Segall P., 2004,Viscoelastic earthquake cycle models with deep stress-driven creep along the San Andreas fault system. // Journal of Geophysical Research, v,109, B10403, doi: 10,1029/2004JB003096.

Nissen E., Emmerson B., Funning G. J., Mistrukov A., Parsons B., Robinson D.P., Rogozhin E., Wright T.J., 2007, Combining InSAR and seismology to study the 2003 Siberian Altay earthquakes – dextral strike-slip and anticlockwise rotations in the northern India-Earasia collision zone. // Geophys, J, Int, , 169, 216-232, doi: 10,1111/j, 1365-246X, 2006,03286,x.

Nur A., Mavko G., 1974, Postseismic Viscoelastic Rebound. // Science, v. 183, n. 4121, 204 – 206.

New catalogue of historic strong earthquakes for the USSR territory, from oldest time to 1975. (in Russian) 1977, Nauka, Moscow, 297-314.

Okada Y., 1985. Surface deformation due to shear and tensile faults in a half-space. // Bull. Seismol. Soc. Am., 75, 1135-1154.

Peltzer G., Saucier F. (1996) Present-day kinematics of Asia derived from geologic fault rates. // J.Geophys.Res., December 10, 1996, v.101, B12, pp.27,943-27,956.

Reid H. F. (1911) The elastic rebound theory of earthquakes. // Bull. Dept. Geology. Univ. California, 1911, 6, 413 p..

Savage J.C., Burford R.O., 1973, Geodetic Determination of Relative Plate Motion in Central California. // Journal of Geophysical Research, v. 78, No. 5, pp. 832-835.

Savage J.C., Prescott W. H., 1978, Asthenosphere Readjustment and the Earthquake Cycle. // Journal of Geophysical Research, v, 83, No, B7, 3369-3376.

Segall P., 2002, Integrating Geologic and geodetic Estimates of Slip Rate on the San Andreas Fault System. // International Geology Review, v, 44, p, 62-82.

Stacey F.D., Physics of the Earth, 1969, J.W.&S.I., New York, London, Sydney, Toronto, 342 p..

Starovoit O.E., L.S.Chepkunas, I.P.Gabsatarova, 2003,The parameters of earthquake 27/09/2003 at Altay by instrumental data. (In Russian). // Electronic Journal of Science and Information magazine, "Vestnik otdelenia nayk o Zemle RAN"(Bull. RAS, Earth Sci.), n.21.

Stus Y.F., Arnautov G.P., Kalish E.N., Timofeev V.Y., 1995, Non-tidal Gravity variation and Geodynamic Processes. // "Gravity and Geoid", Shpringer, Germany, p.35-43.

Timofeev V. Yu., Ardyukov D.G., Duchlov A.D., Zapreeve E.A., Calais E., 2003, Modern geodynamics of western Altay-Sayan region, from GPS data. // Russian Geology and Geophysics, 44, 1168-1175.

Timofeev, V, Yu,, Ardyukov D,G,, Calais E,, Duchlov A,D,, Zapreeve E,A,, Kazantsev S,A,, Roosbeek F,, Bruyninx, 2006, Displacement fields and models of current motion in Russian Altay. // Russian Geology and Geophysics, 47, n.8, 923-937.

Timofeev, V, Yu, Gornov P.Y., Ardyukov D,G, Malishev Yu.F., Boyko E.V. Results of analysis GPS data (2003-2006 yy.) at Sikhote-Alin net, Far East. // Geology of the Pacific Ocean, v.27, n.4, 2008, p. 39-49 (ISSN 0207-4028).

Turcott D.L., Schubert G., 1982, Geodynamics. Applications of Continuum Physics to Geological Problems. John Willy & Sons. 2 v., New York, Chichester, Brisbane, Toronto, Singapore, 730 p.

Wang R., Martin F.L., Roth F., 2003, Computation of deformation induced by earthquakes in a multi-layered elastic crust-FORTRAN programs EDGRN/EDCMP. / Computers&Geosciences, 29, 195-2007.

Xinjian Shan, Jiahang Liu, Chao Ma, 2004, Preliminary Analysis on Characteristics of Coseismic Deformation Associated with M=8.1 Western Kunlunshan Pass Earthquake in 2001. // Proceedings of the APSG Symposium. Space geodesy and its applications to Earth Sciences, Shanghai Astronomical Observatory, CAS, p.91-98.

Table 1. Velocities for Altay network (2004-2007 yy.) calculated relative Eurasia plate model AR-IR2006 [Timofeev et.al., 2008]. Epicenter zone – red. West part of Gornii Altay – green

Code of point	Latitude φ	Longitude λ	Height, m, WGS84	AR-IR 2006, Vφ	AR-IR 2006, Vλ	Exper. Vφ	Exper. Vλ	Difference Vφ	Difference Vλ
UKOK	49,562° N	88,232° E	2323.9	-3.64	26.26	-2.0±0.8	24.6±0.7	+1.6±0.8	-1.6±0.7
KURA	50,245° N	87,890° E	1490.3	-3.54	26.22	-6.8±0.5	30.0±0.6	-3.2±0.5	3.8±0.6
CHAG	50,068° N	88,417° E	1710.6	-3.69	26.21	-7.9±0.4	30.0±0.5	-4.2±0.4	3.8±0.5
AKTA	50,325° N	87,619° E	1365.5	-3.50	26.20	-7.8±1.3	30.1±1.1	-4.2±1.3	3.9±1.1
CHIB	50,313° N	87,503° E	1122.8	-3.43	26.23	-7.7±0.8	27.0±0.9	-4.2±0.8	0.8±0.9
								-3.9	**+3.1**
YAZU	50,586° N	88,851° E	1542.8	-3.82	26.14	-10.2±1.2	34.6±1.3	-6.3±1.2	8.4±1.3
ART2	51,799° N	87,282° E	460.8	-3.36	26.09	-3.6±0.5	26.8±0.5	-0.2±0.5	0.7±0.5
CHIK	50,644° N	86,313° E	1249.5	-3.08	26.25	-0.9±0.3	23.3±0.3	+2.1±0.3	-3.0±0.3
USTK	50,939° N	84,769° E	999.4	-2.63	26.28	-2.3±0.3	24.3±0.3	+0.3±0.3	-2.0±0.3
KAYT	50,146° N	85,439° E	1037.5	-2.83	26.33	0.7±0.3	23.4±0.4	+3.5±0.3	-2.9±0.4
								+1.9	**-2.6**

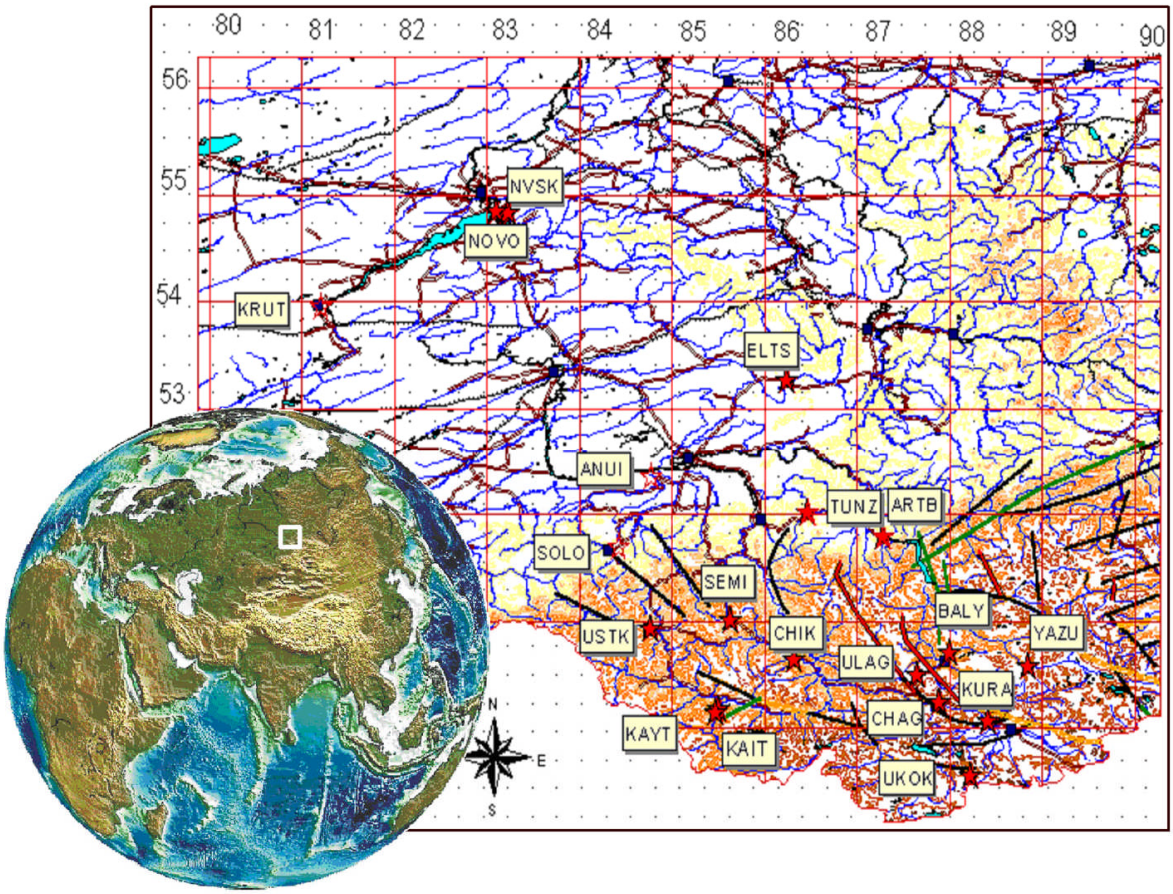

Figure 1: GPS stations in Gorny Altay and reference stations to the North

Pre-seismic situation and tectonic part

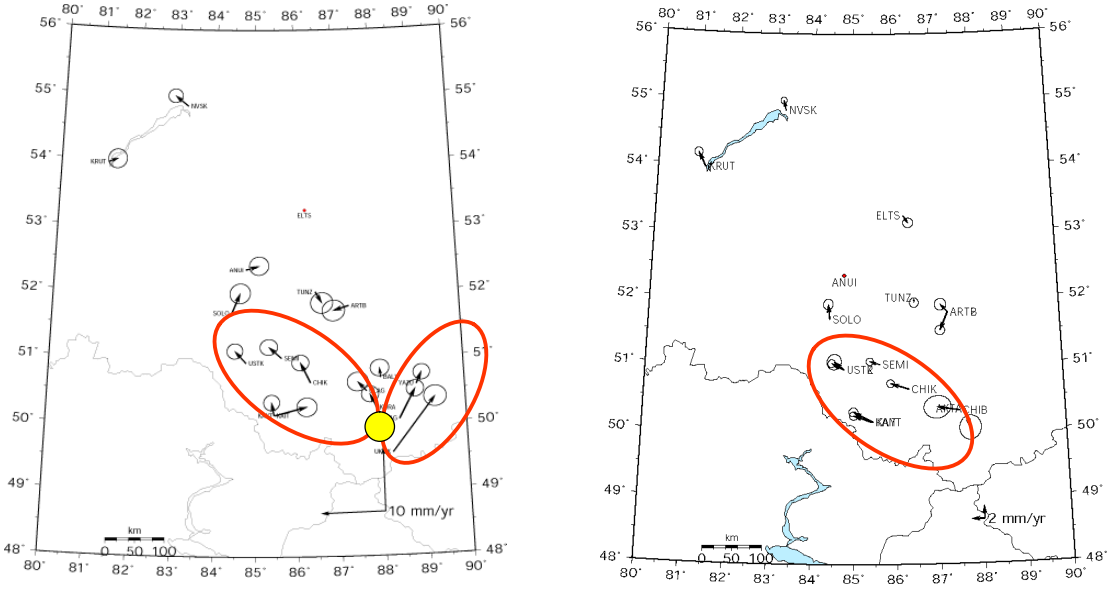

2000-2003 **2000-2007**

Figure 2: Pre-seismic situation (2000-2003) and long term tectonic part (2000-2007)

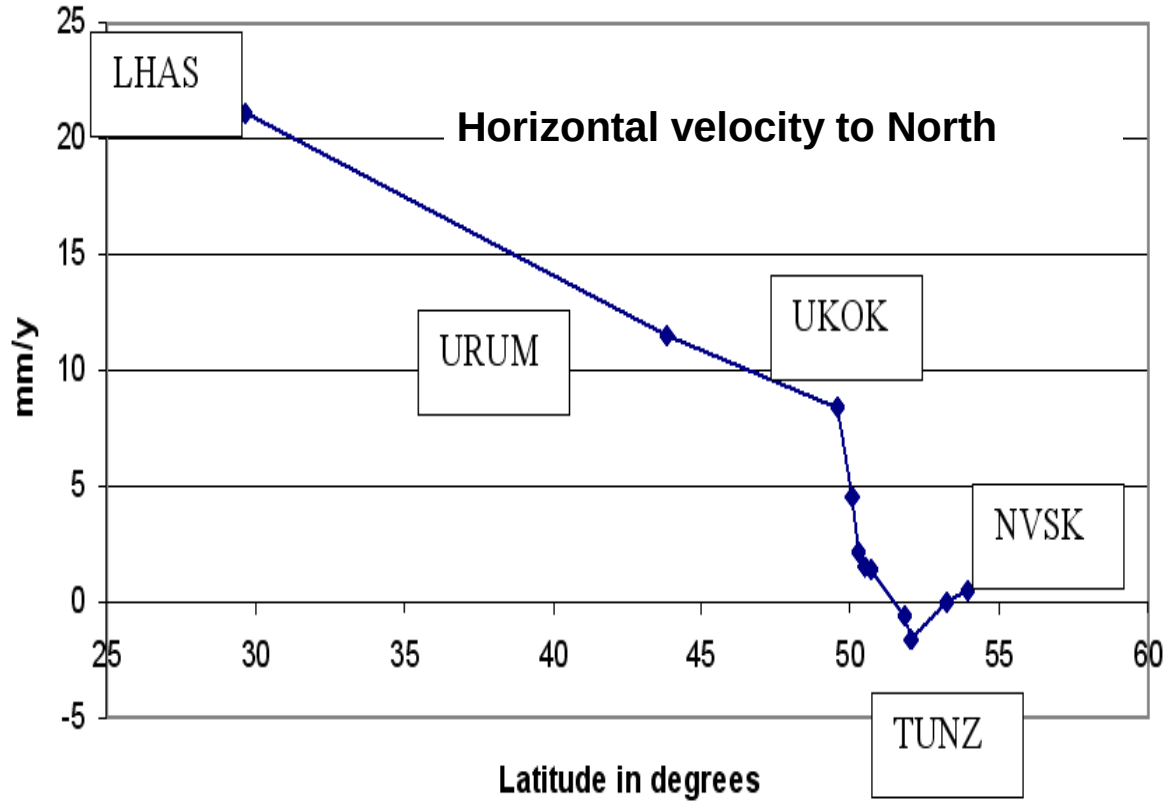

Figure 3: Horizontal velocities along a SN profile Lhasa-Novosibirsk

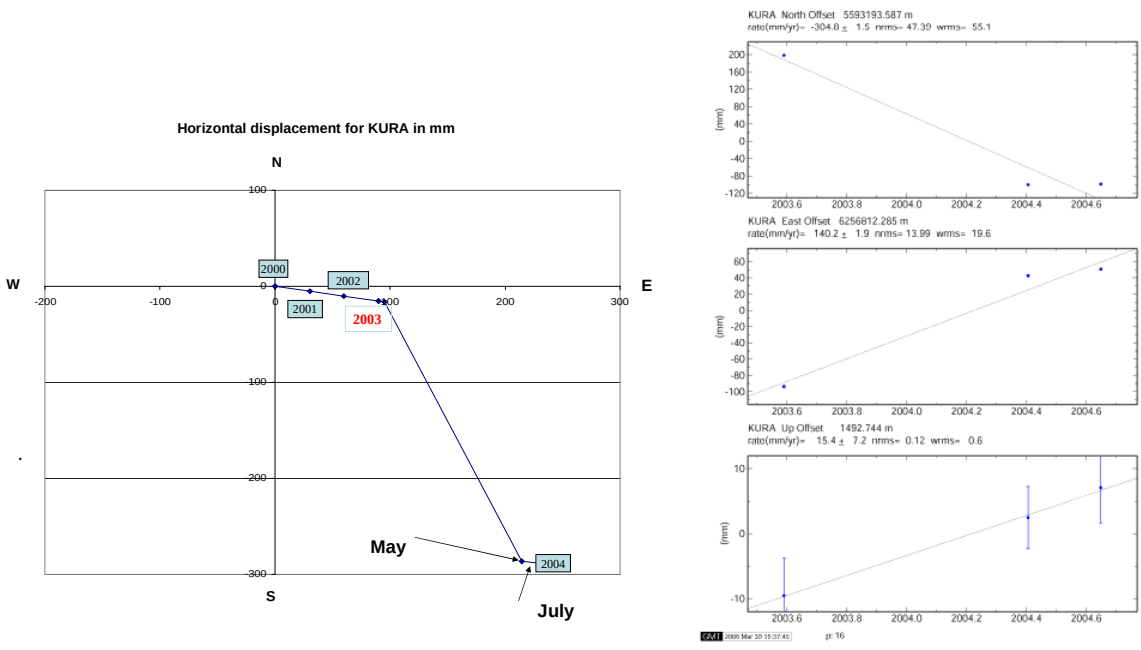

Figure 4: Coseismic jump measured at KURA station due to Chuya earthquake

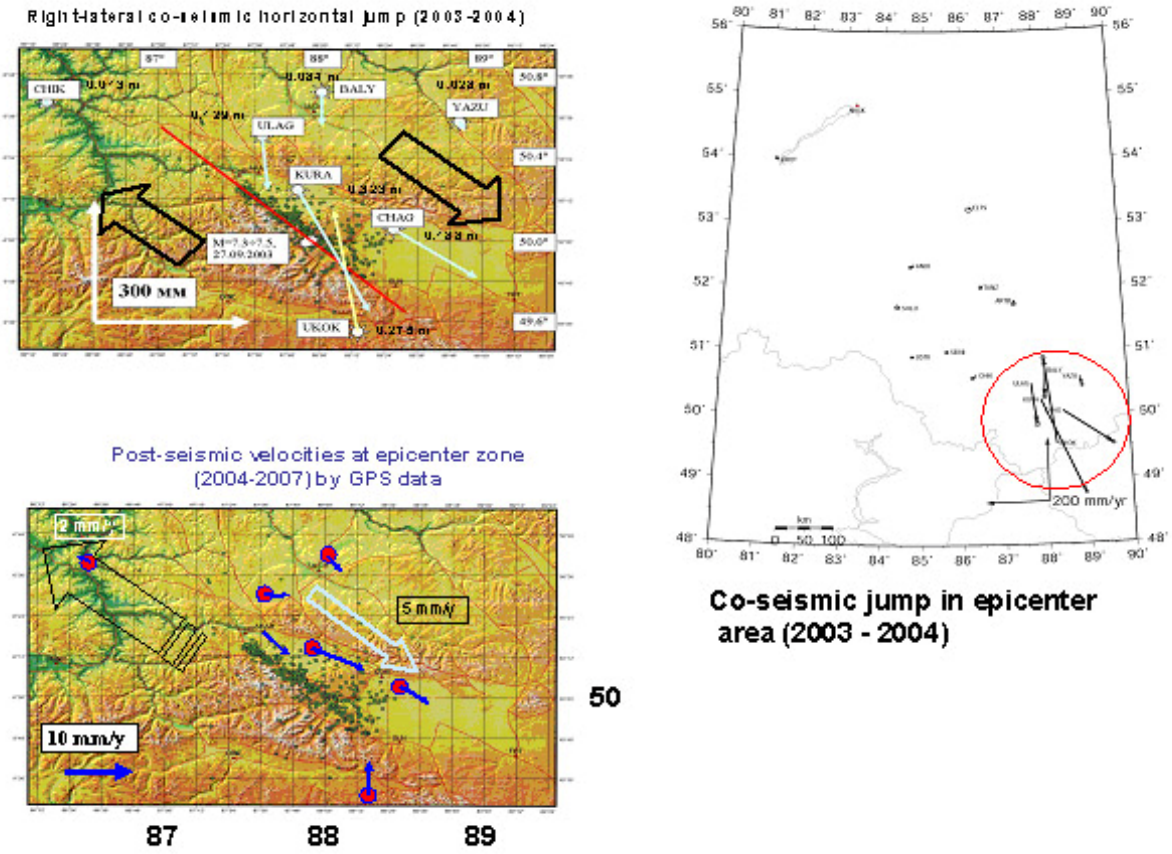

Figure 5: Co- and post-seismic deformation in epicentral area observed with Altay network

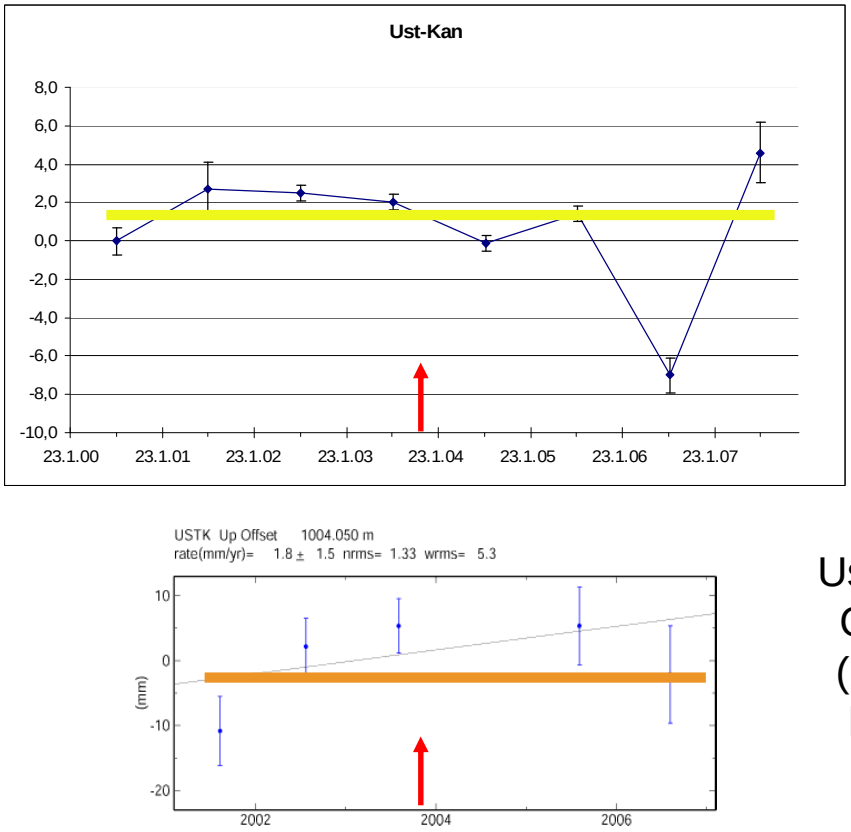

Ust-Kan, bed rock. Gravity variation (2000-2007) and height variation (2001-2006)

Figure 6: Comparison of gravity changes (μgal) and height variations (mm) at Ust-Kan station

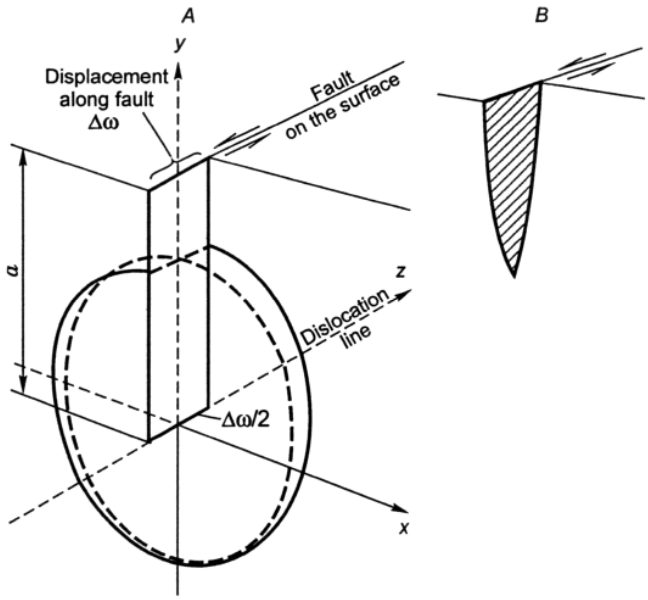

Figure 7. Screw Dislocation Model (SDM, single source).

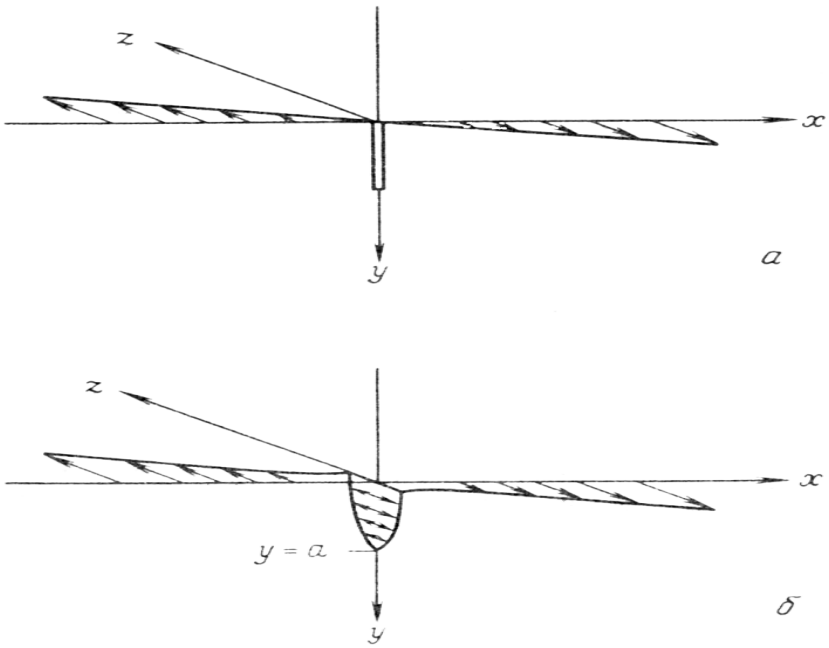

Figure 8. a) 2D Model; b) 2DM, belt source).

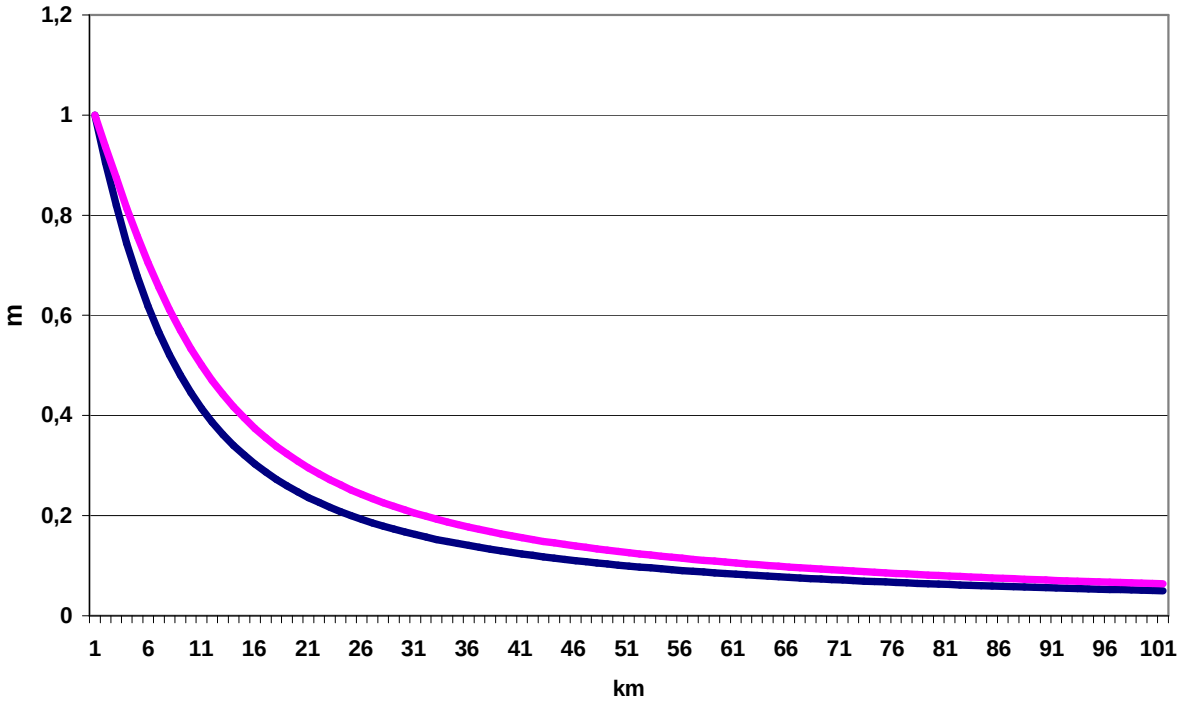

Figure 9: Dislocation according to distance to the rupture plane using SDM and 2DM models

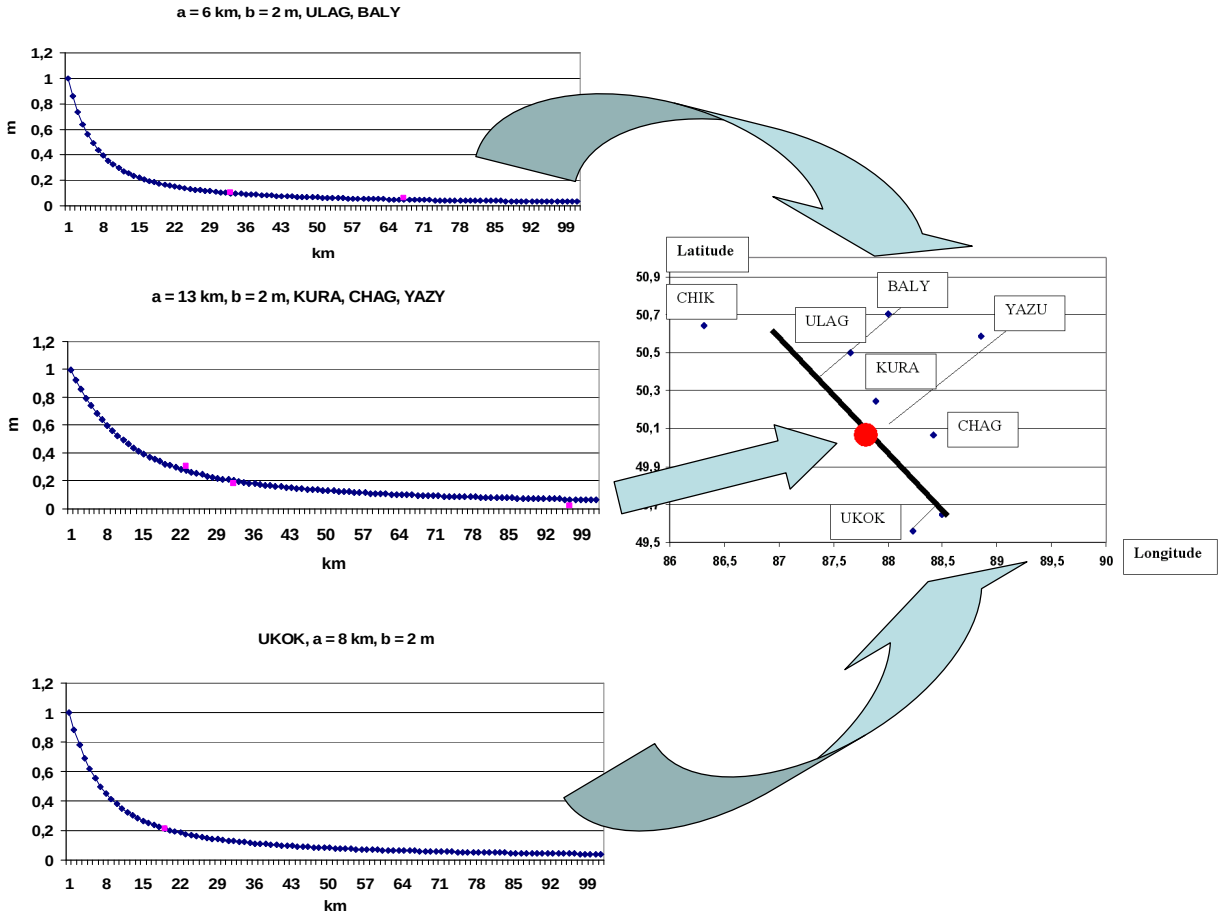

Figure 10: Displacement curves parameters a (depth) and b (slip) determined from the GPS observations (red dots) at different stations using the 2DM model.

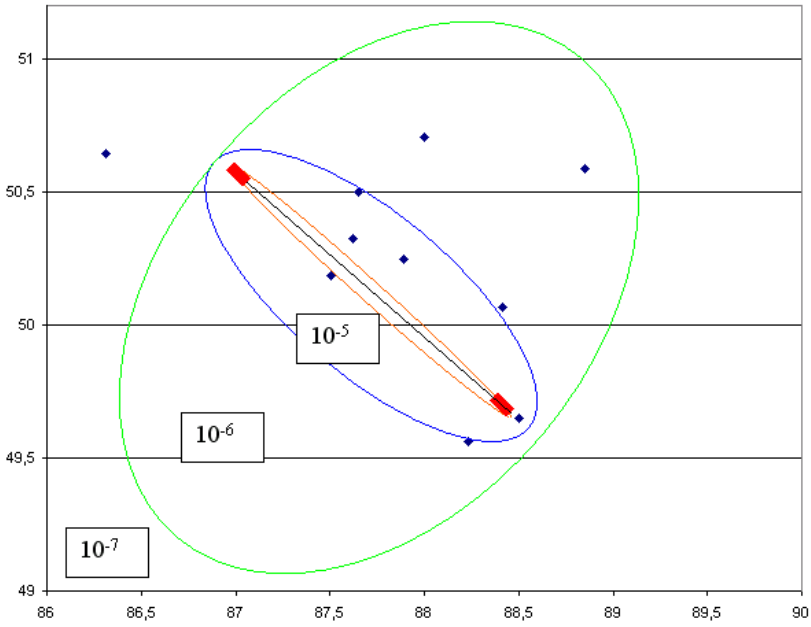

Figure 11: Coseismic shift deformation by 2D model with changing depth, symmetrical change by epicenter (from 15 km to 1 km, deformation Uxy, step - 1 km). Axes are labeled according to latitude and longitude. 10^{-7}, 10^{-6}, 10^{-5}, 10^{-4}, deformed zone up to10^{-3} at the end of line.

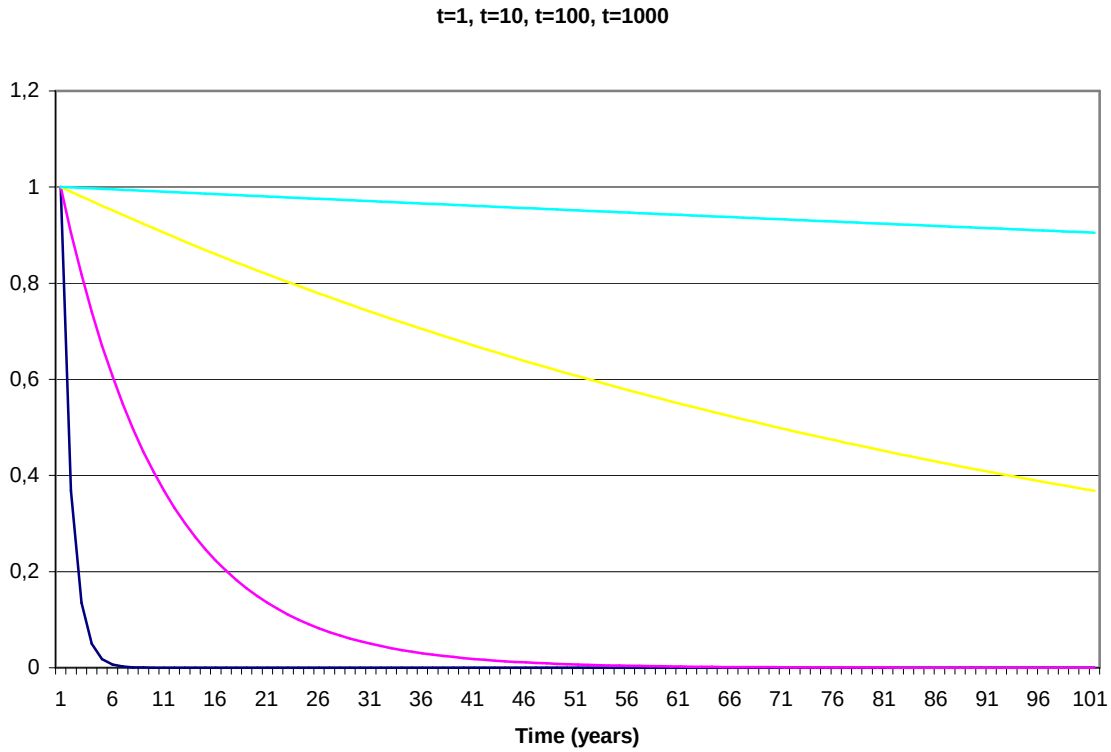
t=1, t=10, t=100, t=1000
1,2
1
0,8
0,6
0,4
0,2
0
1 6 11 16 21 26 31 36 41 46 51 56 61 66 71 76 81 86 91 96 101
Time (years)

a)

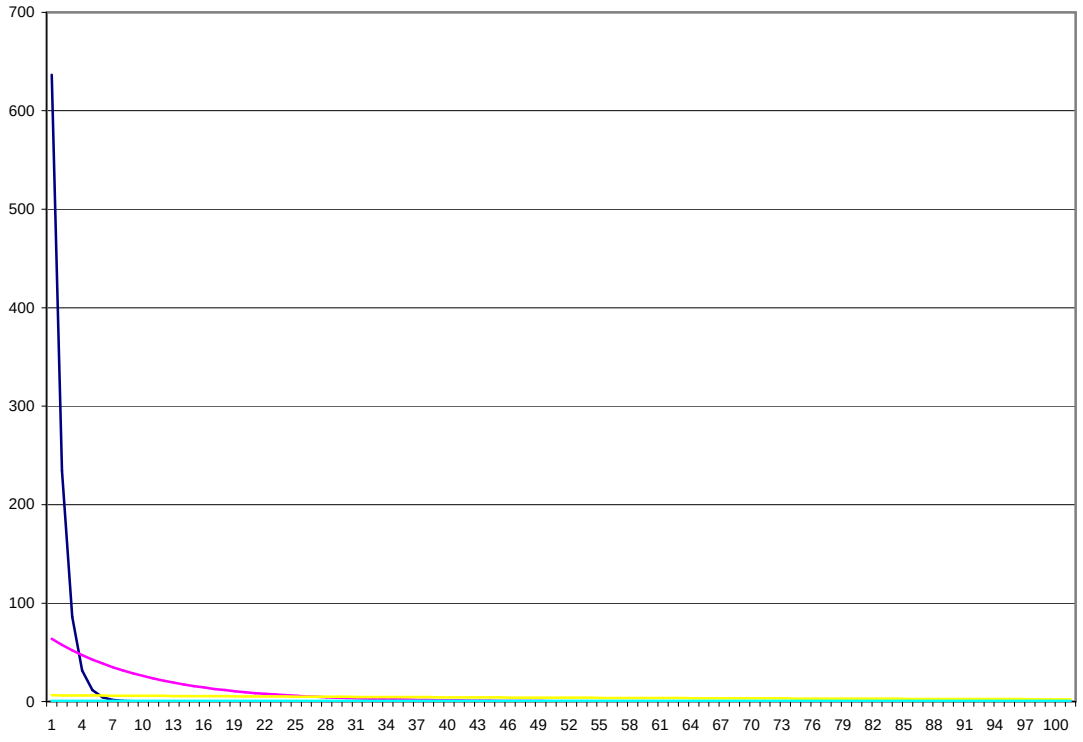
700
600
500
400
300
200
100
0
1 4 7 10 13 16 19 22 25 28 31 34 37 40 43 46 49 52 55 58 61 64 67 70 73 76 79 82 85 88 91 94 97 100

b)

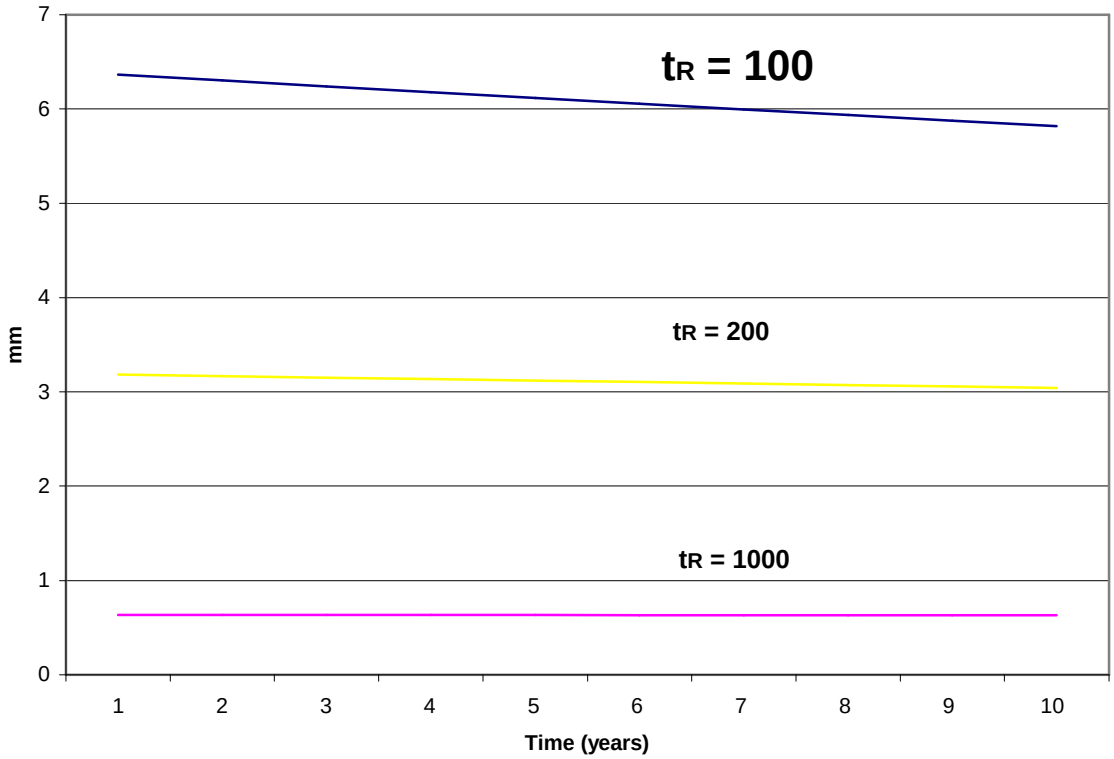

c)

Figure 12. eq. 6 a) $\exp(-t/\tau_R)$, τ_R from 1 to 1000 years;
b) $(\Delta u/\pi \cdot \tau_R) \cdot \exp(-t/\tau_R)$ in mm, τ_R from 1 to 1000 years;
c) $(\Delta u/\pi \cdot \tau_R) \cdot \exp(-t/\tau_R)$ in mm, zoom for τ_R from 100 to 1000 years.

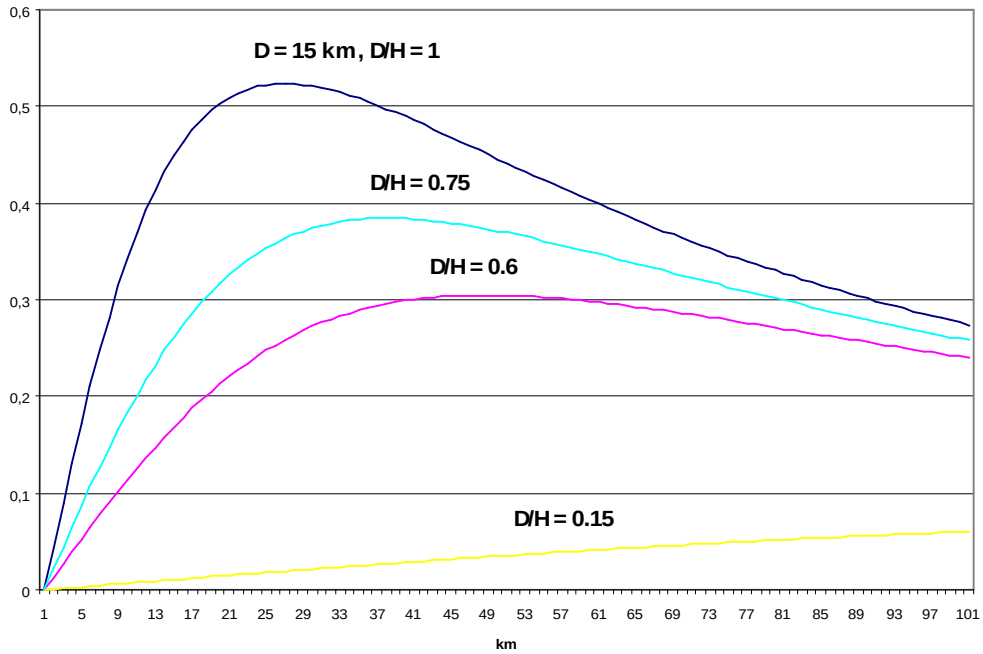

Figure 13. Spatial distribution $F_1(x, D, H) = \tan^{-1}[2xD/x^2 + (2H)^2 - D^2]$ in eq. 6 at distances x from the fault up to 100 km.

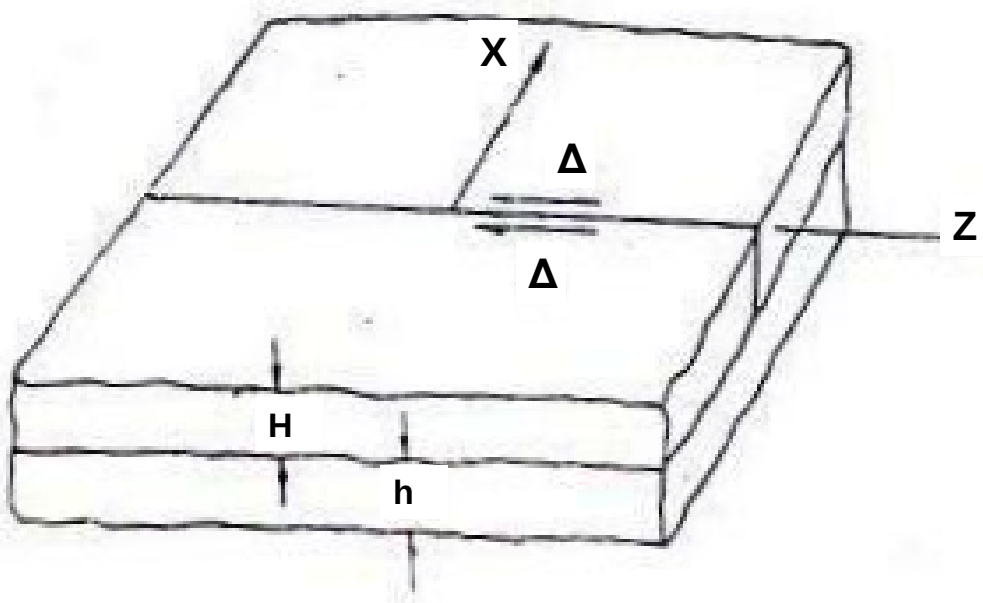

Figure 14. Two layers Elsasser model.

Tidal modulation of weak seismic activity (Baikal rift zone, Altay-Sayan region).

Timofeev V.Y., Van Ruymbeke M.*, Ardyukov D.G., Ducarme B.*
Trofimuk Institute of Petroleum Geology and Geophysics SB RAS, Novosibirsk, Russia
**Royal Observatory of Belgium, Brussell*

Abstract

We show the tidal analysis of Earthquake's data bank for Baikal (1970-1993) and Altay-Sayan regions (1970-2001) by HiCum program. We research correlation of seismic activity in semi-diurnal, diurnal and long period tidal bands. As a result we got 10%-30% modulation for weak seismic process (magnitude M = 0.5÷ 2.0) for K1, S1, Mf and Mm tidal waves. Process modulation in time was analyzed for the Busingol earthquake (M =6.5-7.0, 1991/12/27 09-09-34.9, 51.12°N, 98.15°E) zone. Variation of modulation parameters is present in epicenter zone. Model of process in epicenter zone was discussed as crack genesis. Velocity of crack process is connected with the stress flow parameter i.e. "Stress•Strain Velocity". For weak energy seismic process tidal modulation appeared when this parameter reaches comparable values for tectonic process and for tidal forces. Modulation parameter reached 30% or more before a strong earthquake and after disappeared. When we analyze the Altay-Sayan seismic process we see the migration of process to south-west in the zone of preparation of Chuya earthquake (27/09/2003, M=7.3-7.5).

Key words: HiCum program, earthquake data bank, Baikal rift and Altay-Sayan region, tidal modulation, earthquake models.

1. Introduction

Research of relation between tidal strength and seismic process was made by different authors. Some results show correlation, some-don't [Aoki et al., 1997; Emter et al., 1985; Heaton 1975; Knopoff, 1964; Polumbo, 1986; Shlien, 1972; Simpson, 1967; Tanka et al., 2002; Van Ruymbeke, 1989; Weem&Perry, 1989].

The method of attack is based on the use of a maximum amount of information about earthquakes of the considered region (theoretically - all information). It is obvious, that we study process, on the weak energies, because most information about seismicity comes from weak energy events. For earthquakes data analysis we used a special software for tidal analysis called HiCum. Main topic of this article is research of modulation for seismic events in Baikal rift zone (1970-1993, about 90,000 events) and Altay-Sayan region (1970-2001, about 26,000 events), and its quantitative estimation (Figure 1). Different peculiarities of process in the different areas and its time variations were studied.

2. The HiCum method

The signals from periodic deformations such as earth tides are extremely small and any effects would be difficult to detect. In earlier studies spectral analysis has been the favorite tool for detecting such signals. In our case, we know the period of different components of the signal with an astronomical accuracy. In addition the very long series of records at our disposal gives us the potential to detect very weak signals with significant signal-to-noise ratio. The **Hi**stograms **Cum**ulating method [Bartels, 1938; Series et al., 1994] was originally developed at the Royal Observatory of Belgium for this purpose[Van Ruymbeke et al., 2003]. Its objective is to put forward a graphical display of the behavior of the non-linearities recorded by the sensors. To further simplify the analysis of the data, the HiCum method has been incorporated in the EDAS Grapher software package [Van Ruymbeke et al., 2001].

The inspiration for HiCum came from the field of meteorology where stacking data has been used for many decades. A signal, which at first sight appears like noisy signal, has its time base divided into a series of constant length time periods. The time period will be selected that is suspected to have an influence on the parameters in question e.g. the diurnal *S1* and semi-diurnal *S2* periods for climatic effects, the lunar *M2* period for tidal effects. This time period is, by definition, equivalent to an interval of width 2π or 360°.

For each period, a maximum of 360 sectors of 1° histogram are created and then the results from each time period are synchronized and added (stacked) resulting in an averaging effect producing a picture of the variations, in relation to the selected wave. Figure 2 is a schematic of the method for the wave *M2*.

HiCum has several advantages over Spectrum Analysis in extracting information when there are complex interactions in a multi parameter environment.

We can remove from the histogram the calculated fundamental sine wave and check for any non-linearity or harmonics present. We have the option of removing up to four harmonics from the main signal, leaving only the non-linear residuals.

The method is highly sensitive and has been shown to be capable of detecting non-linear hysteresis on raw data, which at first sight appears to be a white noise signal. This precision, obtained from analyzing the effects of tidal fluctuations on a weak signal from raw data records of a gravimeter, was possible because records were taken repeatedly over years and the results from the same time period each day were added, stacked, resulting in an averaging effect producing a picture of the daily variations. The accuracy of method has been tested on computer generated data. We can regard the background theory. Fourier's Theorem states that any periodic function can be expressed as a sum of sine waves.

$$F(x) = \sum(a \cdot \cos rx + b \cdot \sin rx) + \tfrac{1}{2} c \qquad (1),$$

where r takes integral values and a,b,c are constants.

This can be used as a method of determining the harmonic components of a complex periodic function. Since equation (1) is unchanged by replacing x by $x + 2k\pi$, where k is an integer, it necessarily represents a periodic function in x of period 2π. Consequently in discussing series of this type it is sufficient to consider any interval of width 2π or 360°.

Thus if we have a signal that varies over a period of time, and we can clearly define the frequency, $\omega/2\pi$, then we can equate that to the interval 2π (or 360°) and equation (1) becomes:

$$F(t) = \sum(a \cdot \cos \omega t + b \cdot \sin \omega t) + \tfrac{1}{2} c \qquad (2),$$

where t is the instantaneous time. With ω clearly defined, the various harmonics of the system can be found.

HiCum has been developed to analyze data linked with tidal phenomenon (e.g. *M2*) where the time period can be accurately defined and is stable. Using HiCum the parameters of the fundamental sine wave, the harmonics and any non-linearity in the signal can be detected on weak signals with high noise levels.

Statistic models of modulation method was discussed in article [Goldin et al., 2008] Let us consider a sinusoidal signal of amplitude B_0 superimposed on a background A_0.

$$F(t) = A_0 + B_0 \cdot \sin(\omega t + \varphi) \qquad (3)$$

or

$$F(t) = A_0 [1 + B_0 / A_0 \cdot \sin(\omega t + \varphi)] \qquad (4)$$

As

$(A_{max}+A_{min}) = 2A_0$

and

$(A_{max}-A_{min}) = 2 B_0$

we get

$$F(t) = A_0 [1 + m \cdot \sin(\omega t + \varphi)] \qquad (5),$$

with modulation m given by

$$m = (A_{max}-A_{min}) / (A_{max}+A_{min}) \qquad (6)$$

An example is given in Figure 3.

We can also write

$$F(t) = A_0 \cdot \cos\Omega t[1 + m\sin(\omega t + \varphi)],$$

or sum of low frequency signal and high frequency signal (noise)

$$F(t) = \lim_{\Omega \to \infty} \{A_0 \cdot \cos\Omega t[1 + m\sin(\omega t + \varphi)]\} \quad (7)$$

For statistic model we have [Goldin et.al., 2008]

$$m_S = [N \cdot \max L(\varphi)] / [\sum^{N}_{r=1} \cos^2(\omega \cdot r \cdot \Delta t - \varphi)] \quad (8)$$

where $N > 20$ (we have $N \geq 24$).

If we want to find estimation with signal/noise = 3 for m: 0.01, 0.05, 0.10, 0.15, 0.20, 0.25, 0.30, we must have BANK of events: 180,000, 7,200, 1,800, 800, 450, 288 and 200.

3. Analysis of Altay-Sayan data as a function of the energy level

Earthquake data bank includes for 1970-2001 years period 26,126 events registered by Altay-Sayan seismology service and by Institute of Geophysics SB RAS (Novosibirsk). Latitude φ, longitude λ, and energy class K* of events are presented on Figure 4. Earthquakes are given from energy class 6 and up for period 1970-1991, and from 9-class for period 1992-2001. Analyses for Altay-Sayan territory are presented with separation in two blocks.

We start analyze for S1 wave with different steps for HiCum (1970-1991, Figure 5). When we check the data bank, we can see that more reliable level is near 7.6-class. Weak effect in longitude and in latitude appeared in result. Modulation for S1 wave (real daily period) is 14.6% ÷ 15.7%. Results for Mf, Mm and Sa waves presented in figure 6 and modulation are 3.2% ÷ 15.3%. For Mf wave (figure 6, 7) there is a dependence for longitude, latitude and energy.

Second part of Altay-Sayan data (1992-2001) is for class 9 and up and the more reliable level is near 9.5-class (figure 7). Analysis of the second part for S1 wave presented a reduction of modulation to 5.1% (figure 7). We can conclude that tidal modulation is maximum for weak energy events (from 6 to 8 class or M = 1.0 ÷ 1.5). This fact is illustrated on figure 8. When the energy of the events decreases the coefficient of modulation increases.

* For energy in Joule: log E = K, M = -3.64 + 0.70 K

4. Analysis of Baikal rift data including spatial distribution of modulation effect

Earthquake data bank includes for 1970-1993 period 90,220 events registered by Baikal seismology service and by Institute of Earth Crust SB RAS (Irkutsk). A first study of the "Tidal variation-Weak seismic activity" connection is presented here. Depth distribution of earthquakes for Baikal rift is presented on Figure 9. Energy of events for the 1970-1993 data bank is given from energy class 6 level up to 16 level or in other system – Richter magnitude – from M = 1 up to M = 7 (Figure 10). When we check the data bank, we can see that it is more reliable to use the lower level 7 ÷ 8 class or M=2. This level range was analysed by HiCum program. Geological & geophysical features of region allow us to cut the studied territory into three blocks according to stress condition, deep structure (depth of Moho) and kind of faults (Figure 11). We have three blocks delimited in longitude: 92°- 107°; 107°- 115°; 115°-126° (block 1, block 2 and block 3). The first one is the left flank of the rift with E-W lateral faults. The second one is the rift zone with SW-NE orientation of main features and the third one, corresponding to the right flank, is a zone with E-W lateral faults too. For the S1 wave (Doodson argument number 164.555) with 90 steps for HiCum, we can see different reactions in the first, second and third blocks (see the figure 11). In the first block is one kind of modulation and in the third one –other flank – there is

the opposite effect. Effect is strong on the left flank up to 17.0%. The modulation is reduced to 10.1% in the central block and in right flank to 3.6% (block 3). S2 modulation is different – first block – 9%, second block – 8%, and third block – 8%. The modulation is practically constant. When we try to estimate the situation as a function of latitude, longitude and energy (class of earthquake) we see the modulation on all these parameters for first block. We have a smaller effect for latitude, but real effect in longitude in second block. Effect is not significant for latitude, longitude and energy in third block. Relation between energy and number of earthquakes is linear for first block and without any correlation for other blocks.

Next step of analyze is the estimation of modulation for block 1. Smoothed data and seismology analyses show the source of such a strong effect (Figure 12). It is a strong earthquake at Busingol Lake, Mongolia (27.12.1991, 51.0°N, 98.0°E, M = 6.5 ÷ 7.0). This zone is present in Altay-Sayan data bank and in Baikal rift data bank. It is a territory where compression typical of Altay-Sayan region changes to Baikal rift extension condition. Testing of this territory showed the different effects before and after earthquake (Figure 13). Large modulation effect (30%) is existing during the four years period before earthquake. It is reduced to 12% within 6 months after Busingol earthquake (Figure 14).

Result of smoothing Altay-Sayan data bank (1992-2001) is presented in Figure 15.On the smoothing result (for 100 events) presented in longitude, latitude and energy we remark the migration of seismic process to south-west where Chuya earthquake happened (27.09.2003 г, M = 7.3, 50.064 °N, 87.731°E). An increasie of energy level can be seen in this graph too.

5. An attempt of theoretical understanding

As we see tidal effect is present in weak seismic activity. We can presuppose some control parameters in the medium. These parameters determine defects generation. Usually these parameters are the temperature, stress tensor and tensor of strain velocities [Zhurkov, 1983, Goldin et. al., 2008]. If tensor structure is fixed these parameters ($T°$, σ and $\dot{\varepsilon}$) can be used as a scalar. We can use stress flow ($\sigma d\varepsilon$), if temperature changes weakly. Our task is estimation of roles $\dot{\varepsilon}_{xz}, \dot{\varepsilon}_{zz}, \sigma_{xz}$ и σ_{zz} for tidal modulation. If seismic intensity $\lambda(t)$ reflects the growth of defect density (crack density) ψ: $\lambda(t) = d\psi(t)/dt$, the equation connecting defect density with control parameters is evolution type equation:

$$\frac{d\psi}{dt} = G(\psi, \nabla\psi, \mathbf{g}), \qquad (9),$$

where $\mathbf{g}$ -vector of control parameters, ψ - defect density.

If right side is proportional to defect value (ψ^q) and $q > 1$ we have speed unstable process, as fore-shock process. If *q = 0* or *q = 1*, we have process controlled by parameters, it may be periodic process when parameters have periodic character. When we have q < 0, the equation describes a delay-process, as after-shock process. For a very large area and for long period, it is a stationary process. For this territory the gradient $\nabla\psi$ is equal to zero as an average and we can use one dimension equation:

$$\frac{d\psi}{dt} = G(\mathbf{g}) \qquad (10)$$

If defect increment is proportional to energy increase:

$G(\mathbf{g}) = A[(\sigma^0_{zz} + \sigma_{zz})(\dot{\varepsilon}^0_{zz} + \dot{\varepsilon}_{zz}) + (\sigma^0_{xz} + \sigma_{xz})(\dot{\varepsilon}^0_{xz} + \dot{\varepsilon}_{xz})]^n$, where - σ_0 and $\dot{\varepsilon}_0$ - geodynamic stress and geodynamic strain velocity, *n* – structure parameter, A – constant for standardization. For tidal variation:

$$d\psi/dt = A[1 + \alpha_z \sin\omega t + \beta_z \cos\omega t + \gamma + \gamma\alpha_z \cos\omega t + \gamma\beta_x \sin\omega t + \cdots]^n =$$
$$= A'[1 + m\sin(\omega t - \varphi) + \cdots]$$

$$\gamma = (\sigma^0_{xz})(\dot{\varepsilon}^0_{xz})/(\sigma^0_{zz})^n(\dot{\varepsilon}^0_{zz})^n,\ \gamma < 1 \text{ (for Altay territory).} \qquad (9)$$

Geodynamic parameters:
by GPS: $4\cdot10^{-8}$/year or $4.6\cdot10^{-12}$/h or $1.3\cdot10^{-15}$/sec (rate of horizontal compression), $1\cdot10^{-8}$/year or $1.1\cdot10^{-12}$/h or $3.2\cdot10^{-16}$/sec (rate of vertical extension), 4 MPa (stress) ["Pre, co and post-seismic…", Timofeev et.al., 2008].
Parameter "Stress•Strain Velocity" $4\cdot10^6$ x $5\cdot10^{-12}$ Pa/h = $2\cdot10^{-5}$ Pa/h.
Tidal parameters:
Stress = (strain · elastic modulus) = $\varepsilon\cdot G$, max value for volume strain (Figure 16) $100\cdot10^{-9}$, if G = 55 GPa; we have $\varepsilon\cdot G$ = 5.5 KPa (maximum estimation for tidal stress).
Horizontal rate $100\cdot10^{-9}$/24h or $4.2\cdot10^{-9}$/h or $1.1\cdot10^{-12}$/sec.
Parameter "Stress•Strain Velocity" $5.5\cdot10^3$ x $4.2\cdot10^{-9}$ Pa/h = $2\cdot10^{-5}$ Pa/h.
As we used peak to peak amplitudes of the tidal variations, energy is only the fourth part of this estimation. We used the daily range of tidal effect (wave S1 as average frequency). As a matter of fact daily period can mix up with air pressure and surface temperature effects.
The ratio "Tidal parameter/Geodynamic parameter" is 25%, similar to experimental modulation.

6. Conclusions

We presented the tidal analysis of Earthquake's data bank for Baikal (1970-1993) and Altay-Sayan regions (1970-2001) by HiCum program. We are looking for seismic activity modulation for semi-diurnal, diurnal and long period tidal bands. As a result we have 10%-30% reaction (modulation) for weak seismic process (magnitude M = 0.5÷ 2.0) for K1, S1, Mf and Mm tidal waves. Process modulation in time was analyzed in Busingol earthquake zone (M =6.5÷7.0; 1991/12/27 09-09-34.9; 51.12°N, 98.15°E). Variation of modulation parameters is presented for epicenter zone. Model of process in epicenter zone was discussed as crack genesis. Velocity of crack process is connected with parameter "Stress•Strain Velocity". For weak energy seismic process modulation appeared when this parameter reaches comparable values for tectonic process and for tidal forces. Modulation parameter reached 30% or more before strong earthquake and after disappeared. Our investigation has been supported by grant RFBR 07-05-00077.

References

1. Aoki S., Ohtake M., Sato H. Tidal modulation of seismicity: an indicator of the stress state? The 29-th General Assembly of the International Association of Seismology and Physics of the Earth's Interior. Abstracts. Aug. 18-28, 1997. Thessaloniki, Greece. P. 347.
2. J. Bartels. Random Fluctuations, Persistence and Quasi-persistence in Geophysical and Cosmical periodicities. // Terr.Magn.Atmos.Electricity, Vol. 40(1), pp. 1-60, 1938.
3. D. Emter, W. Zurn, R.Schick and G.Lombardo. Search for Tidal Effects on Volcanic Activities at Mt. Etna and Stromboli. // Proceedings of the Tenth International Symposium on Earth Tides, pp. 765-774, 1985.
4. Goldin S.V., Timofeev V.Y., Van Ruymbeke M., Ardyukov D.G., Lavrentiev M.E., Sedusov R.G. 2008, Tidal modulation of low seismicity in Southern Siberia. // Physical Mezomechanic, vol.11, No.4, pp.81-93.ISSN 1683-805x.
5. HeatonT. H. Tidal triggering of earthquakes // Geophys. J. Roy. Astron. Soc. 1975. V. 43. P. 307-326.
6. Knopoff L. Earth tides as triggering mechanism of earthquakes // Bull. Seismol. Soc. Amer. 1964. V. 54. P. 1865-1870.
7. Melchior P., Tidal interactions in the Earth Moon system. // Chronique U.G.G.I., N210, Mars/Avril, MHN, Luxembourg, 1992. p. 76-114.

8. Polumbo A. Lunar and solar tidal components in the occurrence of earthquakes in Italy // Geophys. J. Roy. Astron. Soc. 1986. V. 84. №1. P. 93-99.
9. Series. W. Zurn and P.A. Rydelek. Revisiting the phasor-walkout method for detailed investigation of Harmonic Signals in Time // Surveys in Geophysics, pp. 409-431, Vol. 15, 1994.
10. Shlien S. Earthquake-tide correlation // Geophys.J. Roy. Astron. Soc. 1972. V. 28. P. 27-34.
11. Simpson J. F. Earth tides as a triggering mechanism for earthquakes // Earth and Planet. Sci. Lett. 1967. V. 2. P. 473.
12. Solonenlo A.V., 1993, Symmetry of Baikal rift stress field. // Doklady Earth Sciences, vol.328, No.6, 674-677.
13. Tanka S., Ohtake M., Sato H. Evidence for tidal triggering of earthquakes as revealed from statistical analysis of global data // Journal of Geophysical Research. V. Solid Earth. 2002. V. 107. №10.
14. Timofeev V.Y., Ardyukov D.G., Stus Y. F., Kalish E. N., Boyko E.V., Dedusov R. G., Timofeev A. V., Ducarme B., 2008. Pre, co and post-seismic motion for Altay region by GPS and gravity observations// Bull. Inf. Marées Terrestres 144,
15. van Ruymbeke M., Beauducel Fr., Somerhausen A.. The Enviromental Data Acquisition System (EDAS) developed at the Royal Observatory of Belgium. // Journal of the Geodetic Society of Japan, Vol. 47 (1), 2001.
16. van Ruymbeke M., Ducarme B., De Becker M.. Attempt model the tidal triggering of Earthquakes. // Proceedings of the Eleventh International Symposium on Earth Tides Helsinki, 1989, Edited by J. Kakkuri p.651-660.
17. van Ruymbeke M., Howard R., Pütz E., Beauducel Fr., Somerhausen A., Barriot J.-P. An Introduction to the use of HICUM for Signal Analysis. // Bull. Inf. Marées Terrestres, 2003, 138, 10955-10966.
18. Weem R. E., Perry W. H. Strong correlation of major earthquakes with solid-earth tides in part of the eastern United States // Geology. 1989. V. 17. P. 661-664
19. Zhurkov S.N. Dilato-mechanism of solid body strength // Physics of Solid Body , n.10, 1983, 3119-3123.

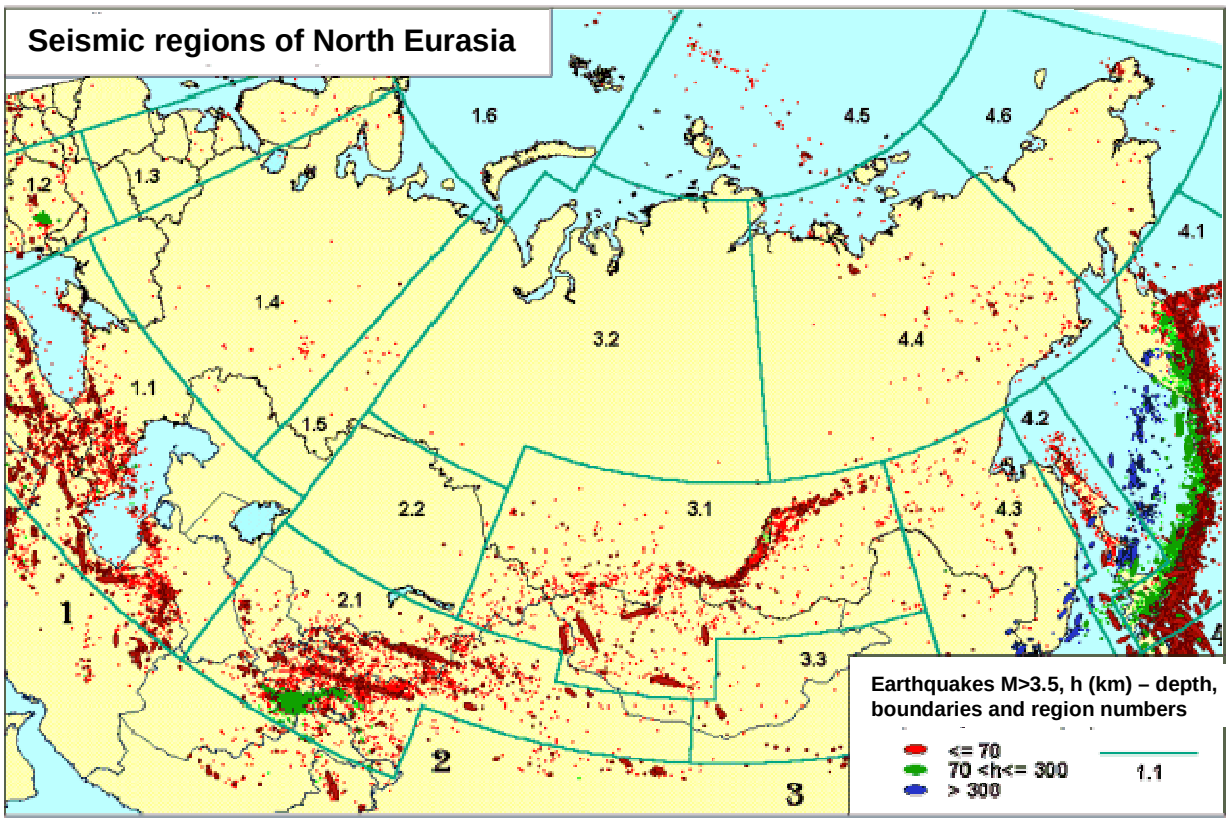

Figure 1. Seismic regions of North Eurasia. Our region is 3.1.

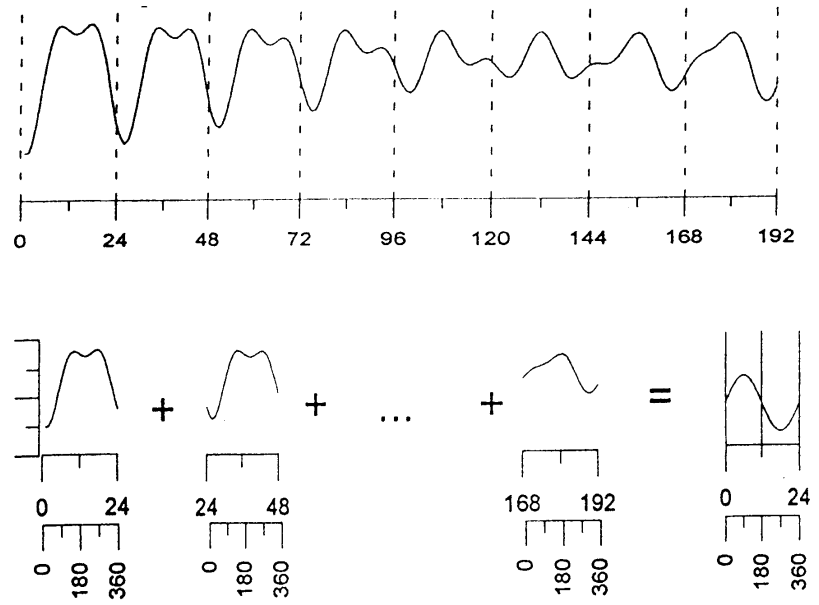

a)

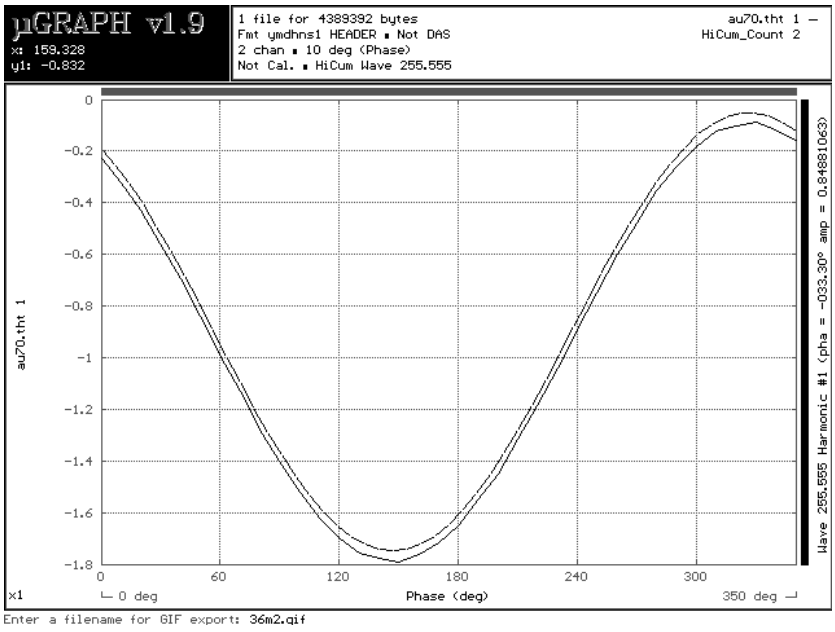

b)

Figure 2. a) HICUM method and analysis of theoretical tide:
b) example on the 12h 25min period (wave M2)

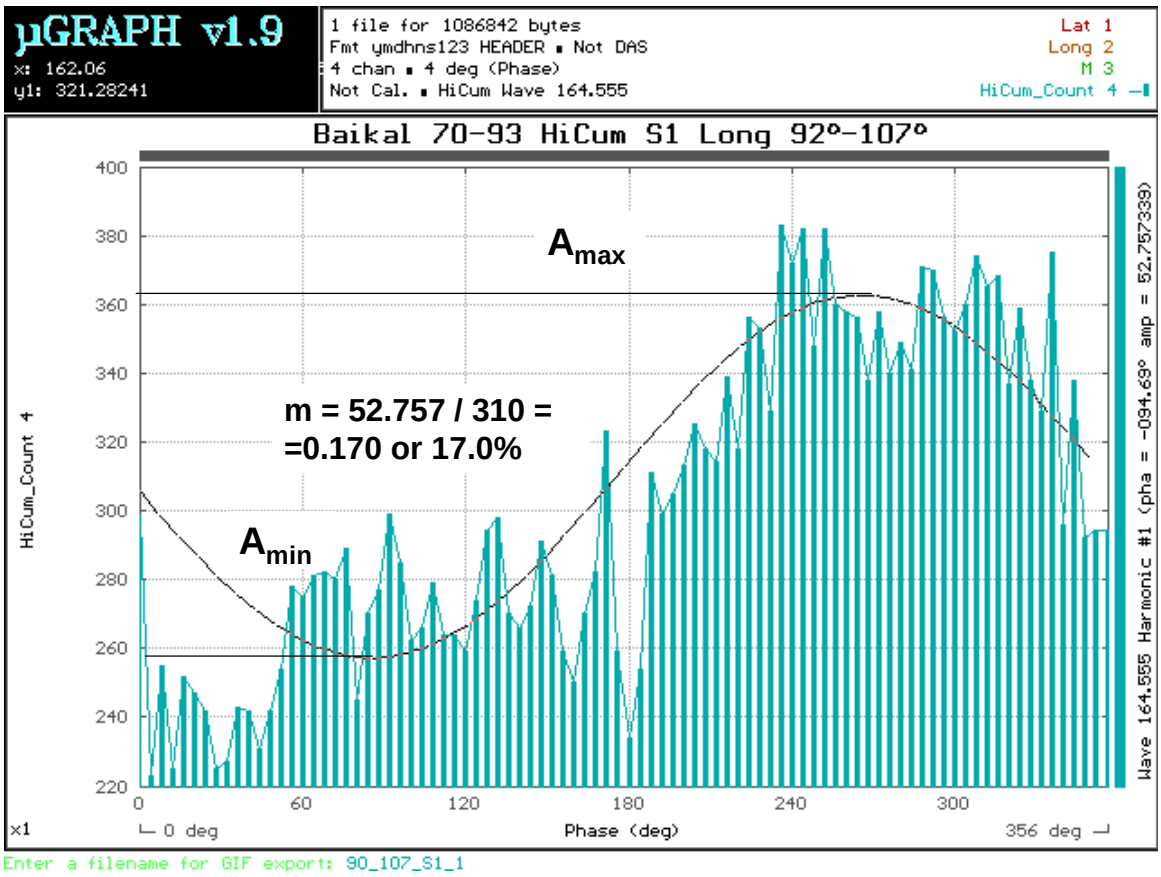

Figure 3. Analysis of Baikal seismic activity (wave S1), western part – 27,900 events. Quantity of sectors may be: N = 24÷360.
In case of random process we have 310 events for every sector (N = 90) and m = 0.
We observe a modulation m = $(A_{max}-A_{min})/(A_{max}+A_{min})$ = 0.17 or 17%

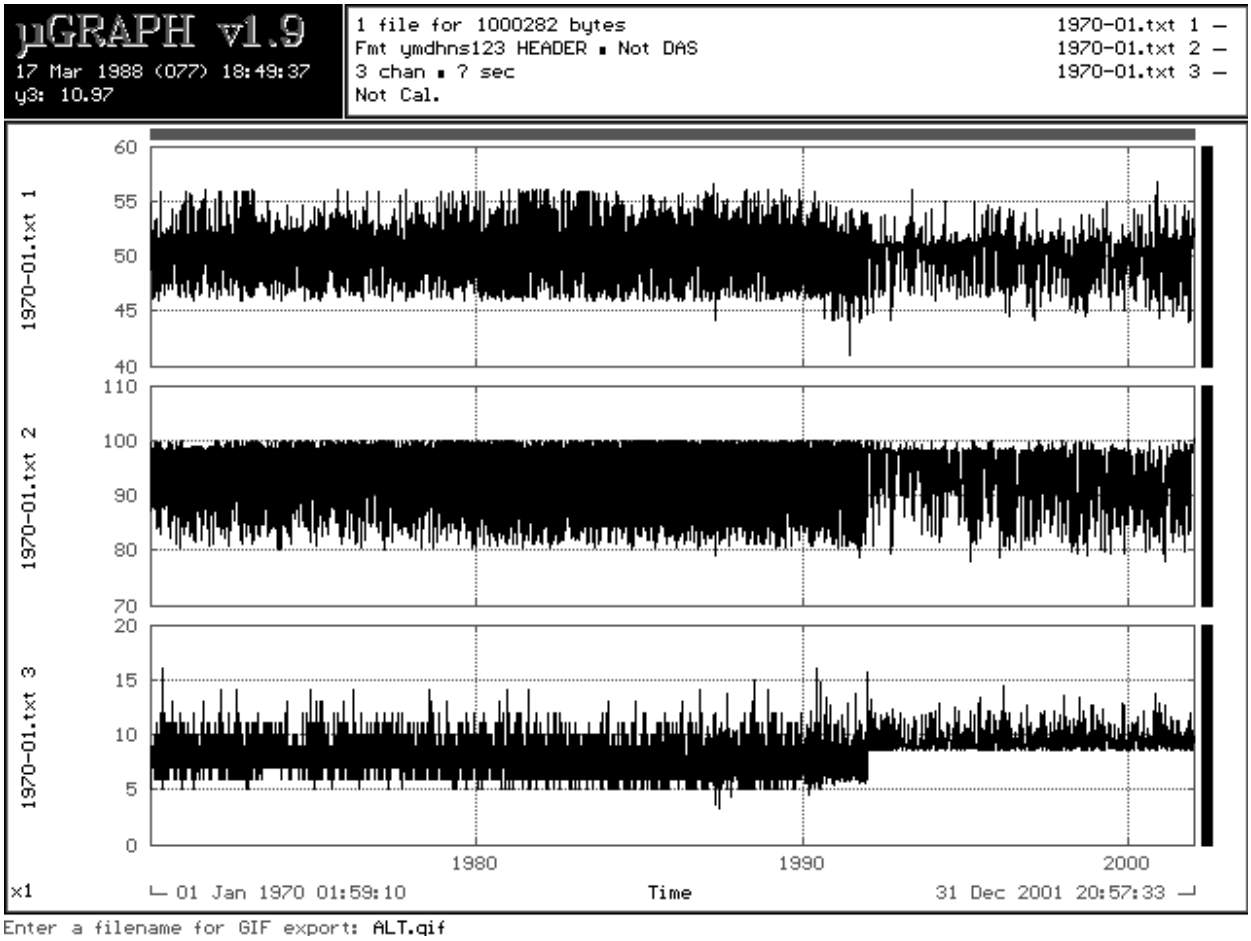

Figure 4. Altai-Sayan bank since 1970: parameters (φ, λ, K): latitude range 46°N÷56°N; longitude range 80°E÷100°E; energy K > 5 (M> 0.5).
Energy E^K Joule, log E = K, M = -3.64 + 0.70 K.

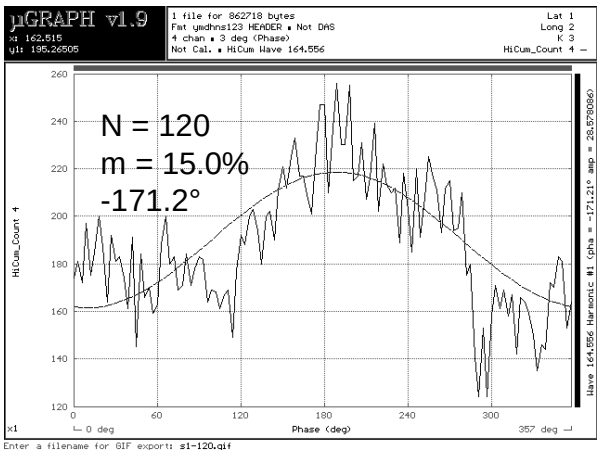

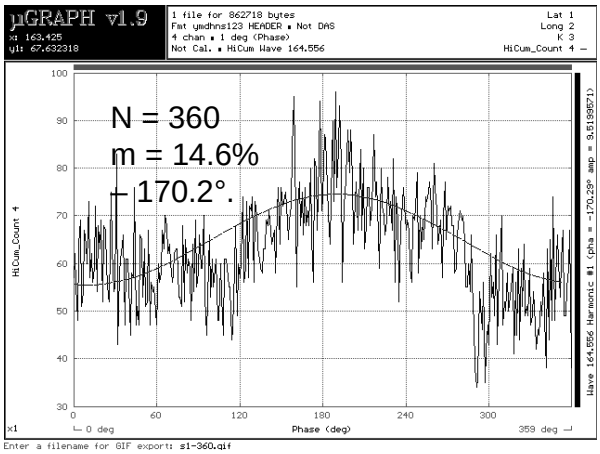

Altay-Sayan region,

near 25000 events, 1970–1991 yy.,
K > 5, wave S1 (really daily period),
quantity of sectors N =120 and 360,
modulation in percents
m = 15.0% and 14.6 %,
phase = -171.2°and – 170.2°.

Bank 1970-2001, (1970-1991, K >5;
1992-2001, K>8.5, M>2.5),
S1, N =72, m = 15.7%.

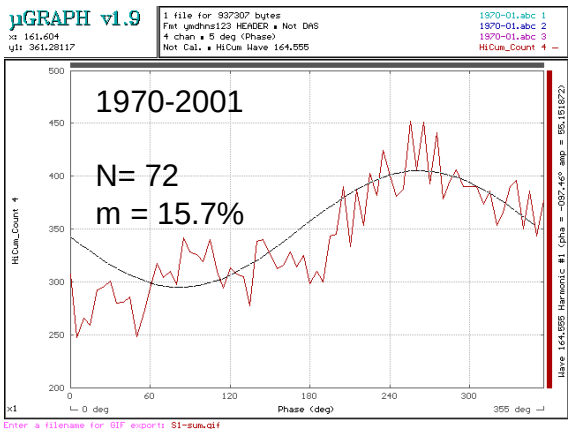

Figure 5. Altay-Sayan region –
left - 1970–1991 period, K > 5, wave S1 (daily period),
quantity of sectors N =120 and 360, modulation in percents m = 15.0% and 14.6 %, phase lag = -171.2°and – 170.2°;
right - 1970-2001 period, wave S1, N =72, m = 15.7%.

Altay-Sayan region, bank 1970 – 1991 yy. and bank 1970-2001, wave Mf, Mm and Sa. m = 3.2% - 15.3%.

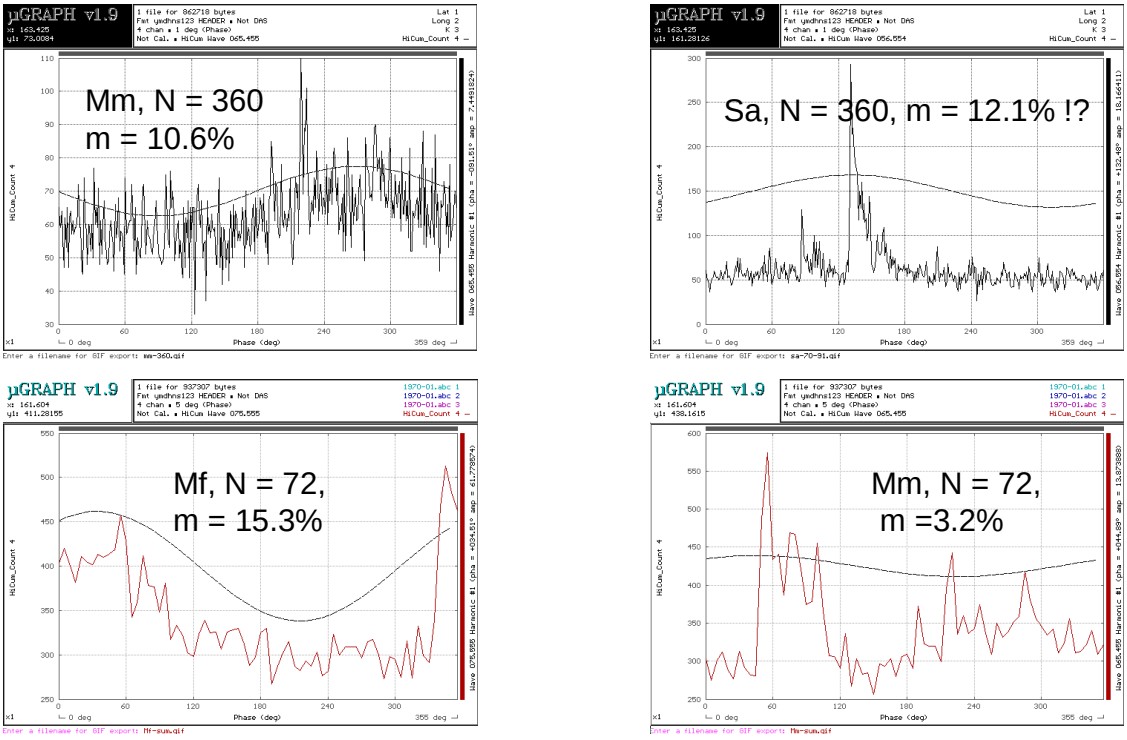

Figure 6. Altay-Sayan region – 1970–2001 period, quantity of sectors N = 72 (Mf, Mm) and 360 (Mm, Sa), modulation in percents from 3.2% to 15.3%.

Altay-Sayan region,

1500 events, 1992 – 2001 yy., K > 8.5, wave S1, Mf, K1, O1, N =72.

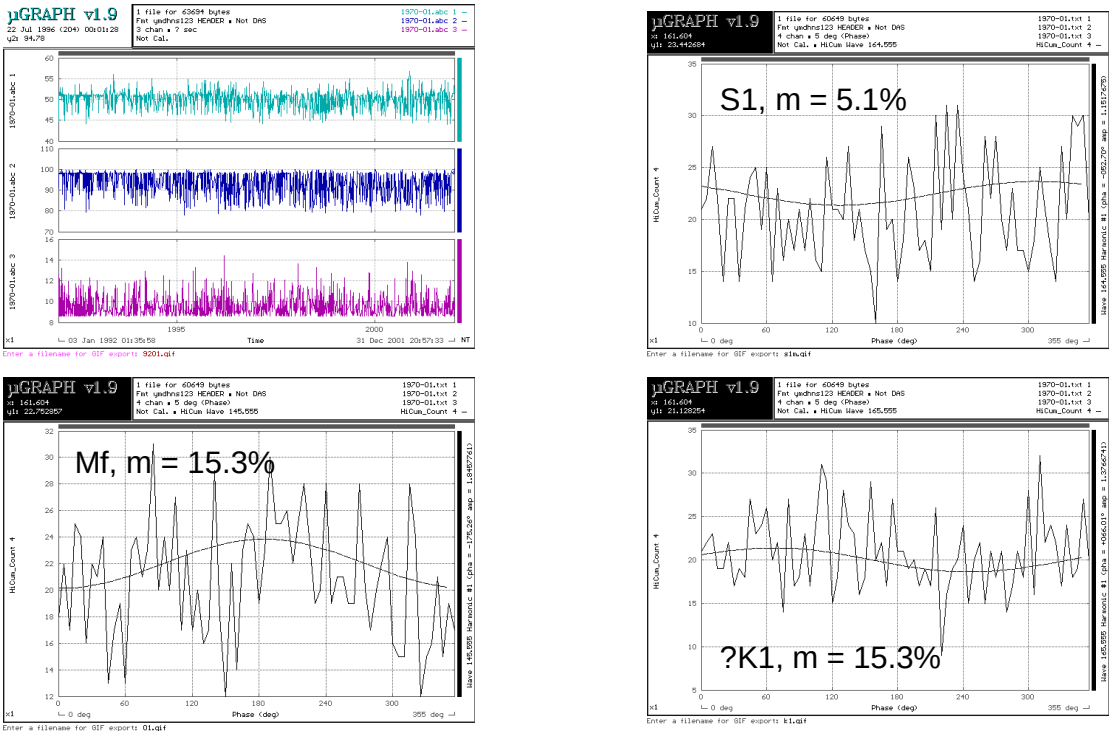

Figure 7. Altay-Sayan region – 1992–2001 period (ϕ, λ, K), energy K > 8.5, waves S1,Mf, K1, quantity of sectors N = 72, modulation in percents from 3.2% to 15.3%.

Energy Level

Altay-Sayan region, 1970 – 1991 yy., wave S1, N = 72,
6 ≤ K ≤ 9; 23400 events, m = 16.6%; 6 ≤ K ≤ 7; 12240 events, m = 27.8%;
7 ≤ K ≤ 8; 17280 events, m = 15.8%; 8 ≤ K ≤ 9; 9000 events, m = 6.4%

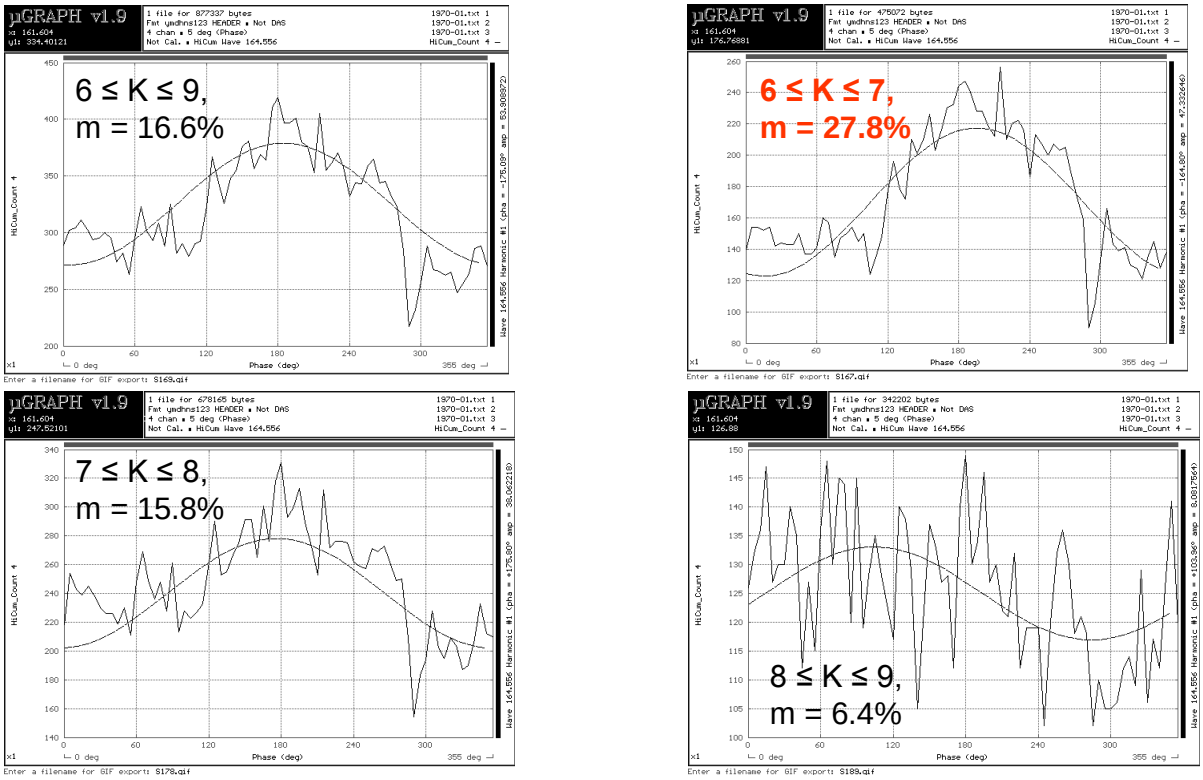

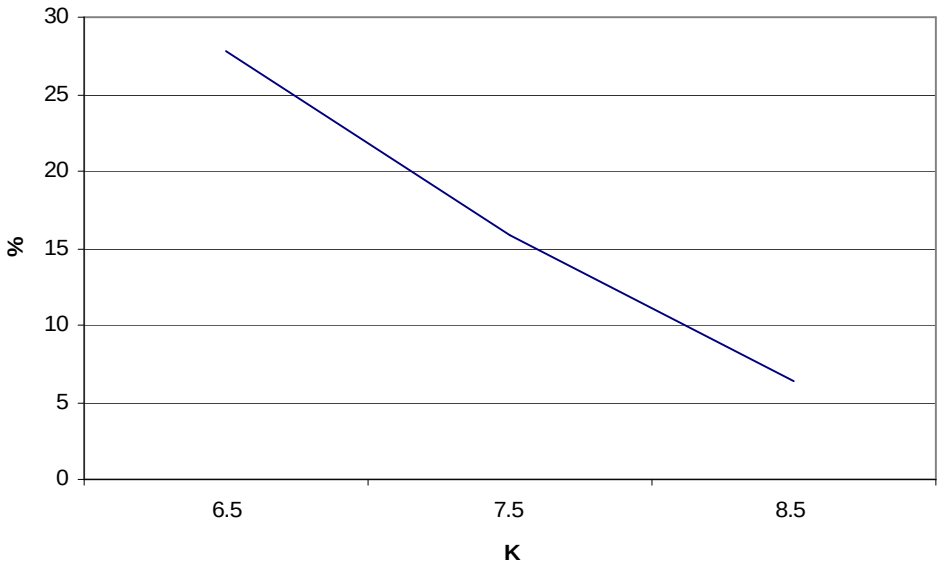

Figure 8. Modulation on S1 as a function of energy parameter K (crustal earthquakes, depth level 5÷25 km).

Tidal variation and weak seismic activity.

Baikal rift, Talaya station, borderland for Siberian platform and western part of Baikal Rift – July and December 2000 year. Series of feeble earthquakes (1-5 km distance), K > 2, July 2000 year; K > 3, December 2000 year. Theoretical tidal curves.

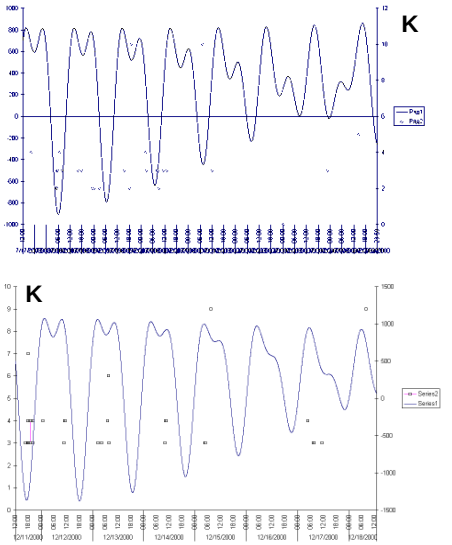

Baikal rift, depth distribution of earthquakes

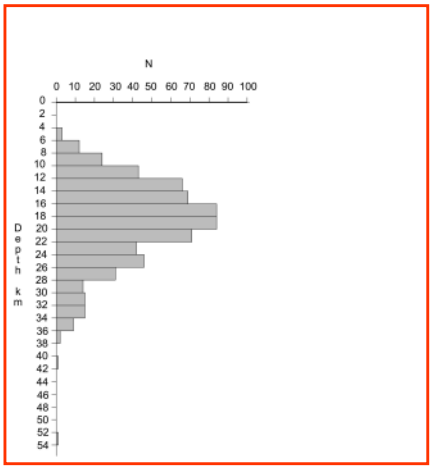

Figure 9. Tidal variation and weak seismic activity.
Baikal rift, Talaya station (51.681°N; 103.644°E; H = 550 m), borderland Siberian platform and western part of Baikal Rift –

Left) July and December 2000. Series of feeble earthquakes (1-5 km distance),
K > 2, July 2000 and K > 3, December 2000 superimposed on theoretical tidal curves.
Right) Repartition of earthquakes with depth

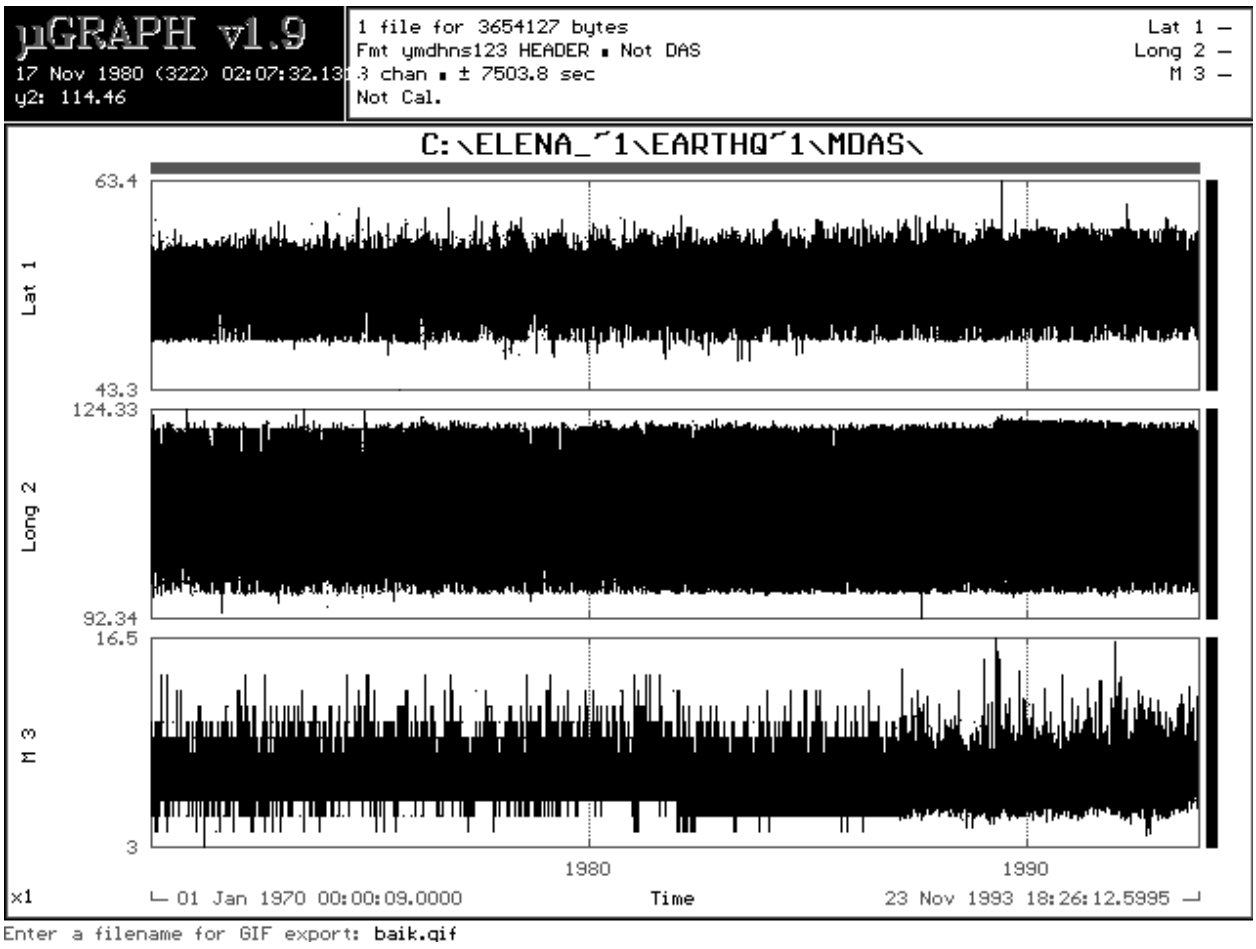

Figure 10. Baikal Rift data bank (φ, λ, K) from 1970 to 1993. Baikal rift territory: 48°N ÷ 59°N; 96°E ÷ 122°E; K> 5 (M>0.5).

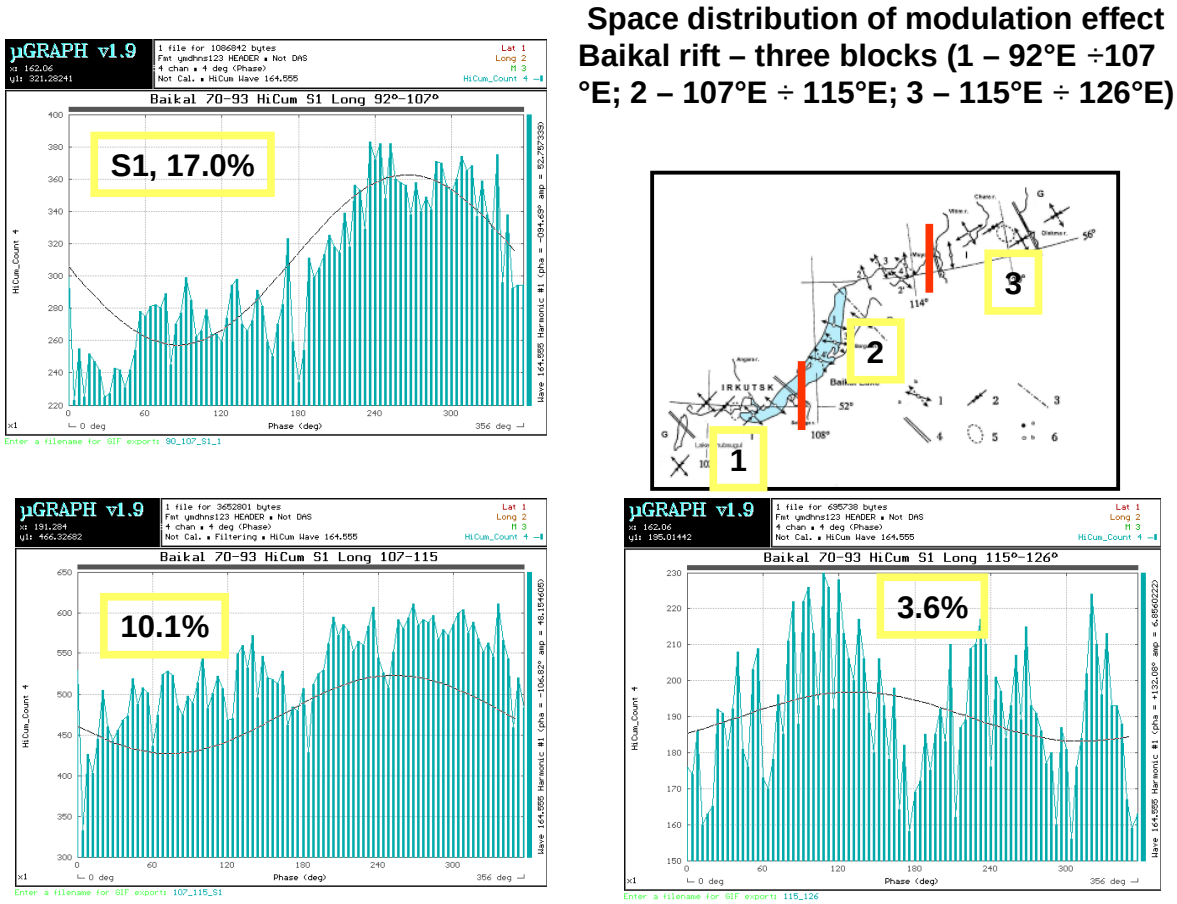

Figure 11. Separation of Baikal rift into three blocks (1 – 92°E ÷107 °E; 2 – 107°E ÷ 115°E; 3 – 115°E ÷ 126°E) based on seismological study [Solonenko, 1993]. Space distribution of modulation for wave S1:: block 1 – 17.0%, block 2 – 10.1%, block 3 – 3.6%.

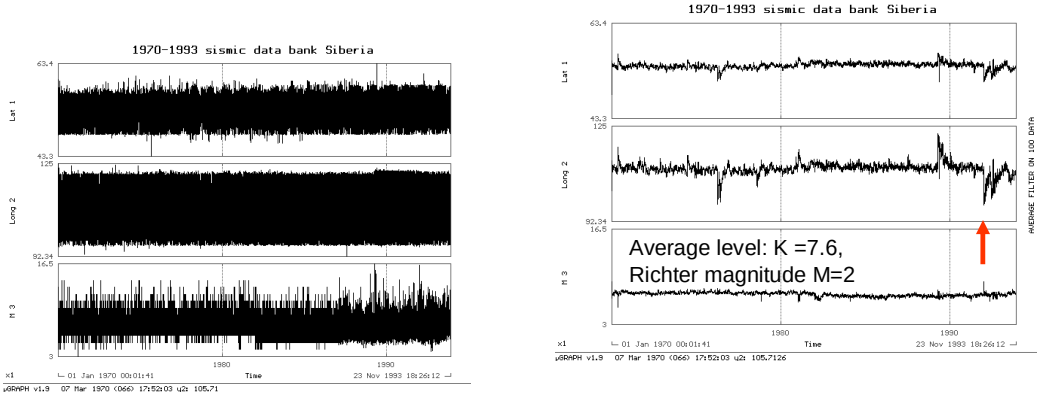

First block - Strong earthquake 27.12.1991, 51.0°N, 98.0°E, M = 6.5 ÷ 7.0. Tested territory 50°N ÷ 52°N and 96.5°E ÷ 99.5°E, 1987-1993 yy.

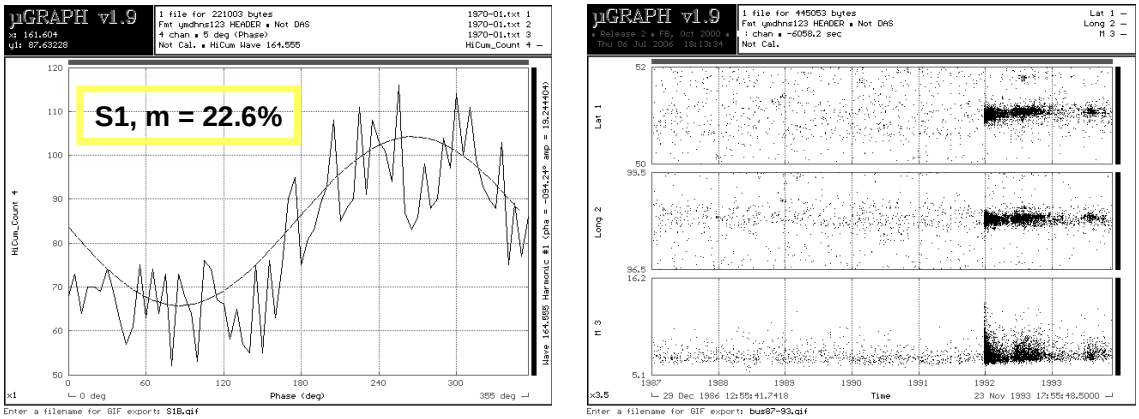

Figure 12. Top) Seismic data bank (φ-λ-K) 1970-1993, raw and smoothed (100); arrow indicates Strong earthquake 27.12.1991, 51.0°N, 98.0°E, M = 6.5 ÷ 7.0.

Bottom) Analysis of 1987-1993 series, tidal modulation (wave S1) , tested territory 50°N ÷ 52°N and 96.5°E ÷ 99.5°E.

Zone of Strong Busingol earthquake 27.12.1991, 51.0°N, 98.0°E,
(Busingol Lake, Mongolia), M = 6.5 ÷ 7.0.
Tested territory: 50°N ÷ 52°N and 96.5°E ÷ 99.5°E, 6.5< K< 8.5.
Modulation for S1 wave, before and after earthquake.

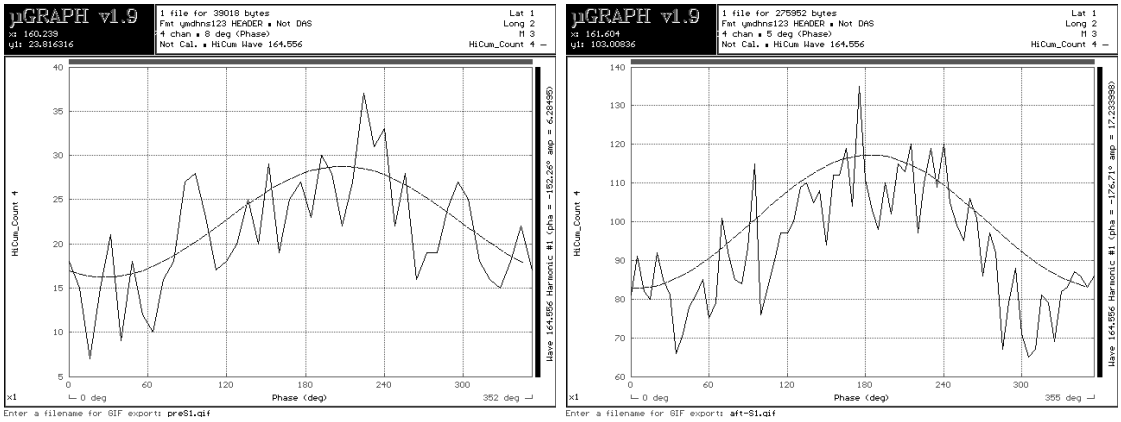

Before (1987-1991) 30.2% and after earthquake (1992-1993) 17.2% .

Figure 13. Zone of Strong Busingol earthquake 27.12.1991, 51.0°N, 98.0°E, (Busingol Lake, Mongolia), M = 6.5 ÷ 7.0. Tested territory: 50°N ÷ 52°N and 96.5°E ÷ 99.5°E, 6.5< K< 8.5. Modulation for S1 wave, before and after earthquake: Before (1987-1991) 30.2% and after earthquake (1992-1993) 17.2% .

Modulation (S1) effect before Busingol earthquake (period 11.1987-12.1991) and after earthquake (periods: 01.1992; 02-04.1992; 05-11.92; 12.1992-11.1993). Changing from 30% to 12% during 6 months after Busingol earthquake.

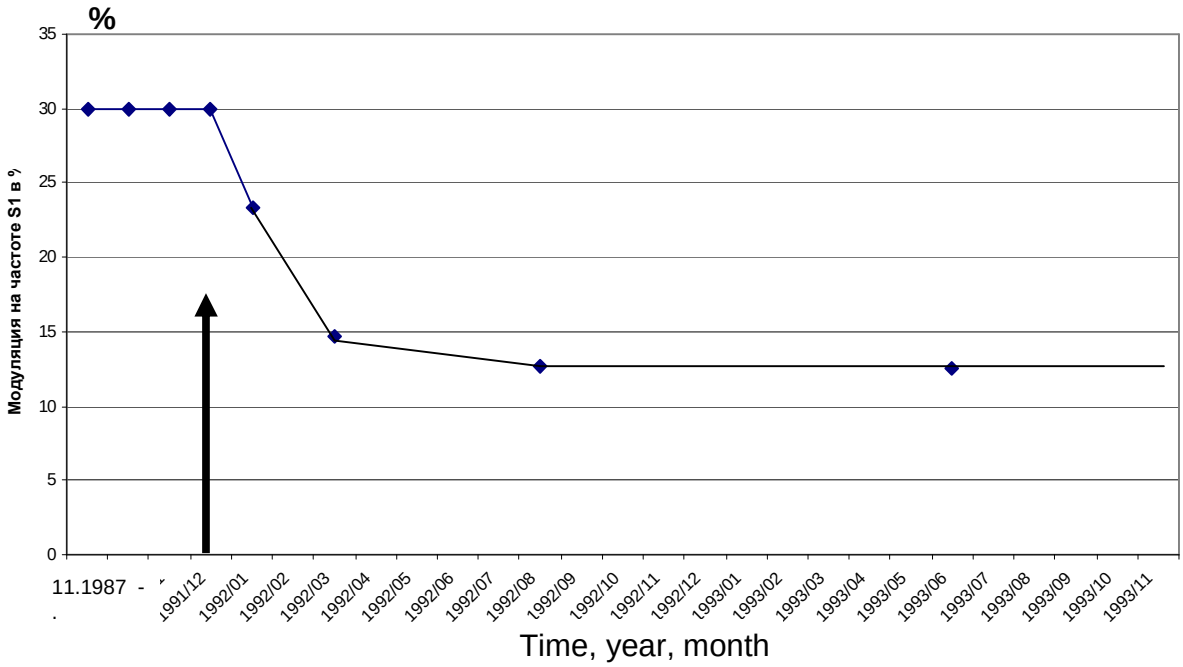

Figure 14. Evolution of S1 modulation before Busingol earthquake (period 11.1987-12.1991) and after earthquake (periods: 01.1992; 02-04.1992; 05-11.92; 12.1992-11.1993). Modulation is changing from 30% to 12% during the 6 months following Busingol earthquake.

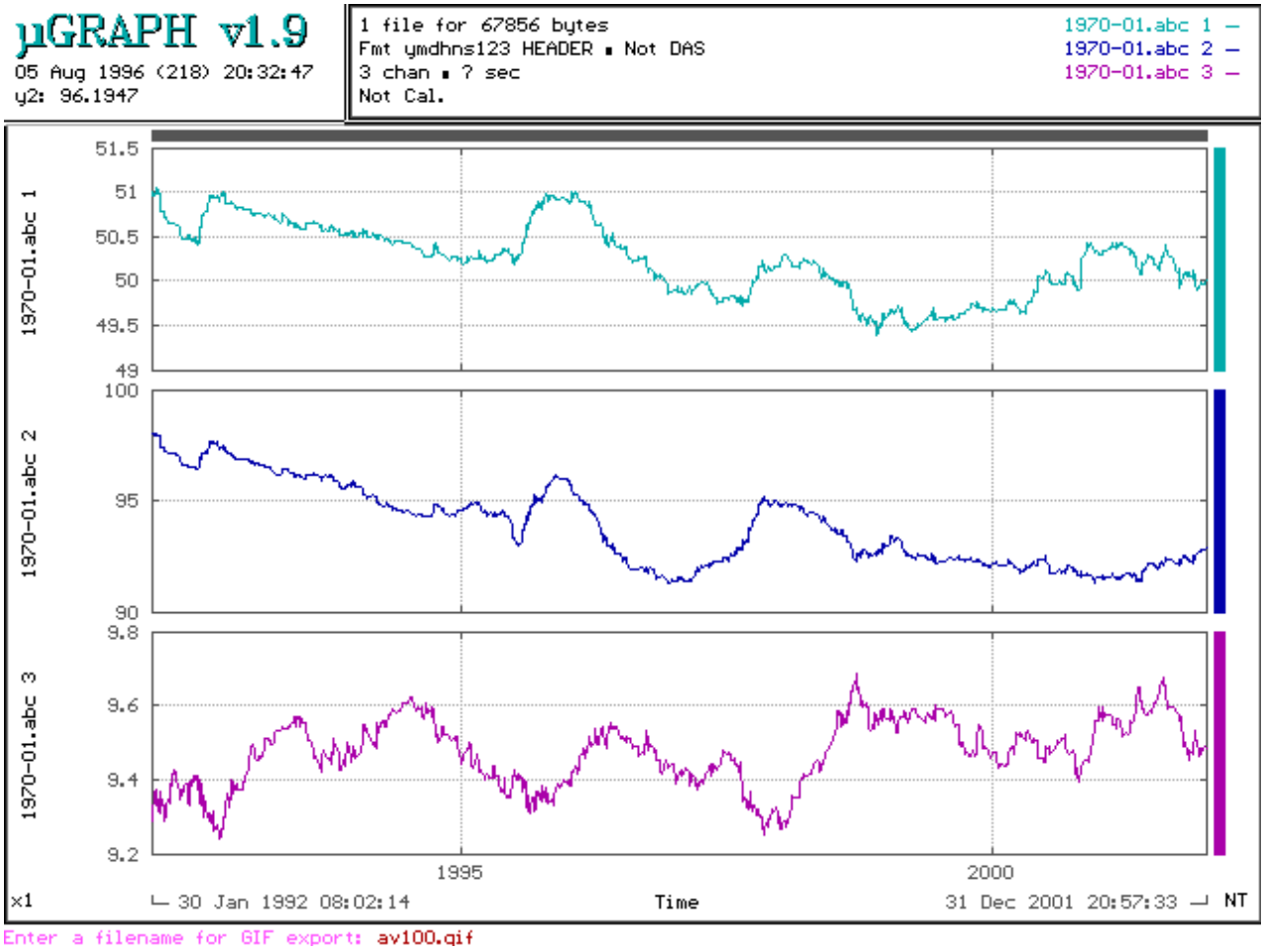

Figure 15. Migration of seismic activity (φ-λ-K) from Busingol earthquake zone (27.12.1991, 51.0°N, 98.0°E, M = 6.5 ÷ 7.0) to Chuya earthquake zone (27.09.2003, 50.0°N, 88.0°E, M = 7.2 ÷ 7.5).

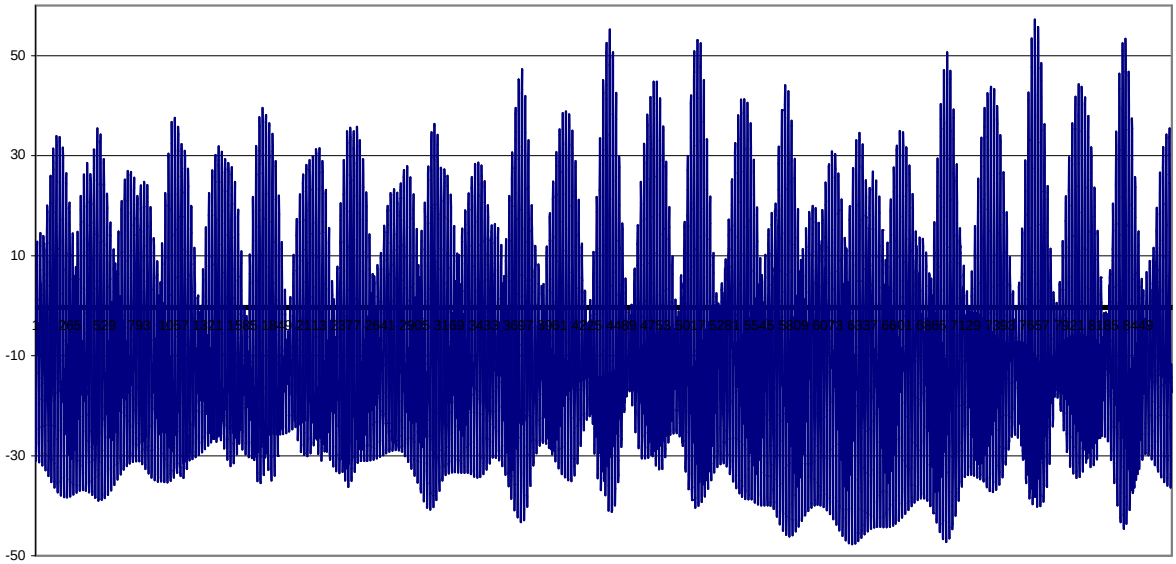

Figure 16. Volume strain for Talaya station (2008 year, in nstr).

Observation of tidal deformations in a tectonically active region of the Northern Caucasus

Vadim K. Milyukov[a*], Alexander V. Kopaev[a], Anna V. Lagutkina[a], Alexey P. Mironov[a], Andrey V. Myasnikov[a], Boris S. Klyachko[a]

[a]Sternberg Astronomical Institute, Moscow State University, Russia.

The results of observations of tidal strains of the crust observed in a mountainous area of the Northern Caucasus near to the volcano Elbrus during the period 2003–08 are presented. Precise crustal strain observations are carried out using the Baksan laser interferometer strainmeter with a measuring arm length of 75 m and resolution of 2.3×10^{-13}. The four-year record is characterized by remarkable annual strain changes of the order of $(1 - 1.5) \times 10^{-6}$ and linear strain accumulation of -3.74×10^{-7} /year. Harmonic analysis, performed with the help of the `ETERNA` software package, reveals temporal variations in the amplitude factors of the main tidal waves M_2 (within 1.02–1.15) and O_1 (within 0.76–1.24). The influence of the topography on tidal strains in the Baksan gorge is estimated at 22% (an increase in the measured strain values). Therefore the reduced amplitude factors of the main diurnal and semidiurnal waves are underestimated. Numerical modeling of tidal anomalies produced by regional heterogeneous inclusions is performed in a *2-D approximation*. The observed anomaly of the M_2 wave (12%) is shown to be due to the influence of the main magma-controlling fault associated with the deep magma source of the Elbrus dormant volcano. The preliminary analysis of the evidence of *the fluid core resonance* (FCR) effect in the diurnal tidal band has been carried out.

Keywords: Earth tides; crustal deformations; volcano structures

1. Introduction

The northern part of the Greater Caucasus is one of the most geodynamically active regions of Russia [11]. From the standpoint of modern geodynamics, this region represents a typical example of collision tectonics, characterized by the accumulation of compressive deformations in the submeridional direction, extension in the sublatitudinal direction, and the continuing overall uplift of the Greater Caucasus mountain system, that is still occurring. This is a zone of complex tectonics associated with the interaction of two of the Earth's major lithospheric plates, Arabia and Eurasia. Therefore, the region as a whole is characterized by a complex system of faults with meridional and diagonal structures.

The Elbrus volcanic center, located on the northern slope of the main range of the Greater Caucasus, is the highest point of Europe. The west top has an altitude of 5643

*Postal address: Sternberg Astronomical Institute of Lomonosov Moscow State University, 13, Universitetskij prospekt, Moscow, 119992, Russia; Phone: (495) 939 1634; Fax: (495) 932 8841; E-mail: milyukov@sai.msu.ru

m and the east top has an altitude of 5620 m. Mount Elbrus is classified as an active volcano with previous historical eruptions clearly dated to the Holocene. Current classifications define Elbrus as a dormant volcano that could become active even after millennia of quiescence [1]. Recent geological–geophysical investigations conducted in the Elbrus region found that a significant volume of low-density substance with a temperature of at least 700°C could exist beneath the volcano at a depth of about 20–30 km. This volume could potentially have been the magma source that supplied the material for previous eruptions of Mount Elbrus [2].

In this unique place for studying geodynamic and volcanic processes, the geodynamic observatory of the Sternberg Astronomical Institute of Moscow University has been created. The Baksan geodynamic observatory is located in the Elbrus area (Baksan gorge) of the Kabardino-Balkaria region 30 km southwest of the town of Tyrnyauz; the distance of the observatory from Elbrus volcano is 18 km. The long-term monitoring of lithosphere deformations of this region is carried out by the long-base laser interferometer–strainmeter.

A horizontal strainmeter oriented at an arbitrary azimuth α measures the following combination of strain components [4]:

$$\varepsilon_{obs} = \varepsilon_{\theta\theta}\cos^2\alpha + \varepsilon_{\varphi\varphi}\sin^2\alpha + \varepsilon_{\theta\varphi}\sin 2\alpha \ , \tag{1}$$

were

$$\begin{aligned}
\varepsilon_{\theta\theta} &= \frac{1}{gr}\left(hW_2 + l\frac{\partial^2 W_2}{\partial\theta^2}\right) \ , \\
\varepsilon_{\varphi\varphi} &= \frac{1}{gr}\left(hW_2 + l\cos\theta\frac{\partial W_2}{\partial\theta} + \frac{l}{\sin^2\theta}\frac{\partial^2 W_2}{\partial\varphi^2}\right) \ , \\
\varepsilon_{\theta\varphi} &= \frac{1}{gr}\left(\frac{l}{\sin\theta}\frac{\partial^2 W_2}{\partial\theta\partial\varphi} - l\frac{\cos\theta}{\sin\theta}\frac{\partial W_2}{\partial\varphi}\right) \ .
\end{aligned} \tag{2}$$

The Love number $h = 0.61$ and the Shida constant $l = 0.08$ are determined from the solution of the problem of the forced oscillations in a spherically symmetric model of an elastic Earth (the preliminary reference Earth model [3]) under the action of the lunisolar potential W_2; g is the gravity at the Earth's surface.

It is well known that the observed amplitudes of tidal strains can differ significantly from theoretical amplitudes calculated for the accepted model of the Earth. These anomalies are mainly controlled by the structure and elastic characteristics of the crust and upper mantle, in particular by the presence of deep faults or other heterogeneous inclusions near observation points, as well as by the topography, especially in mountainous areas. The role of such heterogeneous inclusions can be played, in particular, by the magmatic structures of the volcano Elbrus.

This study presents the results of long-term tidal strain observations made with the Baksan laser interferometer strainmeter. The observed amplitude anomaly of the tidal wave M_2 is interpreted in the framework of the existence of regional low-density inclusions which can be associated with the magmatic structure of the volcano Elbrus. Finally, we use the whole data to estimate the effect of *the fluid core resonance* (FCR) on the amplitudes of diurnal tidal harmonics.

2. Baksan laser interferometer

The Baksan laser interferometer is a Michelson two-beam unequal-arm interferometer operating in the regime of separated beams. The length of its larger (measuring) arm is L = 75 m (accordingly, its optical length is 150 m), and the length of the minor (reference) arm is 0.3 m. The optical elements of the interferometer are mounted in two cylindrical vacuum chambers whose lower parts are built into pedestals. The supporting pedestals of the interferometer are concrete pillars deepened to 1.5 m, rigidly connected with bedrock, and protruding beyond the lower level of the gallery for 30 cm. The chambers are connected to each other by three bellows and vacuum tubes 30 cm in diameter that form a light guide (Fig. 1). In a stationary regime, the pressure in the system is 10^{-2} Pa. An electronic recording system ensures operation of the interferometer in a wide range of frequencies, from ultralow (limited only by the time interval of continuous observations) to thousands of hertz. In a standard regime, the lithospheric strains are monitored by five frequency channels. The instrumental resolution of the interferometer is 2.3×10^{-13} for crustal strain measurement. The design and technical layout of the Baksan interferometer are described in detail in [6] and [5].

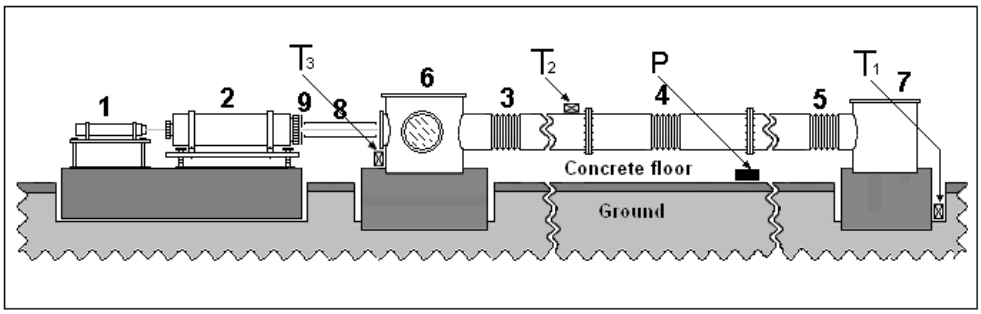

Figure 1. General scheme of the Baksan laser interferometer and the position of monitoring sensors: (1, 2, 8, 9) laser, telescopic system and light guide; (3, 4, 5) bellows; (6, 7) vacuum chambers; (T_1, T_2, T_3) temperature sensors; (P) pressure gauge.

The interferometer is mounted at a level of 650 m and a depth of 400 m inside the main gallery of the Baksan Neutrino Observatory, Institute of Nuclear Research (INR), Russian Academy of Sciences (RAS). The coordinates of the interferometer are (43°12′N, 42°43′E), and its azimuth is 150°37′. The temperature of the interferometer units and environment is monitored by three sensors with a resolution of 0.005°C. The sensors T_1, T_2, and T_3 (Fig. 1) are installed on the concrete basement below the gallery floor level, on the light guide surface, and in the lower part of the vacuum chamber, respectively. The atmospheric pressure is recorded by the gauge P of the membrane type with a resolution of 2.7 mPa. The pressure inside the interferometer is monitored by a vacuum electric-discharge magnetic gauge.

3. Observations and data analysis

Long-term monitoring of the crustal deformation is being carried out over a period of ten years. The results of four years observations of hourly variations in strains, "rock" temperature (T_1 sensor), and atmospheric pressure are shown in Fig. 2. Thirty day running means are superposed on the temperature and pressure curves. The increase in temperature is displayed downward. As shown in Fig. 2, the strain record is characterized by remarkable annual changes of the order of $(1-1.5)\times10^{-6}$ and linear strain accumulation of -3.74×10^{-7} /year. The annual strain changes are inversely proportional to "rock" temperature changes.

a)

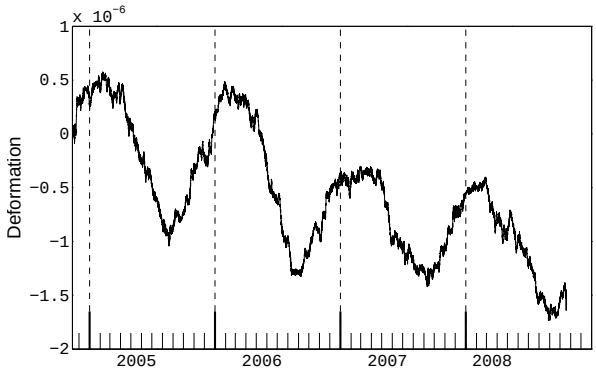

b)

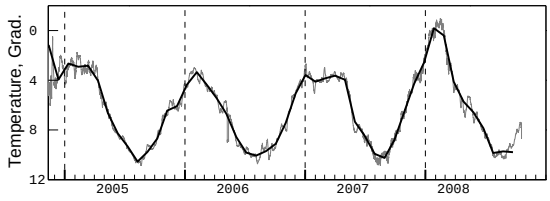

c)

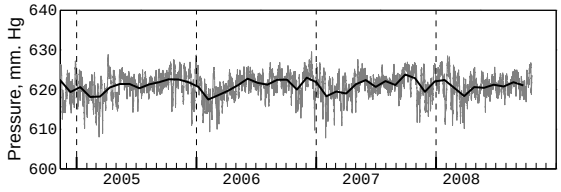

Figure 2. Observational results of strain (a), "rock" temperature (b) and atmospheric pressure (c) changes during the period from November 2004 to October 2008 (the temperature scale is inverted).

Records of crustal strains, atmospheric pressure, and temperature variations during the period 2003–08 were used for harmonic analysis. The data are represented as two periods of continuous observations: September 2003 – May 2004 and November 2004 – August 2008. The periods were divided into 53 monthly segments. An example of observed monthly data filtered in tidal frequency band is shown in Fig. 3. The diurnal and semidiurnal groups of tidal waves revealed by the Fourier analysis of all data are shown in Fig. 4.

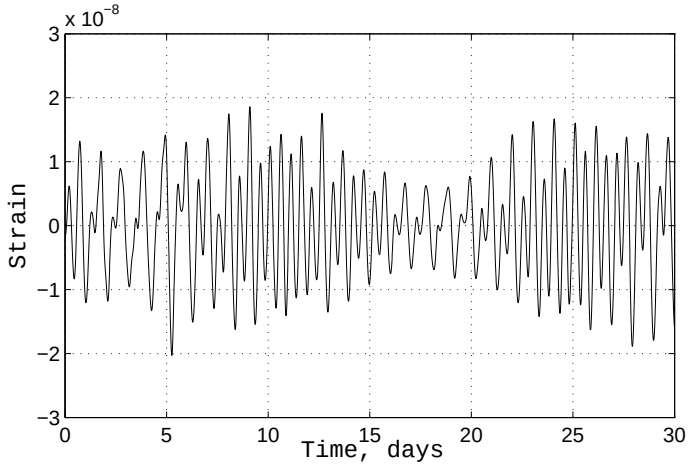

Figure 3. One month observed tidal data.

Harmonic analysis of a one-month series of observations was performed with the use of the ETERNA software package. The decomposition included eleven groups of tidal harmonics: six in the diurnal range (Q_1, O_1, NO_1, $P_1S_1K_1$, J_1, OO_1) and five in the semidiurnal range ($2N_2$, N_2, M_2, L_2, S_2K_2). The waves P_1, S_1 and K_1 and the waves S_2 and K_2 are united in two groups because they cannot be determined separately from one-month intervals of observations. ETERNA allows the calculation of the regression of strain data for various meteorological parameters. The temperature regression was calculated for each of the three temperature channels. We examined the dependence of the calculated results on the temperature channel used. The signal-to-noise ratio for the main tidal waves M_2 and O_1 was a criterion of the efficiency of compensation for the temperature dependence. The largest values of the signal-to-noise ratio are obtained for data for the channel T_2, reflecting well the diurnal temperature variations.

The results of monthly harmonic analysis of the tidal waves O_1 and M_2 are presented next (Fig. 5). The signal-to-noise ratios for the main lunar diurnal wave O_1 vary from 15 to 70 (on average, 30). The determination uncertainty of the amplitude factor is 2–5%. The main lunar semidiurnal wave M_2 has a signal-to-noise ratio within the range 70–280 (on average, 150). The determination uncertainty of the amplitude factor is 0.4–1%. The lower signal-to-noise ratio for the O_1 wave is evidently due to the presence of a residual

a) **b)**

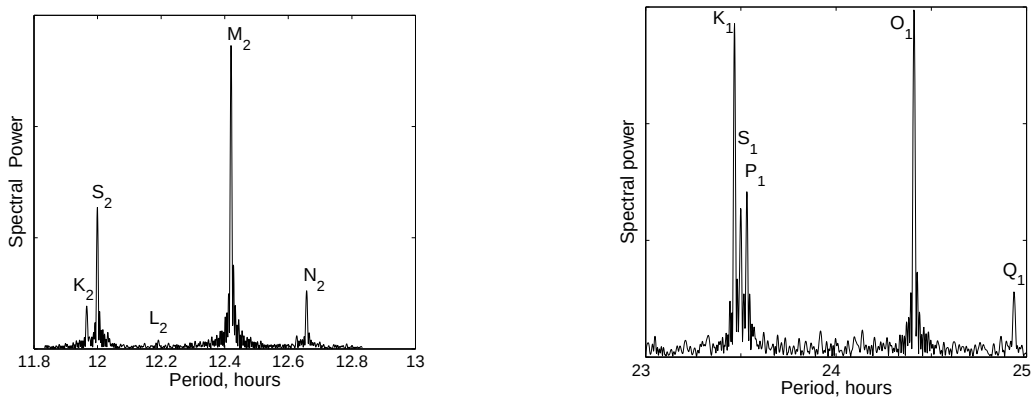

Figure 4. Spectra of (a) the semidiurnal and (b) diurnal groups of tidal waves.

a)

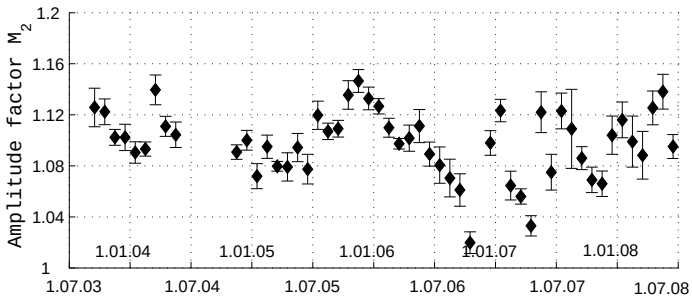

b)

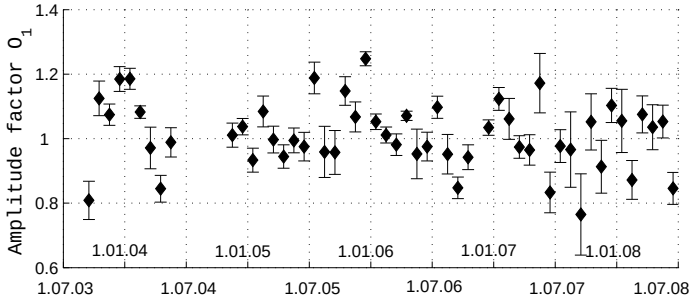

Figure 5. Amplitude factors for the tidal waves (a) M_2 and (b) O_1, calculated for monthly data. The vertical bars are rms deviation ranges.

correlated noise in the diurnal frequency range. In contrast, the M_2 wave, whose period differs significantly from both the nearest tidal components, N_2, L_2, S_2, and K_2 and from the average solar day, has a high signal-to-noise ratio and is therefore a main amplitude-phase indicator of the elastic response of the crust to the tidal action. The phase delay of the O_1 wave varies from $-5°$ to $+5°$ (the average over all time intervals is $-1.3°$). The determination uncertainty of the phase delay is $1°$ to $3°$. A quite stable phase delay for the M_2 wave varying from $0°$ to $1°$ (an average of $0.1°$) with a determination uncertainty of the order of $0.5°$ points to the absence of any systematic effects and to stable operation of the instrument. No appreciable seasonal variations are noted either.

The topography of the area in the immediate vicinity of the observation point appreciably distorts tidal strains. The effect of the topography on the amplitudes and phases of tidal tilts and strains was estimated by the perturbation method of a small parameter [9,10]. Using this method, the topography of the Baksan gorge was approximated by the 8th order polynomial (Fig. 6). The Baksan laser interferometer is located at a depth of about 400 m and is oriented along the axis perpendicular to the gorge. The direct calculation of perturbations associated with the effects of topography and the position of the interferometer yields a relative strain anomaly equal to +0.22. Thus, the topography effect increases the measured strain values by 22%.

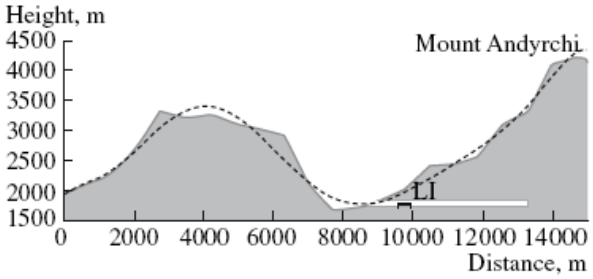

Figure 6. Approximation of the Baksan gorge topography along the cross section of the main gallery of the Baksan Neutrino Observatory (INR RAS) by a polynomial of degree 8. The position of the laser interferometer (LI) is shown.

4. Discussion of results of observation

Analysis reveals statistically significant temporal variations in the amplitude factors of the wave M_2 , while for the O_1 wave they are only scattered in time. The values of this factor lie within the range 1.02–1.15 (on average, 1.10) for M_2 and 0.76–1.24 (on average, 1.01) for O_1. In accordance with the estimated topography effect, we have to reduce the estimates of amplitude factors for the M_2 and O_1 waves by 22%. Therefore the mean values of the amplitude factors are 0.88 for M_2 and 0.81 for O_1. On the whole, the amplitude factors of the main diurnal and semidiurnal tidal waves are underestimated.

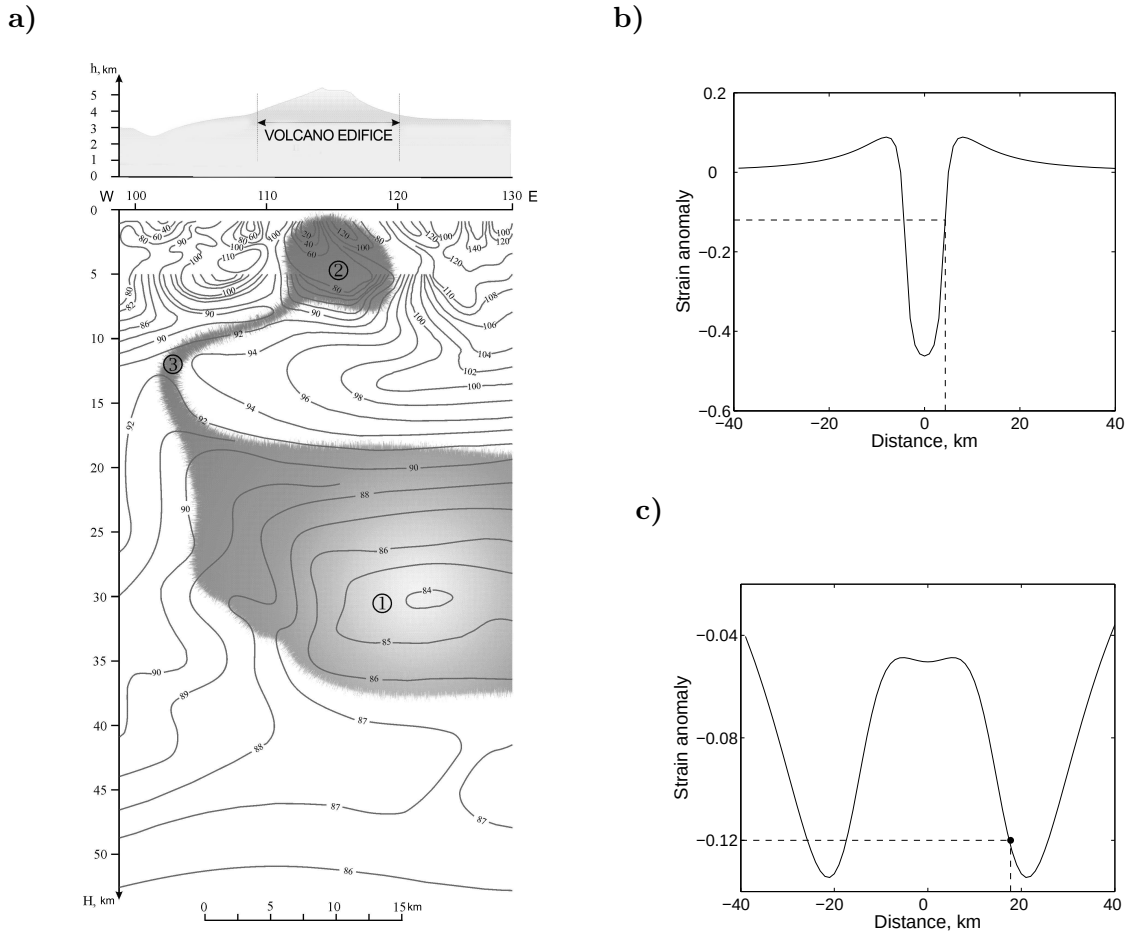

Figure 7. Influence of Elbrus magmatic structures on tidal strain amplitude: (a) Elbrus Volcano and its volcanic chambers from data on the tectonic fragmentation field [2]: (1) potential magma source; (2) shallow magma chamber; (3) a possible channel of primary magma flow. (b) and (c) the results of numerical modeling of anomalous effects of the magma chamber (b) and magma source (c).

Thus, the M_2 and O_1 anomalies of tidal strains average 12 and 19%, respectively. Since the topography effect is compensated, the observed anomalies are apparently associated with the presence of a large regional heterogeneous inclusion. The influence of such an inclusion can be estimated by analogy with the topography effect [9].

The nearest tectonic fault extends for 5 km from the Baksan laser interferometer station in the N–W direction, that is, almost parallel to an interferometer arm [7]. The anomalous strain caused by this fault is negligible. The magmatic structures of the Elbrus volcano can play the role of large regional heterogeneous inclusions because the Baksan laser interferometer is located at a distance of 18 km from its peaks. Modern technologies for processing space images of the Earth's surface identify near the Elbrus volcanic center two areas of anomalously low values of the tectonic fragmentation field of the lithosphere that are interpreted as a potential magma source and chamber of the Elbrus volcano [2]. The Elbrus magma chamber is located exactly beneath its volcanic edifice at depths from 1 to 8 km. The chamber width attains 9 km. The other tectonically weakened zone interpreted as a magma source is traceable from depths of 40–45 km up to 15–17 km (Fig. 7a). Results of the observations and analysis of regional resonance modes also reveal a shallow magma chamber in the structure of the Elbrus volcano [8].

Using a method proposed by Molodensky [9], we calculated anomalies of M_2 tidal strains in the vicinity of a soft inclusion in the shape of an infinite (along the horizontal Y axis) rectangular parallelepiped similar in cross-section dimensions and occurrence depth to the magma chamber and source. The results of numerical modeling are presented in Fig. 7b (chamber) and Fig. 7c (source). The anomalous effect of the magma chamber becomes rapidly weaker with distance from the volcano center and becomes negligible at a distance of 18 km (at the observation point); a tidal anomaly of 12% will be observed at a distance of 4.3 km. The tidal anomaly associated with the deep source varies with distance according to a more complex law and attains a value of 12% at distances of 18 km (at the observation point) and 26 km from the volcano center. Thus, the observed tidal strain anomaly is apparently due to the influence of the Elbrus deep magma source.

5. Estimation of the fluid core resonance effect

Free core nutation of the Earth causes the fluid core resonance (FCR) at the frequency of 1.0023 *cycles per sideral day*, which leads to disturbances of the tidal waves in the diurnal band. The FCR effect should deform essentially the amplitudes of tidal waves in a range of frequencies from 14.9 degree/h to 15.15 degree/h, that is, the waves K_1, Ψ_1 Φ_1. We have performed the preliminary analysis to estimate the influence of the FCR on the amplitudes of diurnal tidal harmonics. Three data sets were used from 2000 to 2007. The data were represented as 40 monthly segments. The analysis was done using `ETERNA` software, and the decomposition included 17 groups of waves: ten waves in the diurnal band (Q_1, O_1, NO_1, P_1, S_1, K_1, Ψ_1, Φ_1, J_1, OO_1), six waves in the semidiurnal band ($2N_2$, N_2, M_2, L_2, S_2, K_2), and the third diurnal wave M_3. The preliminary analysis also included correction of the strain data on three temperature channels, which was carried out using the program `TSOFT`. The results of the analysis are shown in Table 1. The analysis clearly reveals lunisolar declination wave K_1, for which the signal-to-noise ratio is more than 50. It is considered that all meteorological effects distort the diurnal

Table 1
Computed parameters of tidal waves according to 2002–07 strain data.

Wave	Ampl., nstr	Ampl. fac.	STDV	Phase Lead	STDV, (deg)
Q_1	0.958	0.9604	0.1227	0.01	7.32
O_1	5.362	1.0293	0.0235	-1.53	1.3
NO_1	0.452	1.1031	0.2987	4.69	15.51
P_1	2.228	0.9193	0.0504	-24.3	3.14
S_1	2.14	37.3351	2.1349	-4.68	3.27
K_1	6.213	0.8481	0.0167	-10.4	1.12
Ψ_1	0.159	2.7792	2.135	129.11	44.01
Φ_1	0.181	1.7306	1.1731	85.65	38.83
J_1	0.403	0.9831	0.2987	-12.13	17.41
OO_1	0.176	0.7867	0.5459	-9.01	39.75
$2N_2$	0.339	1.0518	0.1123	-7.03	6.12
N_2	2.19	1.0847	0.0179	0.82	0.94
M_2	11.553	1.0955	0.0034	-0.04	0.18
L_2	0.323	1.0849	0.1215	-4.84	6.42
S_2	5.226	1.0653	0.0073	0.95	0.39
K_2	1.438	1.0783	0.0271	1.65	1.44
M_3	0.065	1.1596	0.3145	14.57	15.541

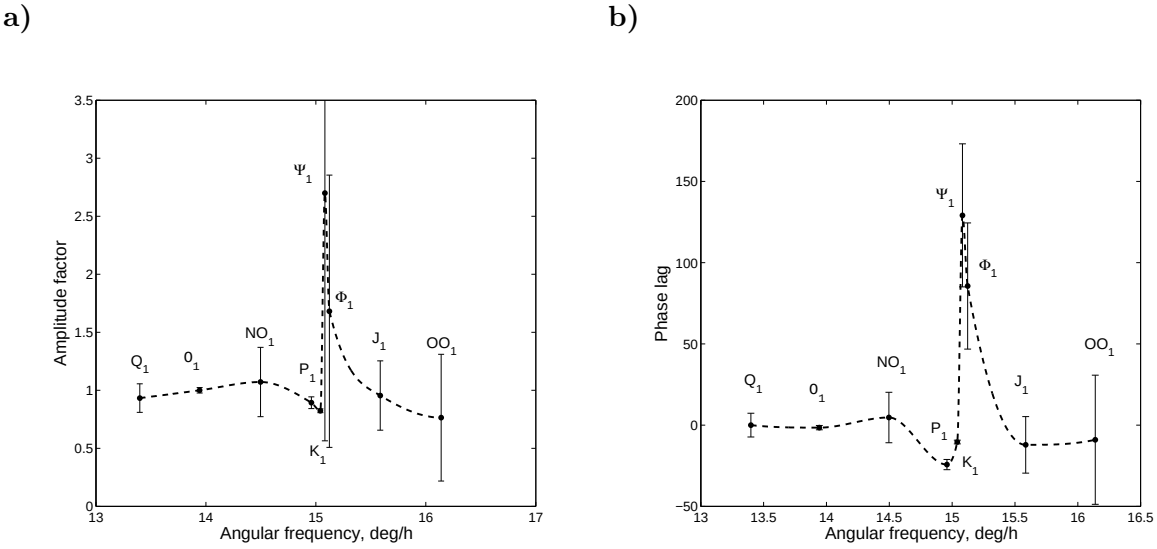

Figure 8. Fluid core resonance effect in the diurnal tidal band. Estimated amplitude factors (a) and phase lag (b) of the diurnal tidal constituents. Bars indicate *rms* errors.

constituents in the same way. To estimate the FCR effect, the wave O_1, which is far from resonance, is chosen as reference for near-resonance constituents. The amplitudes for K_1, Ψ_1 and Φ_1 constituents are 82%, 270%, and 168% of the amplitudes free from the FCR effect, respectively. The computed phase lags for these waves are $-10°$, $129°$, and $85°$, respectively. As it follows from the Table 1 the wave S_1 is very perturbed (the amplitude factor is 37). The minor constituents of the diurnal tidal bands, Ψ_1, and Φ_1, being harmonics of S_1, are obviously affected by S_1, that is expressed in the very large phase lags observed on Ψ_1, and Φ_1. Accuracies of the amplitude and phase estimations for these minor waves are very low. Fig. 8 demonstrates the influence of the FCR effect on the diurnal harmonics of tidal waves.

6. Conclusion

The principal finding of this study is the considerable anomalies in tidal wave amplitudes which are observed in the mountain area of the Northern Caucasus, near to the volcano Elbrus, one of the most geodynamically active regions of Russia. This result is based on long-term regular observations of tidal strains which were performed with the use of the Baksan laser interferometer strainmeter with a measuring arm length of 75 m mounted at a depth of 400 m below the Earth's surface. The data from 2003 to 2008 were used for the tidal harmonic analysis which was carried out using the `ETERNA` software package. The main semidiurnal wave M_2 is most reliably resolved by the analysis. For the one-month observation intervals, this tidal harmonic has a signal-to-noise ratio within the range 100–170 (280 at the most). The determination uncertainty of the amplitude factor is 0.5–1%. Thus, the M_2 wave is a main amplitude-phase indicator of the elastic response of the crust to the tidal action.

The topography of the area in the immediate vicinity of the observation point can appreciably distort tidal strain values. It is particularly important to take into account the topography in a mountainous area; in particular, inclination angles of the Baksan gorge profile attain 30–35°. The topography of the Baksan gorge at the location of the laser interferometer was approximated by a polynomial of degree 8. Direct calculations of tidal strain perturbations due to the topography effect yield a strain value of +0.22, which is larger than the measured strain values by 22%.

On the whole, the reduced amplitude factors of tidal waves are underestimated. The tidal strain anomaly averages 12% for M_2 and 19% for O_1. Tectonic faults and Elbrus magmatic structures can play the role of large regional heterogeneous inclusions distorting tidal strains. The nearest fault extends at a distance of 5 km from the location of the Baksan laser interferometer and is nearly parallel to its sensitive arm. However, the anomaly caused by this fault is negligible. In contrast, mathematical modeling of the anomalous effect caused by the magma source of Elbrus volcano shows that this effect can be appreciable. The tidal anomaly attains 12% at a distance of 18 km from the volcano center (at the observation point). Apparently we may suggest that the observed tidal strain anomaly is due to the influence of the deep magma source of the Elbrus volcano.

The existence of long-term observations allowed us to also estimate the FCR effect. This analysis is based on the data from 2000 to 2007. The computed amplitudes for

K_1, Ψ_1 and Φ_1 constituents are 82%, 270%, and 168% of the amplitudes free from the FCR effect, respectively. The FCR effect analysis is considered to be a preliminary one. We hope to improve the estimation of near-resonance constituents and to estimate the parameters of free core nutation of the Earth in a future study.

7. Acknowledgments

This work was supported by the *Russian Foundation for Basic Research*, project No.07-05-13573-ofi_c and No.07-05-00786-a.

REFERENCES

1. Bogatikov, O.A., Nechaev, Yu.V., Sobisevich, A.L., 2002a. The use of cosmic technologies for the monitoring of geological structures of Elbrus volcano. Dokl. Akad. Nauk. 387 (3), 364–369.
2. Bogatikov, O.A., Gurbanov, A.G., Rogozhin, E.A., et al., 2002b. Activation of Elbrus volcano and its possible consequences. In: Catastrophic processes and their implications for the environment, vol. 1: Volcanism, IFZ RAN, Moscow, 346–397.
3. Dziewonski, A.M., Anderson, D.L., 1981. Preliminary reference Earth model. Phys. Earth Planet. Int. 25, 297–356.
4. Melchior P., 1966. The Earth Tides. Pergamon Press, Oxford.
5. Milyukov, V.K., Klyachko, B.S., Myasnikov, A.V., Striganov, P.S., Yanin, A.F., Vlasov, A.N., 2005. A laser interferometer - deformograph for monitoring the crust movement. Instr. Exp. Techniques. 48 (6), 780–795.
6. Milyukov, V.K., Myasnikov, A.V., 2005. Metrological characteristics of the Baksan laser interferometer. Izmerit. Tekhnika. No. 12, 26–30.
7. Kopaev, A., Milyukov, V., 2002. Environmental effects in tide strain observations near the mt. Elbrus, Central Caucasus. Marees Terrestres. Bull. d'Inform. 137, 10909–10916.
8. Milyukov, V.K., 2006. Monitoring of the state of Elbrus magmatic structures using lithospheric strain observations. Vulkanol. Seismol. No. 1, 3–15.
9. Molodensky, S.M., 1983. Determination of tidal strain perturbations for a plain topography. Izv. AN SSSR, Ser.Fiz. Zemli, No. 7, 80–96.
10. Molodensky, S.M., 1986. The plain topography implications for tidal tilts and strains: effects of second order. Izv. Akad. Nauk SSSR, Ser. Fiz. Zemli, No. 8, 3–14.
11. Rogozhin, E.A., Sobisevich, L.E., Nechaev, Yu.V., et al., Geodynamics, Seismotectonics, and Volcanism of the Northern Caucasus. 2001. IFZ RAN, Moscow.

Validation of GRACE Data Using GGP stations from Europe and Asia

David Crossley[(1)], Caroline de Linage[(2)], Jean-Paul Boy[(2)], and Jacques Hinderer[(2)], and Junyong Chang[(1)]

[(1)] Department of Earth and Atmospheric Sciences, St. Louis University, 3507 Laclede Ave., St. Louis, MO, USA 63103 (crossleydj@gmail.com),
[(2)]Ecole et Observatoire des Sciences de la Terre / IPG Strasbourg, 5 Rue Descartes, Strasbourg 67084 Cedex, France (Jacques.Hinderer@eost.u-strasbg.fr).

Abstract
We consider the validation of GRACE satellite data by ground gravimetry from the Global Geodynamics Project (GGP). Results are presented for central Europe, where 7 superconducting gravimeter stations have been operating through the period of GRACE (mid 2002 to present); our comparison extends previous results to the end of 2006. While the overall agreement between GGP and GRACE is consistent with the seasonal hydrology predicted by GLDAS model, many features in the gravity data differ in amplitude and phase. Using EOF decomposition, the amplitude of GLDAS is generally higher than GRACE, and much higher than the ground GGP signal. This is partly due to processing, but a major factor for the GGP data is the location of stations under the soil moisture horizon. This complicates the comparison with GRACE data. We also for the first time consider the small network of GGP stations in the Japan-Korea-China-Taiwan area, and find that the GRACE seasonal effect is complex. Good correlation between GLDAS and GGP exists for some stations, in particular Wuhan and Matsushiro, but again the phase inversion is apparent. It is clear that problems introduced by the coastlines in this part of the world will make validation even more difficult than in Europe.

Keywords: Superconducting gravimeter, GRACE, hydrology, GGP, GLDAS

Introduction
To readers of BIM, the topic of ground validation of GRACE data is no doubt familiar. Some recent papers include Crossley (2004), Crossley et al. (2004), Crossley et al. (2005), Andersen et al. (2005), Andersen and Hinderer (2005), Hinderer et al. (2006), and Crossley et al. (2007a, 2007b). GRACE satellite gravity data has been used extensively for estimating the variability of continental hydrology, especially in locations of high rainfall, but also in areas such as the US Midwest where ground hydrology is well observed (Swenson et al., 2006). The data has also been compared to the ground deformation produced by the Sumatra-Andaman earthquake of 2004 (e.g. Lambotte et al., 2006; Han et al., 2006; Panet et al., 2007). In both instances, evidence has shown that the satellite gravity field is consistent with the predicted models, based on global land assimilation models and observed ground soil moisture in the first case, and on seismic observations in the other. Yet in neither case has the same type of data been compared, i.e. surface gravity data derived from GRACE with gravity observations on the ground.

Given the size of the anticipated signal (typically a few microgal), the only instrument that is reliable at the microgal level is the superconducting gravimeter (SG), which is the main

instrument of the GGP network. Unlike other studies of the two gravity data sets, we choose not to do a station-by-station comparison between GRACE and GGP data because we believe the satellite data cannot be compared directly to point measurements on the ground. Our approach has been to combine the data from several SGs that cover an area that is comparable to the highest resolution satellite projections on the ground (about 500 km). The technique is a principal component analysis, equivalent to the use of empirical orthogonal functions (EOFs) for time varying spatial data.

In this paper we summarize the result from the European array and compare the different GRACE solutions with the GLDAS hydrology and the GGP data. A more extended paper that includes data to the end of 2007 is being prepared for publication elsewhere. In addition, we here take a look at the possibilities for using the SGs in NE Asia, as they are the only group outside Europe that could be used as an array for comparison with GRACE data - all other SG stations are too isolated for such a purpose.

GGP Data

The data is the same as used previously, that is the ICET GGP database 1 minute data, uncorrected (code '00'), but extended here to the end of 2006. There are 7 SGs located in central Europe: Bad Homburg (BH) near Frankfurt in Germany, Membach (MB) east of Brussels, Medicina (MC) in Italy and south of the Alps, Moxa (MO) near Jena, Germany, Strasbourg (ST) in eastern France, Vienna (VI) which has now stopped recording, and Wettzell (WE) in eastern Germany, a major fiducial geodetic station. These are shown in Figure 1, together with the grid area used for all the comparisons. As can be seen, the GRACE footprint of 500 km is comparable to the average station spacing, but the small number of SG sites even in Europe does little to properly average the regional hydrology.

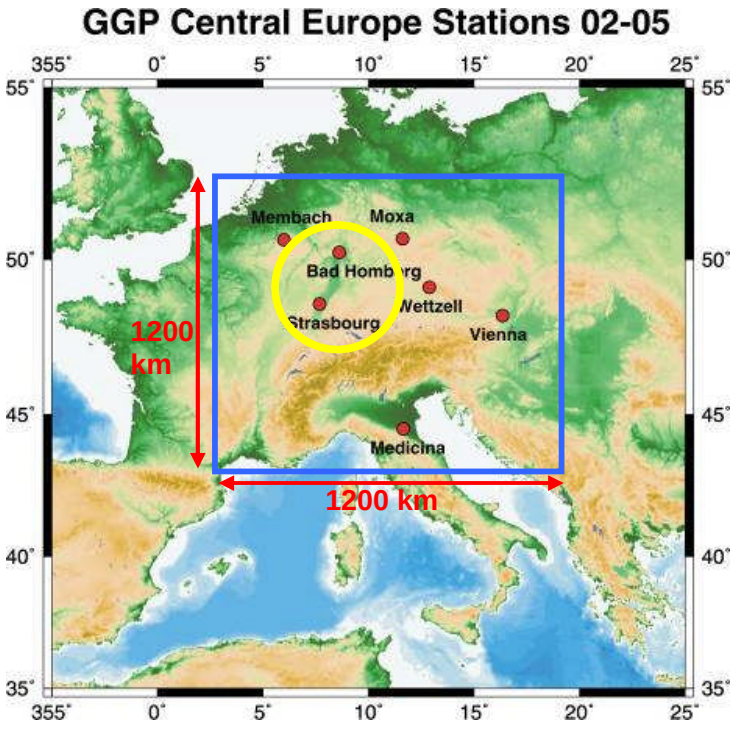

Figure 1. GGP stations recording during the GRACE satellite mission. The blue rectangle is the area for gridding and the yellow circle is about 500km, a typical ground resolution for GRACE.

The processing of the SG data is standard. We subtract a local synthetic tide, including ocean tide loading, local atmospheric pressure with a 2-D global correction for a nominal vertical temperature distribution, and remove IERS polar motion. The residual series has offsets and disturbances that must be removed; this we do with the consultation of the various station operators to ensure that the offsets are not geophysical in origin (e.g. rapid hydrology changes). The

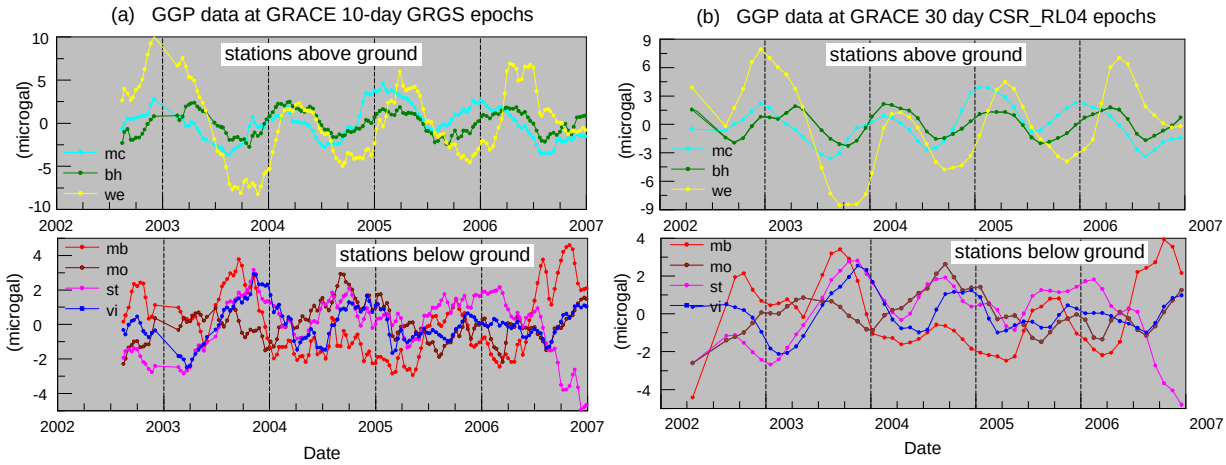

Figure 2. GGP data resampled to: (a) GRGS, and (b) CSR epochs as for the GRACE solutions. The stations are separated according to the location of the soil moisture level.

algorithm for correcting offsets includes an estimate of a linear trend to allow for data gaps during which a trend needs to be continued. After decimation to 1 day samples, the GGP data is resampled to the time periods of the GRACE data, which is about 30 days for the CSR and GFZ solutions, and 10 days for the GRGS solutions (see below). The series are then separated according to whether the SG is located at ground level (the local soil moisture), or below the surface, as shown in Fig. 2. Note that stations above ground level show simultaneous high readings in winter, but low values in summer, even though they may different somewhat in the phase (by up to a month). The 4 stations below the soil moisture level show more complex behavior, but predominantly they have a reversed phase (or sign); this is best seen in the 30-day smoothing (Fig. 2b). Station Moxa is the most complex, as is well known from many other studies. Note that the Strasbourg and Membach gravity diverge notably toward the end of 2006.

The SG series are interpolated to a grid of 65 x 49 cells, spacing 0.25°, using a robust minimum curvature algorithm. Then we perform an EOF decomposition of the spatial data on the grid at each time sample point (GRGS or CSR) and extract the top eigenvalues and their associated eigenvectors. This is a technique that allows the predominant temporal and spatial information to be quantified in the most efficient way and effectively combines the SG data over the map area for comparison with GRACE.

GRACE Data

Again we used the CSR (Texas) and GFZ (Potsdam) GRACE solutions, in Release 04 version, from mid 2002 until the end of 2006, as well as the GRGS (Toulouse) 10-day solutions. The latter are not just a 10-day coefficient solution, but to reduce noise each nominal sample is obtained from running sum of 3 raw 10-day solutions, with weights (1,2,1) indicating double weight for the central time. The mean value of the data (reference level) has been removed, and we note also the degree 2 component has been treated differently according to each data source. No temporal trend was removed from the GRACE data.

To match the effective filtering of the GRGS solutions, the ground level data from GRACE was computed with a cosine taper between degrees 20 and 40, as tapering between degrees 30 and 50 left too much noise in the data. This is designated for example as CSR24. A second solution was

computed using a Gaussian weighting function of the spherical harmonic coefficients. We used 350 km as the more useful radius, whereas previously we had tried 500 km and found the surface field to be too smooth for this area. Solutions are designated for example as GFZ350. The gravity field is computed using the radial derivative of the potential at the surface, but we did not here correct for the effect of vertical station displacement which requires an additional loading factor in the computation of GRACE gravity. Recent calculations suggest that a multiplicative factor of about 1.32 should be applied to the satellite gravity to make the appropriate comparison between GRACE, GGP and hydrology, as done by Neumeyer et al. (2006) and de Linage et al. (2008).

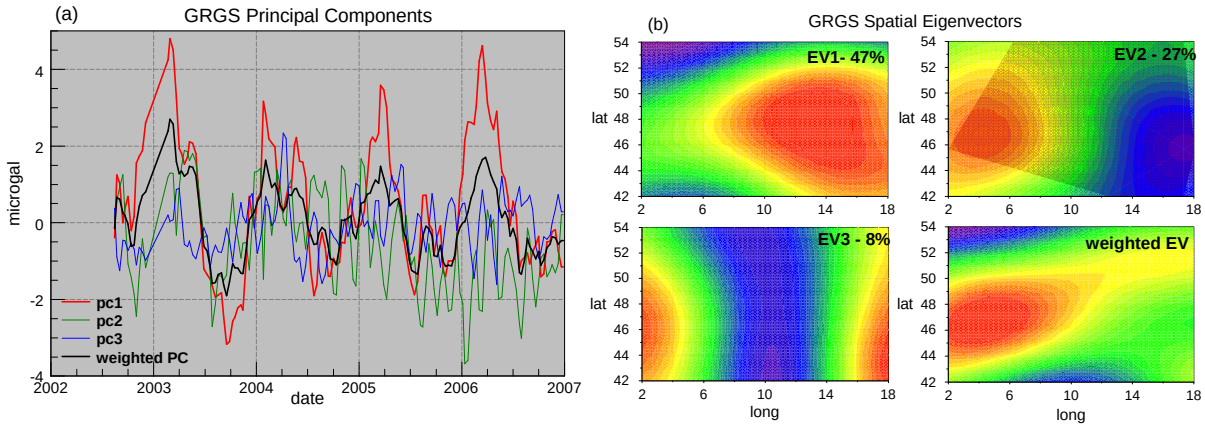

Figure 3. EOF decomposition of the GRGS GRACE field 2002-2006: (a) the first 3 principal components, and (b) the corresponding eigenvectors and variance reduction. The weighed solutions are described in the text.

Figure 3 shows the first 3 eigenmodes of the GRGS field for Europe. The first eigenvalue accounts for 47% of the variance reduction of the data, the second for 27% etc. Each principal component (PC) is a temporal eigenvector that has a corresponding spatial eigenvector (EV). Figure 3a shows that PC1 dominates the decomposition and corresponds to a large annual signal. The third PC has very little coherence and its EV is quite different to the first EV. Also shown is the weighted PC and EV, which are obtained by taking the sum of the first 7 individual PCs (and EVs) weighted by the corresponding eigenvalue (these account for > 95% of the variance reduction). The weighted solutions are an attempt to show, in a single principal component and eigenvector, the relative complexity of the time and spatial components of the data set.

GLDAS Hydrology

One of the most widely used global continental hydrology models is GLDAS/Noah (Rodell et al. 2004). The model is based on the meteorological forcing from rainfall, snowfall and energy fluxes that appear as soil moisture, evapotranspiration, canopy water and snow cover. The only missing part is the surface water (runoff, rivers, etc.). The sum of soil moisture and snow cover is used as a loading mass to compute the gravity effect. One component of gravity is mass attraction of the soil moisture layer, and we separate the local effect (at the station, effectively a delta function load) from the rest of the attraction that is considered regional. The second component is crustal loading that is not subdivided because it represents the overall deformation of the ground in response to the water load.

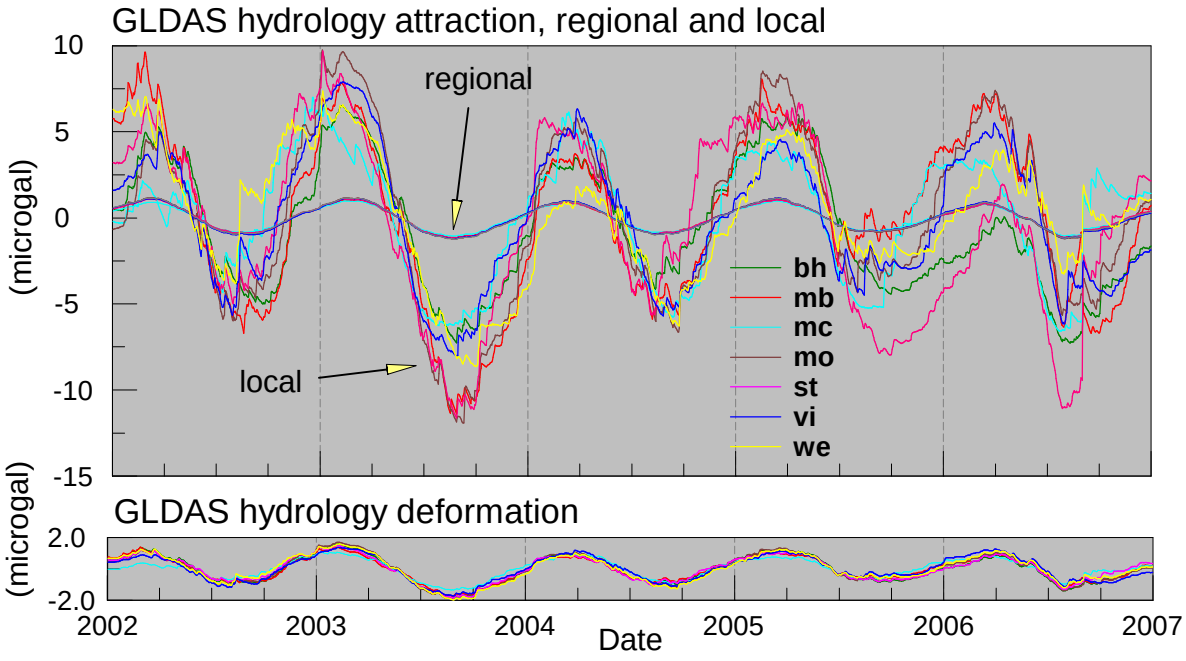

Figure 4. Components of the gravitational attraction and loading at GGP sites from the GLDAS hydrology model. The attraction is given for both the local effect (delta function at station) and for the remaining contribution (regional).

Figure 4 shows that the local attraction dominates the gravity effect at each station, and also the regional attraction and loading deformation are approximately the same; all components are in phase. This separation of the loading is a useful indicator of the extent to which hydrology needs to be accounted for if the SG is below the soil moisture level, in which case the sign of the local attraction is reversed. This assumes all the soil moisture is above the instrument, which is not always the case, especially for Moxa. The GLDAS data is also resampled to the GRACE GRGS and CSR epochs, and then the same minimum curvature grid is generated as for the GGP data.

EOF Comparisons

We now compare the 3 types of data using the EOF analysis of each data set. One feature of the decomposition is that the principal components are not affected by the relative phases of each station, so the combination of SGs being above and below ground level (Figure 2) does not reduce the amplitude of the time variation, as seen in Figure 5(a). It is also apparent that the GLDAS amplitude is significantly larger than either the GRACE or the GGP signals. In the case of GRACE, this would be compensated by the inclusion of the vertical effect mentioned earlier (factor 1.32). In the case of GGP the PC1 is reduced because only 3 of the 7 stations have a clear hydrology signal below the station, and the other 4 stations have a mixed signal that reduces the amplitude of PC1. The data for Moxa contributes little to an annual signal, either positive or negative.

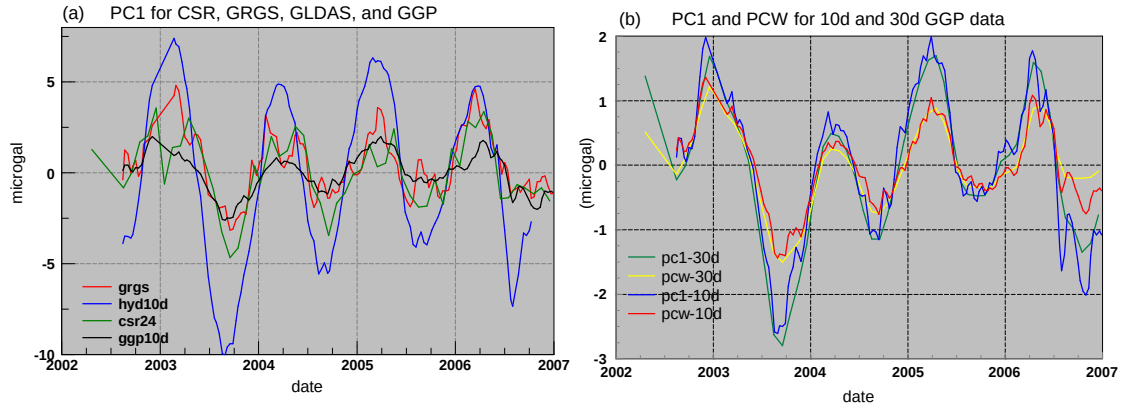

Figure 5. Comparison of the first PC for (a) representative data sets, and (b) the effect of weighting the eigensolutions for GGP data.

We show in Figure 5(b) the difference between PC1 and the weighted PC for both the GRGS and CSR solutions. The weighted PC has less amplitude because it contains components of the other eigenmodes that do not contain the annual component. The first EV and weighted EV for the 30 day GGP residuals are shown in Figure 6. It is clear that the 3 stations above ground are positive (green/red) and those below ground are negative (blue). The weighted EV is somewhat different due to the complexity of the response from other eigenmodes, as for the weighted PC.

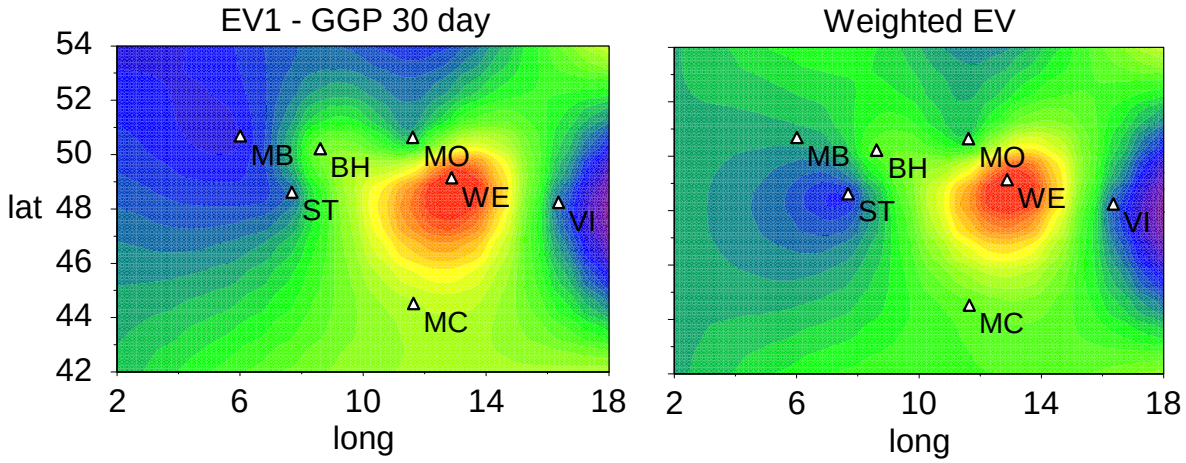

Figure 6. Comparison of the first EV and the weighted EV for the GGP data sampled at 30 days. Note that stations below ground have a negative polarity.

One of the reasons we would like to use GGP data is to verify not only GRACE data solutions, but also their comparison with GLDAS. At times when the GRACE solutions diverge from each other and from hydrology models, can GGP supply additional information? To answer this we show in Figure 7 a comparison between all solutions for two time periods, called anomaly 1 and anomaly 3. In the first case, the winter of 2003, GLDAS and GRGS solutions are both positive, whereas the CSR and GFZ solutions dip down. The corresponding GGP data has low amplitude but suggests no dip, perhaps supporting GRGS and hydrology. In late summer of 2005 the CSR solutions follow the hydrology, but the GRGS shows a positive peak. GGP solutions appear to follow better the GRGS, but are of the same sense as the CSR and hydrology, though obviously of weaker amplitude.

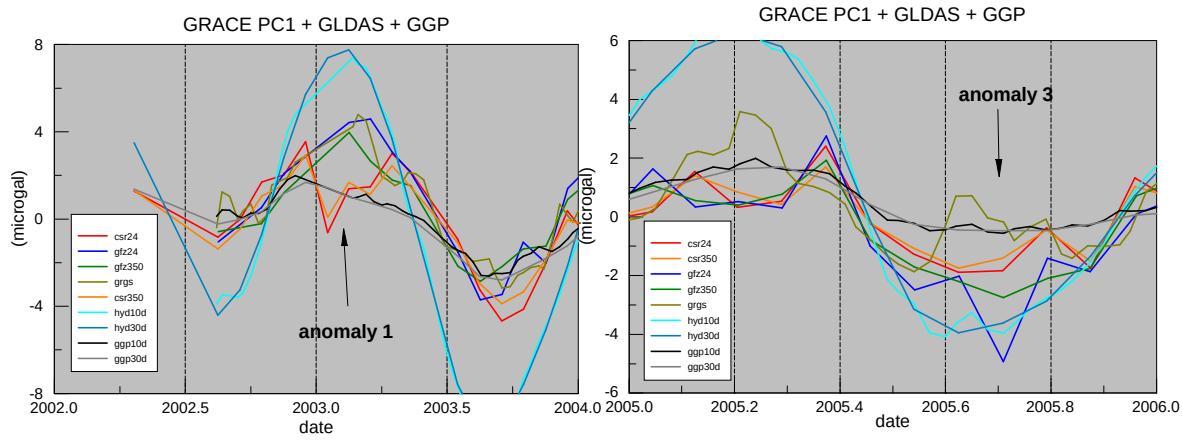

Figure 7. Details of two anomalous epochs (2003, left and 2005, right) where some of the GRACE solutions and GLDAS do not agree.

ASIA network

The only other group of GGP stations that could be used in the GRACE validation is in NE Asia (Figure 8). At the present time only 4 of the stations are supplying data to ICET: Esashi (ES), Matsushiro (MA), Kamioka (KA), and Wuhan (WU). Note that the area covered is much larger than for Europe, and the number of available stations is even smaller (especially at the present time). A further complicating factor is the relative size of GRACE averaging compared to available land areas.

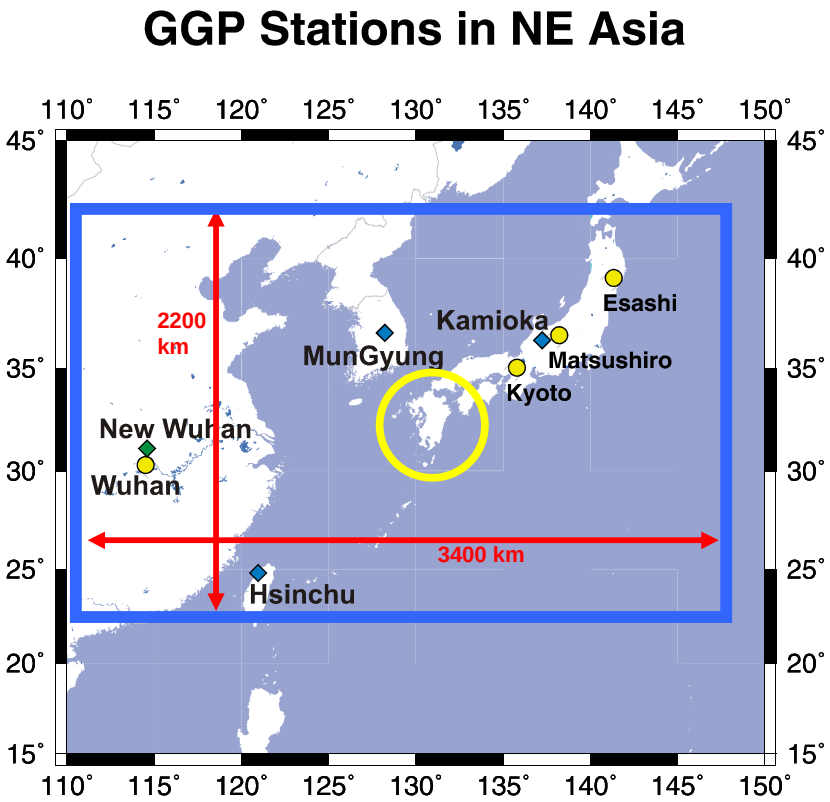

Figure 8. GGP stations in Asia for comparison with GRACE satellite data. The blue rectangle is much larger than for Europe, and the yellow GRACE target size necessarily includes ocean areas around the sites in Japan, S. Korea, and Taiwan.

Nevertheless, we processed the data for the 4 stations as for Europe, and show in Figure 9 a comparison between the GGP data and the GLDAS hydrology.

There are clear annual periods at WU and MA, correlated with hydrology. WU is nominally a surface station, but partly set into a hillside according to Xu et al. (2008); they indicate there is a 1 m layer of soil on the rooftop that might serve to invert the signal for soil moisture. Station MA has been studied extensively for hydrology by Imanishi et al. (2006) who found the typical inverted response for an underground station. The situation is similar at KA, where the station is deep underground at the neutrino test facility and irregular snowfall leads to a variable seasonal signal (Imanishi, personal communication). Station ES, also underground, shows some characteristics of the inverse relationship with hydrology, but the latter part of the record in 2006 clearly needs the removal of more disturbances to reveal the hydrological signal.

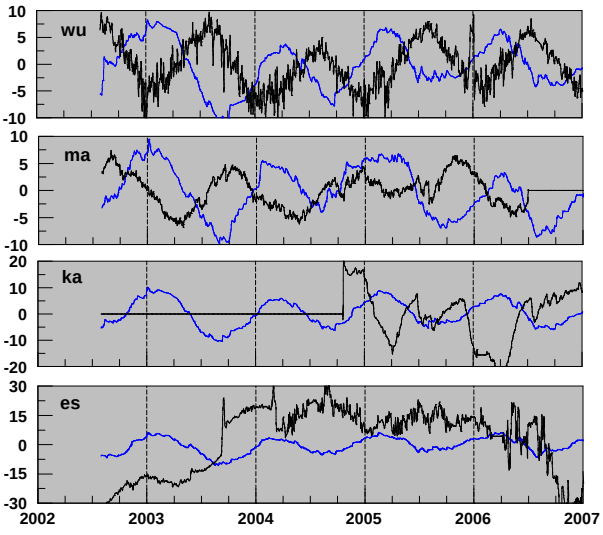

Figure 9. GGP residuals (black) and GLDAS hydrology (blue) for four stations in Japan and China. Data from Kamioka (KA) and Esashi (ES) probably require further processing for instrumental offsets.

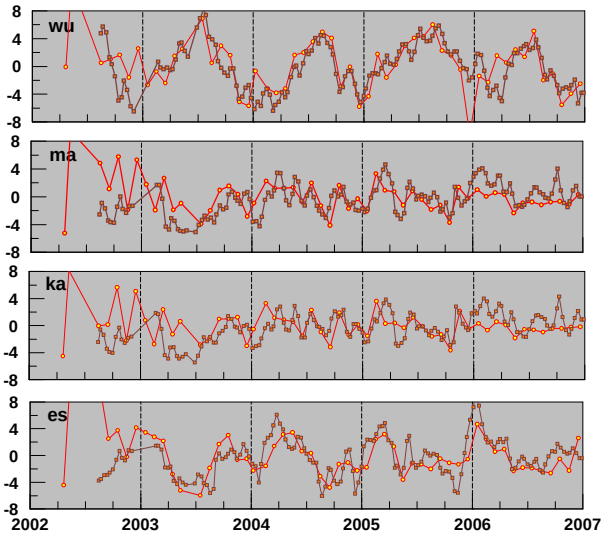

Figure 10. GRACE solutions CSR24 (red) and GRGS (brown) interpolated to GGP ground stations.

The GRACE data, interpolated directly to the four station locations, is shown in Figure 10. Only WU has a clear seasonal variability because it is well within the continental land mass, but curiously the expected phase is different from the GLDAS model – we are currently investigating the cause for this. The Japanese stations show little seasonal signal from either of the two GRACE solutions, no doubt because of the leakage of the signal due to the inclusion of the ocean (which yields no obvious hydrology signal, but there is a pressure loading).

Finally, we also show in Figure 11 the EOF decomposition of 3 of the GRACE solutions plus GLDAS hydrology. The variance reduction for the top 3 GRGS modes is only 30, 12, and 10% respectively, with similar results for the CSR and GFZ solutions. Clearly the PC1 is messy, but there is some correlation between GRGS and GLDAS. The spatial map (EV1) is also complex, caused by the mixture of land and ocean areas evident in Figure 8. We are not yet ready to say anything about the spatial coherence of the GGP data.

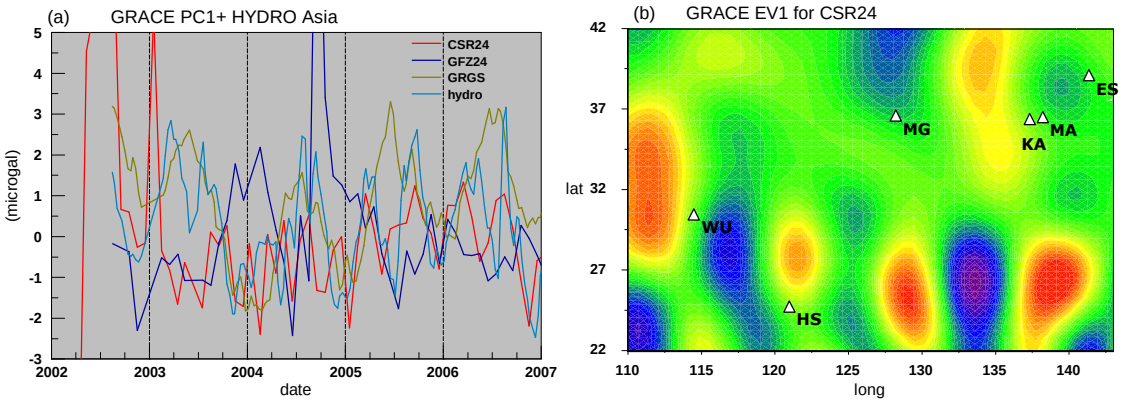

Figure 11. EOF solutions for NE Asia: (a) PC1 for 3 different GRACE solutions + GLDAS hydro, (b) EV1 for the CSR24 field.

Discussion and Conclusions

For the European data, the seasonal effect is well established up to the end of 2006, but the processing here lacks the vertical displacement that is handled by including a correction to the GRACE processing (e.g. Neumeyer et al. 2006; de Linage et al. 2008). A correction for the 3-D mass attraction of the atmosphere is also required, and we need to add data for 2007. All these deficiencies are being addressed in a more complete treatment of the European data in preparation.

As for the Asia data, there are still corrections to be added to the GGP processing, such as a 3-D atmosphere and the vertical loading effect, as well as more careful scrutiny of the station offsets, especially for Esashi. Nevertheless, we have now shown that the outlook for using the Asia stations as a network for GRACE comparisons is going to be difficult. This is, for the stations located in Japan, due to the leakage of the continental signal in the ocean and the very small land surface compared to the GRACE footprint

Acknowledgments

We thank the GGP station operators for supplying the data to ICET for this paper. Also, we appreciate discussions with C. Kroner (GFZ) and H. Wziontek (BKG) for supplying comments on offsets. Y. Imanishi provided useful comments on Matsushiro and Kamioka, but otherwise any errors in the Asian stations are a result of our own processing. This material is based upon work supported by the National Science Foundation under Grant No. 0409381, and CNRS (French Research Ministry).

References

Andersen, O.B., Seneviratne, S.I., Hinderer, J., and Viterbo, P. 2005. GRACE-derived terrestrial water storage depletion associated with the 2003 European heat wave, *Geophys. Res. Lett.*, **32** (18).

Andersen, OB. and Hinderer, J., 2005. Global inter-annual gravity changes from GRACE: Early results, *Geophys. Res. Lett.*, **32** (1).

Crossley, D. and J. Hinderer, 2007a., Report of GGP activities to Commission 3, completing 10 years for the worldwide network of superconducting gravimeters, *IAG Proceedings of the IUGG Meeting, Perugia 2007*, in press.

Crossley, D. and J. Hinderer, 2007b. The Contribution of GGP Superconducting Gravimeters to GGOS, *IAG Proceedings of the IUGG, Perugia 2007*, in press.

Crossley D., Hinderer J., Boy J.-P., de Linage C., 2006, Status of the GGP Satellite project, *Bull. d'Inf. Marees Terr*, **142**, 11423-11432

Hinderer, J., Andersen, O., Lemoine, F., Crossley, D., and Boy, J.-P., 2006. Seasonal changes in the European gravity field from GRACE: A comparison with superconducting gravimeters and hydrology model predictions, *J. Geodynamics*, **41**, 59-68.

Crossley, D., Hinderer, J., and Boy, J.-P., 2005. Time variation of the European gravity field from superconducting gravimeters, *Geophys. J. Int*., **161**, 257-264.

Crossley, D., 2004. Preface to the Global Geodynamics Project, *J. Geodyn*. **38** 225-236.

Crossley, D., Hinderer, J., & Boy, J.-P., 2004. Regional gravity variations in Europe from superconducting gravimeters, *J. Geodynamics*, **38**, 325-342.

De Linage, C., D. Crossley, J. Hinderer, J.-P. Boy, and J. Famiglietti, 2008. A comparison between GRACE observations, hydrology model predictions and ground gravity measurements by the superconducting gravimeters of the Global Geodynamics Project (GGP) in Europe, *AGU Fall Meeting*, poster G31B-0656.

Han, S.-C., Shum, C. K., Bevis, M., Ji, C. et Kuo, C.-Y. (2006). Crustal Dilatation Observed by GRACE after the 2004 Sumatra-Andaman Earthquake. *Science*, **313**:658–662.

Imanishi, Y., K. Kokubo, and H. Tatehata, 2006. Effect of underground water on gravity observation at Matsushiro, Japan, *J. Geodyn*. **41**, 221–226

Lambotte,S., L. Rivera, and J. Hinderer, 2006. Rupture length and duration of the 2004 Aceh-Sumatra earthquake from the phases of the Earth's gravest free oscillations, *Geophys. Res. Lett*., **33** (3), L03307, doi: 10.1029/2005GL02409

Neumeyer, J., F. Barthelmes, O. Dierks, F. Flechtner, M. Harnisch, G. Harnisch, J. Hinderer, Y. Imanishi, C. Kroner, B. Meurers, S. Petrovic, Ch. Reigber, R. Schmidt, P. Schwintzer, H.-P. Sun and H. Virtanen, 2006. Combination of temporal gravity variations resulting from superconducting gravimeter (SG) recordings, GRACE satellite observations and global hydrology models, *J Geod*. **79**: 573–585, DOI 10.1007/s00190-005-0014-8

Panet, I., Mikhailov, V., Diament, M., Pollitz, F., King, G., de Viron, O., Holschneider, M., Biancale, R. et Lemoine, J.-M. (2007). Coseismic and post-seismic signatures of the Sumatra 2004 December and 2005 March earthquakes in GRACE satellite gravity, *Geophys. J. Int*., **171**:177–190.

Swenson, S., P.J.-F. Yeh, J. Wahr, and J. Famiglietti, 2006. A comparison of terrestrial water storage variations from GRACE from in situ measurments from Illinois, *Geophys. Res. Lett*., **33**, L16401.

Xu, J., J. Zhou, S. Luo, and H. Sun, 2008. Study on characteristics of long-term gravity changes at Wuhan station, *Chinese Science Bulletin*, **53** (13), 2033-2040.

BLANK PAGE